Electric Field Induced Formation and Characterization of Nanoscroll from Water-Submerged Graphene Nanoribbon

A thesis submitted to the

Department of Electrical and Electronic Engineering (EEE)

of

Bangladesh University of Engineering and Technology (BUET)

In partial fulfillment of the requirement for the degree of

MASTER OF SCIENCE IN ELECTRICAL AND ELECTRONIC ENGINEERING

by

Mahnaz Islam

(Roll No.: 0417062209 P)

DEPARTMENT OF ELECTRICAL AND ELECTRONIC ENGINEERING (EEE)

BANGLADESH UNIVERSITY OF ENGINEERING AND TECHNOLOGY (BUET)

May 2019

The thesis titled **"Electric Field Induced Formation and Characterization of Nanoscroll from Water-Submerged Graphene Nanoribbon"** submitted by Mahnaz Islam, Roll No.: 0417062209 P, Session: April 2017, has been accepted as satisfactory in partial fulfillment of the requirement for the degree of MASTER OF SCIENCE IN ELECTRICAL AND ELECTRONIC ENGINEERING on May 27, 2019.

Board of Examiners

1. **Dr. Md. Kawsar Alam**
   Chairman
   (Supervisor)

   Professor
   Department of Electrical & Electronic Engineering (EEE),
   Bangladesh University of Engineering and Technology (BUET),
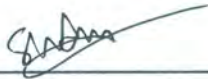   Dhaka-1205, Bangladesh

2. **Dr. Md. Shafiqul Islam**
   Member
   (Ex-officio)

   Professor and Head
   Department of Electrical & Electronic Engineering (EEE),
   Bangladesh University of Engineering and Technology (BUET),
   Dhaka-1205, Bangladesh

3. **Dr. Shaikh Asif Mahmood**
   Member

   Associate Professor
   Department of Electrical & Electronic Engineering (EEE),
   Bangladesh University of Engineering and Technology (BUET),
   Dhaka-1205, Bangladesh

4. **Dr. Mohammed Abdul Basith**
   Member
   (External)

   Professor
   Department of Physics,
   Bangladesh University of Engineering and Technology (BUET),
   Dhaka-1205, Bangladesh

Declaration

It is hereby declared that this thesis or any part of it has not been submitted elsewhere for the award of any degree or diploma.

Signature of the candidate

Mahnaz Islam

(Roll No.: 0417062209 P)

Dedication

To yours truly.

Acknowledgements

I must express my indebtedness and thankfulness to my thesis supervisor, Dr. Md. Kawsar Alam, Professor of the Department of Electrical and Electronic Engineering, Bangladesh University of Engineering and Technology, Dhaka for his unique mentoring style, insightful suggestions and for guiding me on the correct path whenever I felt lost (which was often and always). His dedication, enthusiasm, and love towards research inspired me in my work and his friendly attitude helped me in overcoming the problems I faced. I am grateful to him for giving me second (and third, and …) chances, and always believing in me. I am honored to have had the opportunity to work under his guidance and it will be my pleasure to continue to do so in the future, in any position.

I am also indebted to Md. Mushfiqur Rahman for his support and guidance.

I would like to thank the board members of my thesis committee, Prof. Dr. Md. Shafiqul Islam, Dr. Shaikh Asif Mahmood and Prof. Dr. Mohammed Abdul Basith for their invaluable feedback on my work.

Also, I wish to express my gratitude to the Department of Electrical and Electronic Engineering, Bangladesh University of Engineering and Technology for supporting this research work with the resources of Nanoelectronic Devices and Materials Research Laboratory to carry out the time-consuming simulations.

Lastly, I would like to thank my parents and my brother for their unconditional love and endless support. In a world of variables, my family has been the only constant.

Abstract

In this thesis work, a technique to induce the formation of a nanoscroll from a graphene nanoribbon structure submerged in water using a rotating electric field is proposed. In particular, we use molecular dynamics simulation to show that electric field induced rotation of water dipoles can, in turn, originate rotation of the immersed nanoribbon. The proposed setup is such that one end of the nanoribbon is kept fixed, while the other end orients itself with the rotating electric field and eventually, self-assembles into a more stable nanoscroll configuration. We compute the time evolution of the van der Waals interaction energy of the nanoribbon structure to explain its self-assembly into a nanoscroll. Our results show that the final structure is more stable than the initial configuration and retains its stability on removal of the electric field as well as the aqueous environment. In addition, we characterize the nanoscroll formed using our method by studying concentration profiles of atoms along its scrolling directions, which depict the stability and uniformity of its morphology. To study the versatility of our proposed method, we vary the length, width, and chirality of the initial nanoribbon. Further, we study the effect of changing the process conditions such as angular frequency and strength of the applied electric field on the trajectory of the nanoribbon and the resulting scrolls formed. In each case, we use energy and concentration profiles to illustrate the stability and morphology of the nanoscrolls. Our studies reveal that the proposed method can be used to induce the self-assembly of any nanoribbon structure independent of its dimensions and chirality. Moreover, the method is fairly independent of the process conditions and thus can be utilized under any preferred rotating electric fields. Lastly, we show that the proposed method can also be employed to induce the scrolling of multilayer nanoribbons as well as to form nanotemplate encapsulated core/shell composite structures.

Table of Contents

List of Tables

List of Figures

Chapter 1

Introduction

The realization of extraordinary carbon nanomaterials, such as carbon nanotubes (CNT) and graphene, has paved ways for far-reaching novel applications in electronics, sensors, field emission, conductive polymers, energy storage, and bio-inspired systems, to name a few [1]. Analogous to a multi-walled CNT is a graphene sheet spirally wrapped into a one-dimensional hollow tubular structure called graphene nanoscroll (GNS) [2] with revolutionary applications in hydrogen and energy storage [3], actuators [4], nanofluidic devices [5], lubrication [6], catalysis, etc. [7]. GNS exhibits many properties of CNT and graphene as well as unique structural [8], electronic [9], and optical properties [10]. Despite such potential and increasing research interest [3, 4, 7, 11-14] fabrication of GNS still remains a challenge [12]. Different fabrication techniques such as arc discharge [2], ball milling [15], chemical [16], mechanical/physical routes [17], and more recently, formation activated by nano-templates [18, 19] have been proposed. However, these methods suffer from complex processing, high energy consumption, abundant impurities, and/or hybrid nanostructures rendering them insufficient to fabricate scalable, cost-effective and stable GNSs [12]. In this thesis work, we have proposed a purely physical, room-temperature method of obtaining pure nanoscroll without the added hindrance of a nanoparticle. The principle of formation is based upon the induced orientation of a non-polar nanoparticle submerged in water. It has been shown that hydrated nanoparticles subjected to an external electric (E-) field orient themselves towards the applied field [20, 21]. Utilizing this principle on a water-submerged graphene nanoribbon (GNR) precursor, a large-scale, reliable, simple and energy-efficient method of fabricating

pure GNS may be realized facilitating exciting new avenues of fundamental and applied research on nanoscrolls.

1.1. Carbon Nanomaterials

Carbon is a unique element and its many allotropic forms have been widely studied. The three-dimensional allotropes of carbon, sp^2 hybridized graphite and sp^3 hybridized diamond, were well known when C_{60} or "buckyball" was discovered in 1985 by Kroto *et al.* [22]. It is a member of the fullerene family which are zero-dimensional (0-D) allotropes of carbon that consist of cage-like molecules with a spheroid shape. Later in 1991, the 1-D CNTs were discovered by Ijima *et al.* [23]. CNTs are perhaps the most extensively studied allotrope of carbon because of their exceptional mechanical strength [24], high current density (as high as $10^9 A/cm^2$ [25]) paired with ballistic transport [26] and ultrahigh thermal conductivity (~3000W/mK for multi-walled [27] and ~3500 W/mL for single-walled CNTs [28]). They consist of tiny cylinders of graphene terminated at each end by six pentagonal rings. Different

(a) Fullerene (b) Multi-walled carbon nanotube (c) Single-walled carbon nanotube

(d) Carbon nanocone (e) Single-walled carbon nanohorn (f) Graphene
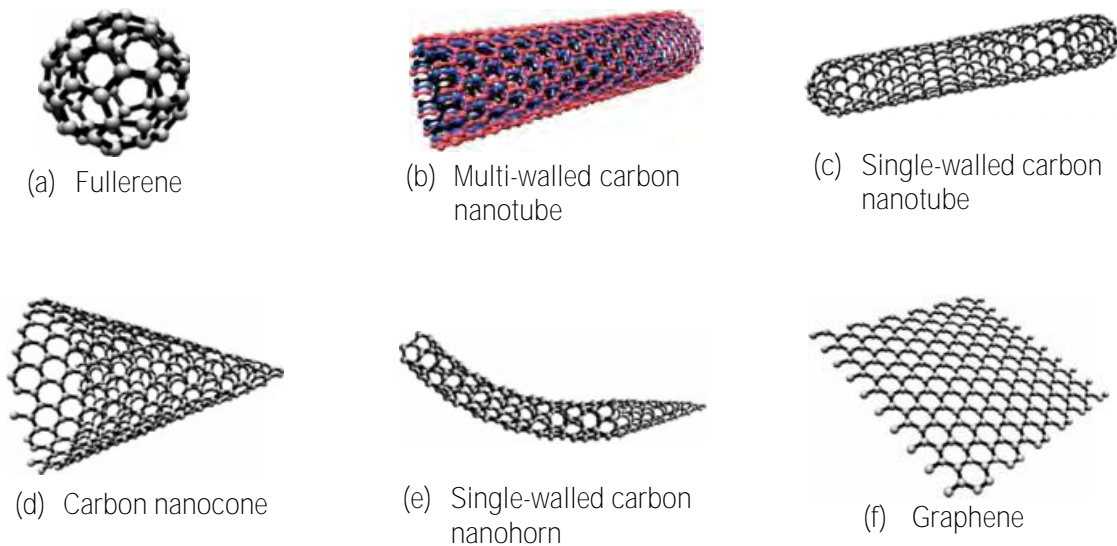
Figure 1.1. Schematic representation of the carbon nanostructures: (a) fullerene, (b) multi-walled carbon nanotube, (c) single-walled carbon nanotube, (d) carbon nanocone, (e) single-walled carbon nanohorn, and (f) graphene. (Reprinted with permission from Soto *et al.* [29])

synthesis routes may result in CNTs with single or multiple concentric graphene layers, known

as single-walled (SWCNT) and multi-walled carbon nanotubes (MWCNT) respectively.

Furthermore, the structure of SWCNTs are characterized by the chiral vector C_h, given by

$C_h=n*a_1 + m*a_2$, where a_1 and a_2 are the unit vectors in the hexagonal graphene lattice and n

and m are integers defined by C_h. Contrary to MWCNTs which are usually conducting,

SWCNTs are metallic if the value of n-m is a multiple of 3 and semiconducting otherwise. In
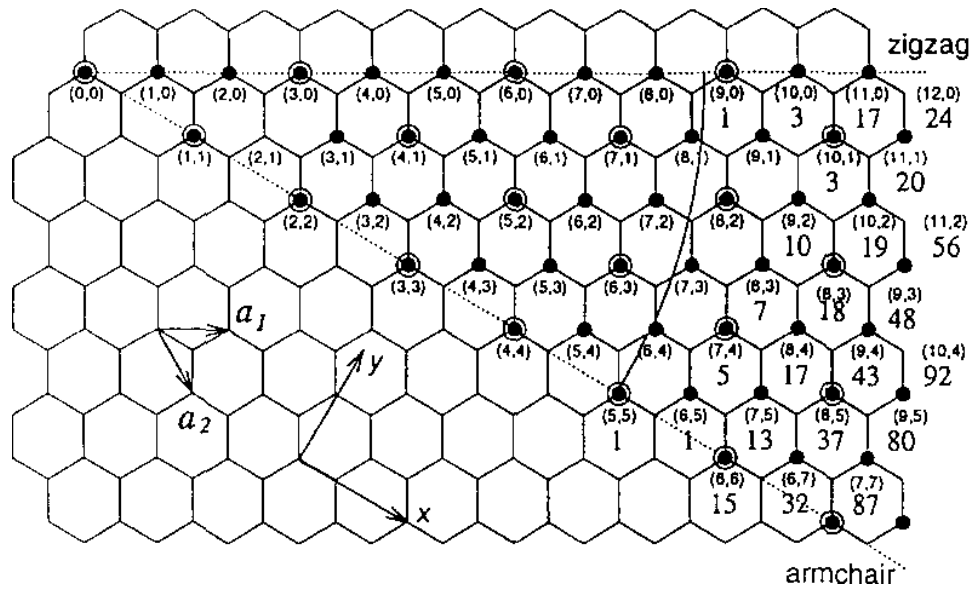
Figure 1.2. A 2-D graphene sheet is shown along with the vector which specifies the chiral nanotube. The pairs of integers (n,m) in the figure specify chiral vectors C_h for CNTs, including zigzag, armchair, and chiral tubes. The circled dots denote metallic tubes and the small dots are for semiconducting tubes. (Reprinted with permission from Dresselhaus *et al.* [30])

context, a chiral angle of 0° refers to a zigzag structured SWCNT and 30° refers to an armchair

one.

Finally, in 2004, the building block of graphitic carbon-based nanomaterials-graphene was

isolated via the renowned "Scotch" tape method by Novoselov *et al.* [31]. Graphene is a 2-D,

atomically thin crystal consisting of a single layer of carbon packed in a hexagonal lattice.

Other fabrication routes of graphene include ball milling of pristine graphite, exfoliation using

ultrasonication in a liquid environment, epitaxial growth on silicon carbide, chemical vapor deposition on metallic substrates, etc. [1]. An exceptional feature of the graphene band-structure is a zero band gap at the Fermi level. The suspended 2-D nanomaterial can exhibit high field-effect mobilities up to 200,000 cm^2/Vs [32] and high carrier concentrations up to 4 x 10^{14} cm^{-2} [33].

On the other hand, GNRs are quasi 1-D narrow strips of graphene with atomically smooth edges, obtained by nanocutting graphene and nanotubes via catalytic nanoparticles [34, 35], patterning by nanolithography [36] as well as unzipping of CNTs by plasma [37] or chemical etching [38]. Although 2-D graphene generally exhibits semimetallic behavior, GNRs can be either metallic or semiconducting based on the width as well as the topology of their edges (zigzag or armchair) [39].

1.2. Nanoscroll: A New Carbon Nanomaterial

More recently, a new type of carbon nanomaterial has drawn increased research attention among the carbon scientists, namely graphene nanoscroll (GNS) [2]. GNS is basically a rolled up graphene sheet resembling a spiral papyrus-like multilayer structure. Thus, morphologically GNSs are similar to MWCNTs except for their unique open-ended structure. As a result, the diameter of GNS can be tuned by changing its effective surface energy [40]. Their interlayer galleries can be easily intercalated with donors and acceptors, which expand to accommodate the volume of the intercalant [41]. They offer more efficient utilization of the surface area of graphene sheets due to the open topology [42]. At the same time, they inherit some of the excellent electronic and mechanical properties of MWCNTs and preserve the high carrier mobility exhibited by graphene [43].

4

(a)   (b)   (c)
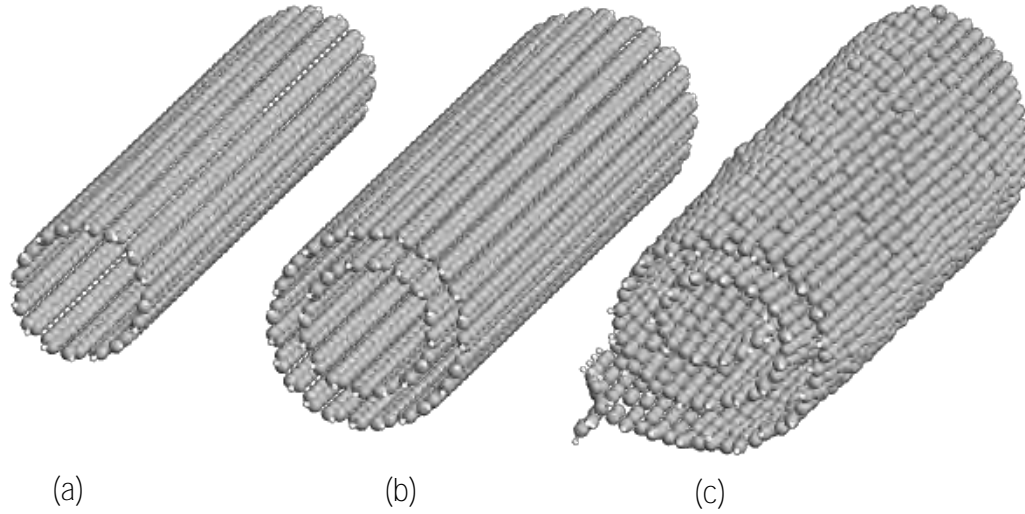
Figure 1.3. Atomistic configuration of (a) Single-walled CNT, (b) Multi-walled CNT, and (c) Graphene Nanoscroll.

Topologically, GNSs are considered to be Archimedean spirals and described by the polar equation:

$$r = r_0 + \frac{h}{2\pi}\phi \tag{1.1}$$

Where r represents points on the scroll for a given core radius r_o, interlayer spacing h, and a number of turns N (ϕ varies from 0 to $2\pi N$). Also, the scroll type can be armchair, zigzag or chiral depending on the axis around which the scroll was wrapped.
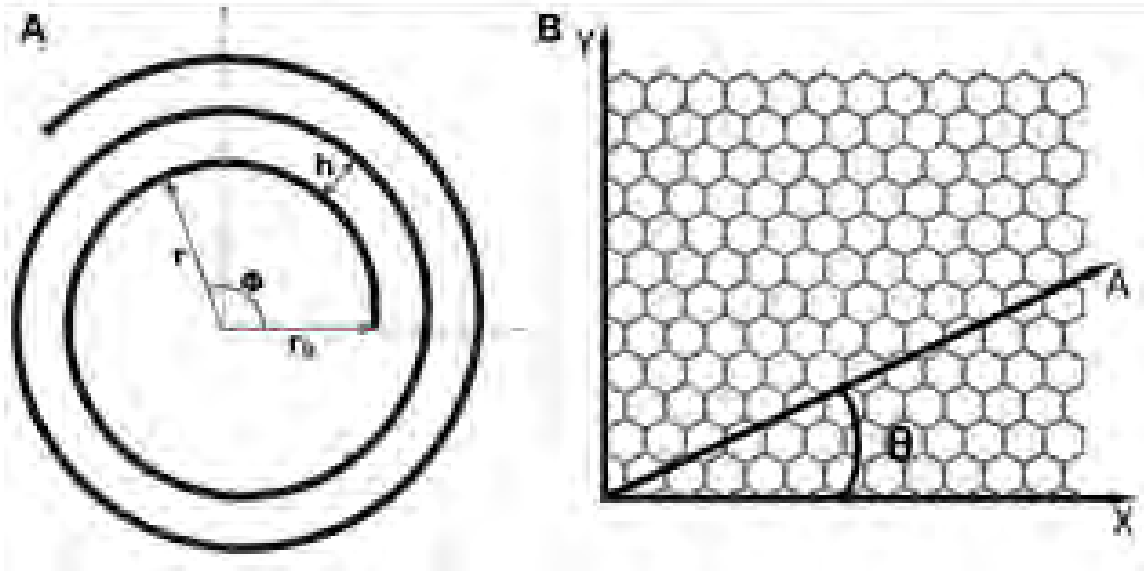
Figure 1.4. (a) Schematic representation of the cross-section of a GNS. The points r lie on the scroll for a given core radius r_0, interlayer spacing h, and number of turns N (φ varies from 0 to $2\pi N$) (b) Schematic showing the rolling up direction for a GNS from a graphene sheet. θ is the rolling angle and A is the GNS axis. (Reprinted with permission for Perim *et al.* [44] Copyright © 2014 Perim, Machado, and Galvao)

In the open-coil nanostructure, scrolling and unscrolling of the GNS is attained by exploiting the interlayer Van der Waal (vdW) forces and is stabilized when the vdW interaction energy overcomes the increasing elastic energy due to bending of graphene sheets. The bending energy, E_{bend} can be defined as:

$$E_{bend} = \frac{1}{2} A_{bend} \frac{D}{r^2} \tag{1.2}$$

A_{bend} is the bending area of graphene and D is the flexural rigidity. In addition, there is an energy penalty associated with the generation of an exposed edge. On the other hand, the interlayer interaction that is responsible for stabilizing multiwall structures corresponds to an interlayer separation of 0.34 nm, common to all sp^2 bonded structures. Thus, a scroll structure will be stable if the energy gain from formation of inter-wall interactions outweighs the strain

6

energy in bending of a graphene sheet and energy required to form two exposed edges along the axis of formation.

1.2.1. Applications

The open topology of GNSs has attracted considerable attention for its use in hydrogen storage [41, 42, 45]. Even though pure GNSs cannot store hydrogen due to its low inter-wall distance, intercalation via Alkali atoms enhances its volumetric intake of hydrogen atoms more than CNTs [41, 42, 45]. The tunable core size of GNSs has also found applications in controllable water and ion channels and nanofluidic devices [46-48]. Shi *et al.* have shown that GNS-based channels display much greater water permeability and sensitivity to an applied DC/AC E-field in comparison to CNT-based water channels [5]. Another important application of GNSs is in electroactuators, facilitated by its diameter change upon adding/removing charges [4, 49]. Shi *et al.* also reported a translational nanoactuator based on substrate-based GNSs where the rolling/unrolling action was brought about by changing the effective surface energy, and suggested to be achieved in practice by applying E-fields [50].

GNSs support much higher current density than MWCNTs and therefore have been explored for electronic devices [17, 19, 51]. GNSs carry current throughout a continuous scrolled graphene layer in contrast to MWCNTs which carry current only through the outermost layer (since the inner layers do not make direct contact) and thus can support a higher current density (up to 5×10^7 A/cm) [17], also making them suitable for interconnects over conventional materials [52]. They also offer better specific capacitances than MWCNTs and thus are used in supercapacitor applications [53-58]. Other applications of GNS in energy storage systems utilize them as electrodes in batteries [7, 54, 59, 60] and in catalysis [61]. The thermal conductivity of GNSs has been reported to be comparable to that of graphene, i.e.

3000- 5000 $Wm^{-1}K^{-1}$, suggesting promising applications as thermal interface materials (TIMs) in electronic packages [62]. The radial thermal expansion coefficient of GNS is two to three orders of magnitude larger than the linear thermal expansion coefficient of diamond, hinting their potential as sensitive temperature sensors. Last but not the least, GNSs have found applications in lubrication- macroscale superlubricity realized during interfaces sliding against each other was traced back to the formation of diamond-like-carbon wrapped nanoscrolls between them [6].

1.3. Literature Review

GNSs were first reported in 1960 as "graphite whiskers", a byproduct of arc discharge experiments conducted by Bacon *et al.* using graphite electrodes [2]. Besides GNSs, other carbon nanostructures such as nanotubes and fullerenes were also formed in these extremely high energy experiments [63-65]. In addition, high energy ball milling of graphite has been reported to yield scroll-like tubular structures [15]. The non-selectivity of these methods paired with the high cost and low yield render them insufficient for production of GNSs, as it is almost impossible to isolate GNS from the complex mixture of nanostructures. In fact, it was proposed that GNSs be classified as part of the MWCNT family for its layered structure [59, 66]. Thus, the synthesis of MWCNT in 1993 by Ijima *et al.* attracted renewed attention toward high yield fabrication of GNSs [23]. One of the first methods reported for a high yield fabrication of ~80% of GNSs was in 2003 [67]. Viculis *et al.* intercalated high-quality graphite with potassium metal, followed by exfoliation in ethanol to disperse the intercalated graphite into carbon sheets, which upon probe sonication curl into nanoscrolls. The conditions of scrolling were critically dependent upon the duration and power of the sonication step. Even so, the 80% efficiency of the method facilitated its use in related nanoscroll studies [68]. In a

separate study of graphite intercalation compounds, GNSs were reported via a similar method as Viculis *et al*. with the exception of an absence of sonication [16]. In that work, scroll structures were observed after the intercalated polymer was dissolved in an appropriate solution such as N-methyl-2-pyrrolidone for a long period of time. The isolated graphene sheets would curl into nanoscrolls as a result of the vdW interaction if significant overlapping occurred [8].

The donor-type intercalation compounds (alkali metals) used in the aforementioned chemical routes to nanoscrolls deemed it necessary to use an inert atmosphere due to their extreme reactivity. The harsh reaction conditions thus render the processes unsuitable for mass production. Savoskin *et al.* overcame this limitation by using acceptor type intercalation compound, namely graphite nitrate in a low-temperature synthesis [69]. However, the difficulty in controlling the rolling initiation and rolling direction of the graphene associated with this approach means that the scroll structure has an undetermined number of layers. Moreover, there is an added possibility of introducing defects in the scroll structure during the chemical process.

The discovery of 2-D graphene in 2004 prompted its direct use for the fabrication of GNSs. Xie *et al*. proposed a new method of fabrication of GNSs *in situ* that allowed more control over its morphology [17]. The scotch tape method is used to mechanically exfoliate graphite which is then deposited over SiO_2 /Si substrate. Upon immersion in a solution of water and isopropyl alcohol, the induced strain results in rolling of the graphene sheets into nanoscroll. The process was found to be sensitive to the contamination and shape of the precursor graphene. Another *in situ* method was suggested by Yu and Liu where electrostatic deposition of graphene under certain gaseous environment resulted in the folding of graphene into scroll

like structures driven by the external stress from adsorption of gas atoms [70, 71]. While these methods offer higher control over the final structures, they are difficult to scale and more sensitive to the quality of the graphene layers. Very recently, Schmidt *et al.* proposed an *in situ* formation of electrically contacted GNS from suspended GNRs with slight tensile stress, however, its formation probability is limited by the length to width aspect ratio [14]. Zheng *et al.* demonstrated the formation of high-quality GNSs assisted by microwave irradiation in liquid nitrogen [72]. Graphite flakes were rapidly heated by microwave sparks while the coated graphene sheet was cooled by liquid nitrogen. The resulting strain discrepancy causes the scrolling of the graphene sheet, which are isolated via sonication and centrifugation. Derivatives such as graphene oxide have also been utilized for fabrication of nanoscrolls via different techniques such as microexplosion [55], Langmuir-Blodgett (LB) [73], cold quenching in liquid nitrogen [74], lyophilization [75], etc. Chemical vapor deposition of graphene has also been employed for fabrication of GNSs [76-78].

While the aforementioned methods produce GNSs with a hollow core, other theoretical [12, 18, 79-86] and experimental works [19, 54, 58, 61, 87-89] have reported hybrid structures in which a nanotemplate encapsulated scroll/wrapped graphene structure is produced. Nanotemplates in the form of water nanodroplets [79], single or multi-walled CNTs [18, 80, 82, 84, 85], diamond-like carbon nanoparticle [6], fullerene [86], Si Nanowire [81, 83], metal nanoparticles [12] have been used to induce the self-assembly of graphene to form hybrid structures. The common reason cited to explain the self-assembly is the vdW interactions between the nanotemplate and the planar material that induces the formation of a more stable hybrid structure than the individual ones. As described by Braga *et al.*, although a scroll structure can be a more stable structure than the corresponding 2-D planar one, there is an

energy barrier associated in the transformation [8]. It is exactly this energy cost that is provided by the vdW interaction between a nanotemplate and a graphene sheet which in turn induces the scrolling motion.

In this regard, the earliest work was reported in 2009 by Patra *et al.* who demonstrated that a water nanodroplet can act as a catalyst that initiates deformation in the 2-D layered material causing bending, folding, and under a certain combination of graphene and nanodroplet size, rolling of the planar nanostructure into water droplet encapsulated nanoscroll [79]. CNTs have been another popular template in this regard [18, 80, 82, 84, 85]. Xia *et al.* demonstrated the formation of a stable core/shell structure when the CNT radius is larger than about 10 Å [18]. To overcome the difficulty of controlling a free-standing graphene sheet, Zhang *et al.* proposed a similar approach for substrate supported graphene sheet which was still very sensitive to the CNT diameter and position [80]. Later, Perim *et al.* modified the setup using a substrate with chamber/pits to reduce this sensitivity [84]. As for nanowires, Chu *et al.* [83] and Xia *et al.* [81] demonstrated in separate studies the self-scrolling of graphene sheets onto Si nanowires under certain threshold conditions, such as a Si nanowire radius larger than about 5 Å. The thresholds associated with these reported procedures correspond to the energy barrier in forming a scroll structure from a planar one. Thus, the formation is critical upon the dimension and position of the nanotemplate used, relinquishing less control over the process. Moreover, there have been no assuring reports on how to remove the nanotemplate once a scrolled structure is obtained. Thus, the cost and difficulty in removing the templates are their main hindrance to large scale production and applications of such processes [53].

In summary, a simple, all-dry, purely physical, room-temperature, energy-inexpensive method towards the fabrication of a pure GNS without the added complexity/hindrance of a

nanotemplate is missing from the literature. In this work, we have proposed such a method that utilizes the E-field induced orientation of a suspended GNR structure submerged in water to facilitate its assembly into a GNS with hollow core and homogeneous morphology. While previous methods have used sonication, microwave irradiation, induced strain or nanotemplates, we have used an E-field to achieve self-assembly of the GNR. Using molecular dynamics (MD) simulations, the proposed method is shown to be versatile for any length, width, and chirality of the initial GNR, thus offering more control over the final structure, and relatively independent of the setup parameters, that is the applied E-field strength and frequency. In addition, it is shown that the same setup may be utilized to produce core/shell composite structures without the limitation of a critical dimension of the nanotemplate. Finally, in addition to single layer GNR, the proposed method is also shown to produce stable scroll structures from multilayer GNRs.

1.4. Objectives of the Thesis

The objectives of this thesis are:

i. To explore the effect of E-fields on a freestanding GNR submerged in water.

ii. To design a GNR-based system submerged in water which may be assembled into a nanoscroll using external E-fields.

iii. To explore the effect of structural variations (e.g. length, width and chirality) of the GNR precursor on the formation stability of the nanoscroll.

iv. To study the effect of applied field properties such as magnitude, direction, and frequency on the formation mechanism, characteristics, and energy variations of the nanoscroll.

v.   To utilize the proposed scheme to form nanotemplate encapsulated core/shell composite structures as well as scrolling of multilayer GNRs.

1.5. Thesis Overview

This thesis is divided into four (4) chapters-

i.   **Chapter 1** provides an introductory note followed by the background and motivation, a comprehensive literature review, and the objectives.

ii.   **Chapter 2** covers a brief description of the simulation methodology employed in this work as well as a theoretical overview and simulation framework.

iii.   In **Chapter 3**, we propose a novel suspended GNR system that utilizes the ultrafast orientation of hydrated nanoparticles guided by rotating E-fields to attain a more stable scroll structure. We provide energy and concentration profiles to characterize the formation of the 1-D scroll structure from the 2-D planar one. We also analyze different scrolls formed as a result of varying length, width and chirality of the initial GNR as well as varying E-field parameters. Additionally, we utilize the proposed method to obtain the scrolling of multilayer GNRs as well as to form hybrid core/shell structures.

iv.   **Chapter 4** contains the concluding remarks followed by possible future works.

Chapter 2
Theoretical Overview

The emergence of nanotechnology has attracted an immense multidisciplinary research interest towards the design, production, and application of structures, devices, and systems at the nanoscale. The versatility of carbon materials in the form of a metal which can also be found as 2-D graphene, 3-D semiconductor as diamond, a quantum dot fullerene molecule, and a 1-D quantum wire nanotube has in turn given rise to the research field of carbon nanotechnology. In addition to advances in experimental techniques for fabrication and measurement tools in this area, there has been significant research of carbon nanostructures using computational methods. In this chapter, we will start by explaining the choice of the simulation technique used to study our GNR-based system, followed by a brief theoretical overview of the chosen method. Lastly, we will provide details of the particulars used in our simulation technique with relevance to the GNR-based system.

2.1. Choice of Simulation Technique

Molecular modeling is the atomistic process of describing complex systems in terms of a realistic atomic model, with an intent to compute and analyze macroscopic properties based on extensive knowledge at an atomic scale. Macroscopic physical properties can be classified into *(a)* static equilibrium properties, such as the average potential energy of a system and *(b)* dynamic or non-equilibrium properties, such as the viscosity of a liquid. Quintessentially, the time-dependent Schrödinger equation describes the properties of molecular systems with high accuracy, using positions of the nuclei and the number of electrons in order to yield useful information such as electron densities, energies, etc. Such an *ab initio* method needs a wave

function description for the electrons since it treats the electronic and ionic degrees of freedom separately and hence is computationally expensive and time-consuming. Thus, systems more complex than the equilibrium state of a few atoms cannot be handled at this *ab initio* level.

While microscopic simulations generate information at the microscopic level, including atomic positions and velocities, the conversion of this microscopic information to macroscopic properties such as pressure, energy, heat capacities, etc., requires statistical mechanics [90]. Macroscopic properties are thus ensemble averages over a representative statistical ensemble of molecular systems. The two broad families of techniques available for the generation of such a representative statistical ensemble are: *(a)* Monte Carlo simulations and *(b)* Classical Molecular Dynamics (MD) simulations [91]. In a Monte Carlo simulation, at each step, a random move of a molecule is attempted and random numbers are used to decide whether or not to accept the move; the decision depends on whether the energy change would be favorable. Monte Carlo simulations do not provide information about time evolution. Rather, they provide an ensemble of representative configurations from which probabilities and relevant thermodynamic quantities, such as the free energy, may be calculated. On the other hand, MD simulations can resolve the nanosecond-scale time evolution of a molecule by solving the classical equations of motions to calculate the forces acting on each molecule which are used to advance the positions and velocities through a small time step for the specified amount of time. Thus, for a study such as ours that requires the temporal evolution of the coordinates and the state of a macromolecule structure, MD simulation is the most universal choice.

2.2. Molecular Dynamics Simulation

The MD method was first introduced by Alder and Wainwright in the late 1950s [92, 93] to study the interactions of hard spheres. The next major attempt was by Rahman in 1964, when the first simulation using a realistic potential for liquid argon was carried out [94]. The first MD simulation of a realistic system was done by Rahman and Stillinger in their simulation of liquid water in 1974 [95]. In the current literature, one routinely finds MD simulations of organic and inorganic material systems addressing various issues including the thermodynamics of biological processes, polymer chemistry, and crystal structure. Moreover, MD simulation techniques are widely used to help interpret experimental results from X-ray crystallography and nuclear magnetic resonance spectroscopy [96]. MD simulations have also been a popular technique to study atomistic simulations of carbon nanostructures' behavior at the nanoscale [5, 8, 12, 18, 40, 45, 50, 79-86, 97].

The classical MD simulations solve Newton's equations of motion for a system of N interacting atoms:

$$m_i \frac{\partial^2 \boldsymbol{r}_i}{\partial t^2} = \boldsymbol{F}_i, i = 1...N \tag{2.1}$$

The forces are the negative derivatives of a potential function $V(\boldsymbol{r}_1, \boldsymbol{r}_2 \ldots \boldsymbol{r}_N)$:

$$\boldsymbol{F}_i = -\frac{\partial V}{\partial \boldsymbol{r}_i} \tag{2.2}$$

The equations are solved simultaneously in small time steps. The system is simulated for the desired amount of time, taking care that the temperature and pressure remain at the required values with the help of heat baths, and the coordinates are written to an output file at regular

intervals. The coordinates as a function of time represent a trajectory of the system. The forces $\boldsymbol{F}_i$ acting on the atoms are usually derived from a potential energy V.

2.2.1. Potential Function

The potential functions can be subdivided into three constituents: *(a)* Non-bonded interactions, *(b)* Bonded interactions, and *(c)* Restraints.

2.2.1.1 Non-bonded Interactions

A part of the potential energy function, V represents the non-bonded interactions between atoms split into 1-body, 2-body, 3-body… terms. Usually, the three body and higher order interactions are disregarded, thus considering only the pair potentials. The pair potentials, $V(r_{ij})$ may be modeled as Lennard-Jones (or 12-6 interaction), the Buckingham (or exp-6 potential), etc. In this work, we have modeled the uncharged carbon atoms using the 12-6 interaction which is given by:

$$V_{LJ}(r_{ij}) = 4\varepsilon_{ij}\left[\left(\frac{\sigma_{ij}}{r_{ij}}\right)^{12} - \left(\frac{\sigma_{ij}}{r_{ij}}\right)^{6}\right] \tag{2.3}$$

using two parameters- σ, the diameter and ε, the well depth.

The force derived from this potential is:

$$\boldsymbol{F}_i(\boldsymbol{r}_{ij}) = 4\varepsilon_{ij}\left[12\frac{\sigma_{ij}^{12}}{r_{ij}^{13}} - 6\frac{\sigma_{ij}^{6}}{r_{ij}^{7}}\right]\frac{\boldsymbol{r}_{ij}}{r_{ij}} \tag{2.4}$$

If electrostatically charged particles are present, then the appropriate Coulombic expression is added to the potential function. The Coulomb interaction between two charged particles is given by:

$$V_c(r_{ij}) = \frac{1}{4\pi\varepsilon_o} \frac{q_i q_j}{\varepsilon_r r_{ij}} \tag{2.5}$$

where q_i and q_j are the charges and ε_o is the permittivity of free space. The force derived from this potential is:

$$F_i(r_{ij}) = \frac{1}{4\pi\varepsilon_o} \frac{q_i q_j}{\varepsilon_r r_{ij}^2} \frac{\mathbf{r}_{ij}}{r_{ij}} \tag{2.6}$$

The correct handling of long-range forces in a simulation is an essential aspect of MD simulation and is discussed further in Section 2.2.3.2.

2.2.1.2   Bonding Interactions

Bonded interactions consist of pair interactions (bond stretching), 3-body (bond angle) and 4-body (dihedral angle) interactions.

i.   *Bond stretching*

The bond stretching interaction may be represented by many different potential functions such as the harmonic potential, fourth power potential, Morse potential, Cubic bond stretching potential, FENE bond stretching potential, etc. The bonds involve the separation $r_{ij} = |r_i - r_j|$ between adjacent pairs of atoms in a molecular framework. In this work, we have represented the carbon-carbon bond stretching using the Morse potential which is given by:

$$V_{bond} = V_{morse}(r_{ij}) = D_{ij}[1 - \exp(-\beta_{ij}(r_{ij} - b_{ij}))]^2 \tag{2.7}$$

and the corresponding force is:

$$F_{morse}(\mathbf{r}_{ij}) = 2D_{ij}\beta_{ij}r_{ij}\exp(-\beta_{ij}(r_{ij} - b_{ij})) * [1 - \exp(-\beta_{ij}(r_{ij} - b_{ij}))]\frac{\mathbf{r}_{ij}}{r_{ij}} \tag{2.8}$$

18

where D_{ij} is the depth of the well, β_{ij} defines the steepness of the well and b_{ij} is the equilibrium distance.

ii.   Bond angle

The bond angle vibration between a triplet of atoms *i-j-k* may be represented by a harmonic potential, a cosine based angle potential, a restricted bending potential, the Urey-Bradley potential, etc. The bond angles θ_{ijk} are between successive bond vectors such as $r_i - r_j$ and $r_j - r_k$, and therefore involve three atom coordinates. In this work, we have used a cosine based angle potential to represent the bond angle vibration between the carbon-carbon atoms, which is given by:

$$V_{angle} = V_a(\theta_{ijk}) = \frac{1}{2} k_{ijk}^{\theta} \left(\cos(\theta_{ijk}) - \cos(\theta_{ijk}^o) \right)^2 \tag{2.9}$$

where $\cos(\theta_{ijk}) = \dfrac{r_{ij}.r_{kj}}{r_{ij}r_{kj}}$. The corresponding force can be derived by partial differentiation with respect to the atomic positions.

iii.   Dihedral angle

For calculating proper dihedral interaction, one can use either the GROMOS periodic function or a function based on Fourier expansion in powers of cos φ (the so-called Ryckaert-Bellemans (RB) potential). The RB dihedral function can also be used to include Fourier dihedrals, has been employed in this work. The torsion angles ϕ_{ijkl} are defined in terms of three connected bonds, hence four atomic coordinates. Thus the potential function may be written as:

$$V_{dihedral} = V_{RB} = \frac{1}{2} \sum_{torsionangles} \sum_{m} k_{ijkl}^{\phi,m} (1 + \cos(m\phi_{ijkl} - \phi_m)) \tag{2.10}$$

where m is the order of periodic functions.

2.2.1.3 Restraints

Special potentials are used for imposing restraints on the motion of the system, either to avoid extreme deviations or to include knowledge from experimental data. Restraints may be on position, angle, dihedral, distance and/or orientation. In our work, we have applied a position restraint on the non-water part of our simulation structure during solvent equilibration only in order to avoid drastic rearrangements i.e. to restrain motion in the GNR structure when it is subjected to large solvent forces since the solvent is not yet equilibrated. The potential function has the form:

$$V_{pr}(r_i) = \frac{1}{2} k_{pr} |r_i - R_i|^2 \tag{2.11}$$

A simulation package force field specifies the treatment of the various potential parameters discussed in this section, the values of the various strength parameters k and other constants involved as well as the form of the total potential function.

2.2.2. Force Field

A force field has two distinct components *(a)* the set of equations used to generate the potential energies and their negative derivatives, the forces *(b)* description of the parameters used in this set of equations. Some of the most well-known force fields are- AMBER, CHARMM, GROMOS, OPLS, REBO, ECEPP, AIREBO, etc. In this work, we have used the OPLS (Optimized Potentials for Liquid Simulations)-AA (all atom) force field to generate the potential function, V [98, 99]. Under OPLS-AA, the total potential function V is given by:

$$V(r_1, r_2...r_N) = V_{bonded} + V_{non-bonded} \qquad (2.12)$$

where,

$$V_{bonded} = V_{bond} + V_{angle} + V_{dihedral} \qquad (2.13)$$

and

$$V_{non-bonded} = V_{LJ} + V_C \qquad (2.14)$$

where the components have been described in the previous section.

2.2.3. The MD Algorithm

A global flow scheme for MD is given in **Figure 2.1**. Each MD run requires a set of initial coordinates and initial velocities of all particles involved as input. To calculate a trajectory, the initial positions of the atoms, an initial distribution of velocities and the acceleration, determined by the gradient of the potential energy function, is needed. Using Newton's laws of motion:

$$x = \frac{1}{2}at^2 + v_o t + x_o \qquad (2.15)$$

Where the position, x at time t is described as a function of the acceleration, a, the initial position, x_o, and the initial velocity, v_o The equations of motion are deterministic, i.e. the positions and the velocities at time zero determine the positions and velocities at all other times, t. The initial positions can be obtained from the structure defined, the initial distribution of velocities are usually determined from a random distribution (e.g. Maxwell-Boltzmann distribution or Gaussian distribution) with the magnitudes conforming to the required temperature, T and corrected so there is no overall momentum.

The potential energy is a function of the atomic positions (3N) of all the atoms in the system. Due to the complicated nature of this function, there is no analytical solution to the equations of motion; they must be solved numerically using an integrator as described in the following section.
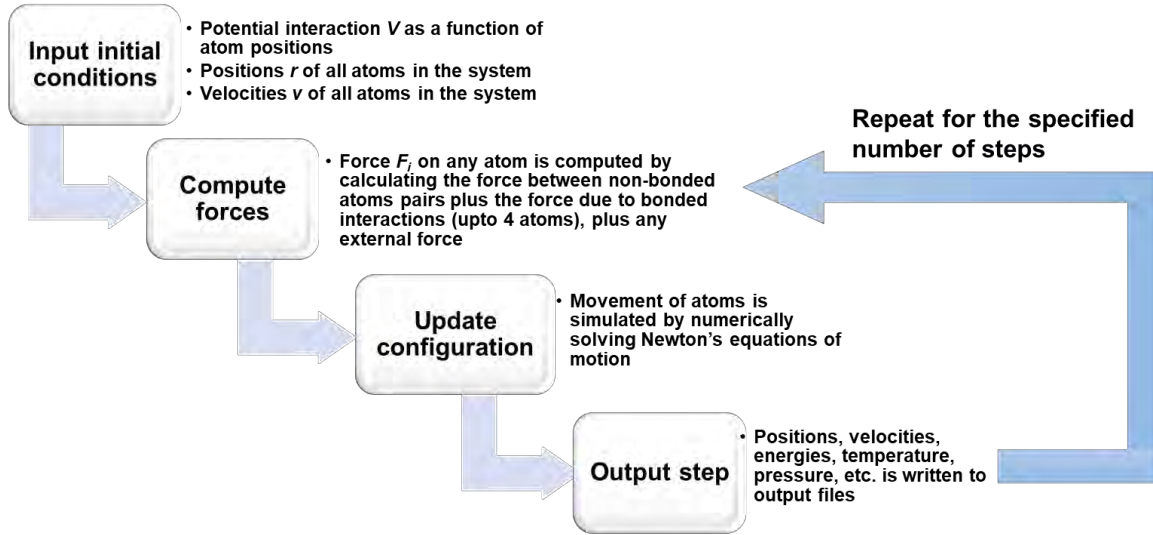
Figure 2.1. Flowchart describing a general MD algorithm.

2.2.3.1 Integrator

All the integration algorithms, such as the Verlet algorithm, the Leap-frog algorithm, the Velocity Verlet, the Beeman's algorithm assume the positions, velocities, and accelerations can be approximated by a Taylor series expansion. In this work, we have used the leap-frog algorithm to solve Newton's laws of motion [100]. The leap-frog algorithm uses positions r at time t and velocities v at time $t - \frac{1}{2}\Delta t$. It updates positions and velocities using the forces $\mathbf{F}(t)$ determined by the positions at time t using:

$$\mathbf{v}(t + \frac{1}{2}\Delta t) = \mathbf{v}(t - \frac{1}{2}\Delta t) + \frac{\Delta t}{m}\mathbf{F}(t) \tag{2.16}$$

22

$$r(t + \Delta t) = r(t) + \Delta t v(t + \frac{1}{2}\Delta t) \qquad\qquad (2.17)$$

The equations of motion are modified for temperature coupling and pressure coupling, which are described in Section 2.2.3.5. The leap-frog scheme is a modification of the Verlet scheme. The error in the positions calculated through the unmodified Verlet scheme is on the order of $(\Delta t)/2$, while the leap-frog scheme results in a global error of the order $(\Delta t)/3$ thus providing more accurate predictions of the positions and velocities of the atoms for the same time step. The time step Δt used for integration of the MD equations is of critical importance to its accuracy. If the value of Δt is too large, then the resulting system will be unstable, equipped with a drift in the total energy of the system. On the other hand, if the value is too small, the total time of simulation and the size of the output files would increase drastically. The time step is determined by the largest oscillation frequency in the system. This is in general associated with the hydrogen atoms in the system. The leap-frog integrator used in GROMACS allows a maximum time step of 2 fs without compromising the accuracy of the simulations [101]. The time step used in the simulations presented in this thesis was 2 fs for solvent equilibration and 1 fs for production runs.

2.2.3.2 Long Range Electrostatics

As mentioned previously, the Coulombic expression is used to describe the electrostatic potential on charged particles. The total electrostatic energy of N particles and their periodic image is the summation of individual Coulombic terms. Computation of the direct sum to calculate the electrostatics is considered tedious and computationally expensive. Thus, different numerical techniques such as the Ewald summation [102], Particle-mesh Ewald [103], Particle-Particle Particle-Mesh [104], etc. may be used instead. In this work, we have used the Particle-mesh Ewald (PME) method to compute the electrostatics of relevant charged

particles. The PME algorithm scales as $N \log(N)$ and is substantially faster than ordinary Ewald summation on medium to large systems.

2.2.3.3 Periodic Boundary Condition

To minimize edge effects in a finite system, it is required to apply suitable boundary conditions to simulate actual conditions. Some of the most common boundary conditions are Free, Rigid, Periodic, etc. While the free and rigid boundary conditions are good approximations for molecules placed in a vacuum, periodic boundary conditions are useful for approximating the behavior of macro-scale systems of gases, liquids, and solids. Thus, in our work, we applied periodic boundary conditions. The atoms of the system to be simulated are put into a box, which is surrounded by translated copies of itself. Thus there are no boundaries of the system; the effect of unwanted boundaries in an isolated cluster is replaced by the effect of periodic conditions. If the potential range is not too long, the minimum image convention in which each atom interacts with the nearest atom or image in the periodic array can be employed. In the course of the simulation, if an atom leaves the basic simulation box, an incoming image of the atom is used instead.

2.2.3.4 Energy minimization

If a starting configuration is very far from equilibrium, the forces may be excessively large and the MD simulation may fail. Thus, it is necessary to minimize the potential energy of the macromolecular structure to overcome this deficiency and create a more realistic structure [105]. Performing an energy minimization also removes all kinetic energy from the system. Energy minimization may be done using steepest descent, conjugate gradients, or l-bfgs (limited-memory Broyden-Fletcher-Goldfarb-Shanno quasi-Newtonian minimizer). In our study, we used the steepest descent method to energy minimize the initial configuration. At first, the forces F and potential energy are calculated, and new position is calculated using:

$$r_{n+1} = r_n + \frac{F_n}{\max(|F_n|)} h_n \qquad (2.18)$$

Where h_n is the maximum displacement. The forces and energy are again computed for the new positions, which are accepted if the new potential is less than the current value. The algorithm stops when either a user-specified number of force evaluations has been performed, or when the maximum of the absolute values of the force (gradient) components is smaller than a specified value.

2.2.3.5 Ensembles

Although direct use of MD results gives rise to the NVE (constant number, constant volume, constant energy) ensemble, to simulate realistic experimental conditions, the MD simulations must be performed either at constant volume and temperature (NVT or canonical ensemble) or at constant pressure and temperature (NPT or isobaric-isothermal ensemble). The total energy is not conserved in these ensembles. The conservation of a quantity, such as the volume or the pressure, requires a constant exchange of energy in between the macromolecular system and the surrounding heat bath. A temperature bath or thermostat is used to simulate an NVT ensemble. Some popular thermostats are Berendsen [106], stochastic randomization through the Andersen thermostat [107], the extended ensemble Nosé-Hoover scheme [108, 109], or a velocity-rescaling scheme [110]. Similarly, some of the famous barostats use the Berendsen algorithm [106] that scales coordinates and box vectors every step, the extended-ensemble Parrinello-Rahman approach [111, 112], and for the velocity Verlet variants, the Martyna-Tuckerman-Tobias-Klein (MTTK) implementation of pressure control [113].

2.3. Models and Simulation Parameters

The GNR structure proposed in this work for the formation of a nanoscroll was created using the "Builder" module of the Virtual Nanolab - Atomistix toolkit (QuantumATK version 2016.4) [114]. To study the self-assembly of the GNR structure immersed in water under an applied rotating E-field into a nanoscroll, we adopted the MD simulation approach. The MD approach is a popular technique for studying GNR-based systems [5, 8, 12, 18, 40, 45, 50, 79-86, 97]. We used the GPU-accelerated-GROMACS 5.1.5 package [101] as the computational platform, wherein the carbon atoms were modeled as uncharged Lennard-Jones (LJ) particles [46] and the optimized potentials for liquid simulations- all atom (OPLS-AA) force field [98] was implemented. Bonded interaction between carbon-carbon atoms was accounted for by a Morse bond potential for bond stretching, a harmonic cosine potential for bending and a twofold cosine potential for torsion as shown by the first three terms in Eq. (2.19). The bonded potential terms are commonly limited up to 4-body interactions, where any higher body interactions can be ignored [91]. The non-bonded potential contributions are excluded from these interactions and suitable functional forms are added separately for simplicity [98]. In our analysis, the non-bonded vdW interactions are described by 12-6 LJ potential [115], shown by the last term in Eq. 2.19. The equation itself is simply the addition of all bonds, angles, dihedrals and non-bonded potential terms under the OPLS-AA field, as proposed by Jorgensen *et al*., [98]. The values of the interaction potential parameters for carbon atoms are given in **Table 2-1**.

$$U(r_{ij}, \theta_{ijk}, \varphi_{ijkl}) = K_{Cr}[\exp(-\gamma(r_{ij} - r_C)) - 1]^2 + \frac{1}{2}K_{C\theta}(\cos\theta_{ijk} - \cos\theta_C)^2$$

$$+ \frac{1}{2}K_{C\varphi}(1 + \cos(2\varphi_{ijkl} - \varphi_C)) + 4\varepsilon_{CC}\left[\left(\frac{\sigma_{CC}}{r_{ij}}\right)^{12} - \left(\frac{\sigma_{CC}}{r_{ij}}\right)^6\right] \tag{2.19}$$

Here, the bonding parameters K_{Cr}, r_C and γ are the parameters for the Morse bond potential; $K_{C\theta}$ and θ_C are the parameters for the bending angle potential; $K_{C\varphi}$ and φ_C are the torsion parameters. The non-bonded parameters ε_{CC} and σ_{CC} are the LJ interaction for carbon-carbon atoms.

Table 2-1 Parameters for the atomic model of the GNR structure [20] [21][117-122]

Bonded Interaction Parameters		
K_{Cr}	478.9 kJ/mol	Spring constant, equilibrium bond length and steepness of well for Morse bond potential
r_c	0.1418 nm	
γ	21.867 nm^{-1}	
$K_{C\theta}$	562.2 kJ/mol	Spring constant and equilibrium bond angle for bending angle potential
θ_C	120º	
$K_{C\varphi}$	25.12 kJ/mol	Spring constant and equilibrium bond angle for dihedral torsion
φ_C	180º	
Non-bonded Interaction Parameters		
ε_{CC}	0.3601 kJ/mol	Well depth (ε) and collision diameter (σ) for C-C and C-O bond
σ_{CC}	0.34 nm	
ε_{CO}	0.4787 kJ/mol	
σ_{CO}	0.3275 nm	

For the water molecules, the TIP3P water model has been used [116]. The values of the interaction potential parameters for water are given in **Table 2-2**. As for GNR-water cross-interactions, a carbon-oxygen LJ potential was employed [46]. The values of ε_{CO} and σ_{CO} have been chosen to be 0.4787 kJ mol^{-1} and 0.3275 nm, respectively. It is noteworthy that the

interaction potential employed in the present work is commonly used in predicting the dynamics of carbon-based systems with a variety of other molecules such as water, ethanol, DNA, lipids, amino acids, etc. [21, 117-122]. It is also in good agreement with the experimental properties of water [98, 116]. Moreover, the potential is very consistent for a wide range of temperature variation [123-125].

$$U(\mathrm{r}_{ij},\theta_{ijk}) = \frac{1}{2}K_{Wr}(\mathrm{r}_{ij}-\mathrm{r}_W)^2 + \frac{1}{2}K_{W\theta}(\cos\theta_{ijk}-\cos\theta_W)^2 \qquad (2.20)$$

Here r_W and θ_W are the reference O-H bond length and H-O-H angle, and the K_{Wr} and $K_{W\theta}$ are the corresponding force constants.

Table 2-2 Parameters for the TIP3P Water Model[20] [21][117-122]

Bonded Interaction Parameters		
K_{Wr}	502416 kJ mol^{-1}	Spring constant, and equilibrium bond length for O-H bond
r_W	0.09572 nm	
$K_{W\theta}$	628.02 kJ mol^{-1}	Spring constant and equilibrium bond angle for H-O-H bond
θ_W	104.52°	
Non-bonded Interaction Parameters		
ε_{OO}	0.6367 kJ mol^{-1}	Well depth (ε) and collision diameter (σ) for O-O bond
σ_{OO}	0.3151 nm	
q_o	-0.834e	Charges on O and H atoms
q_H	0.417e	

The flowchart in **Figure 2.2** shows the details of the MD simulation steps employed in this work. For all the MD simulations conducted in this work, dangling bonds at the edges were appended by covalently bonded hydrogen atoms and the structure was energy minimized (EM) using steepest descent method with a tolerance in force of 1 kJ/mol/nm. The GNR structure was then equilibrated in water in an NVT ensemble using Berendsen thermostat [106] for 1 ns, with the number N of atoms, volume V, and temperature T constant. Further,

it was equilibrated in an NPT ensemble using Velocity rescaling barostat [110] for 1 ns with N, pressure P, and T constant. Periodic boundary conditions were applied in the X, Y and Z axes. Once the solvent was fully relaxed in terms of potential and kinetic energies and exhibited the desired temperature and pressure, the GNR structure was unrestrained and a rotating E-field was applied in the YZ plane. The rotating E-field was accomplished by applying two sinusoidal E-fields in the Y and Z directions with a 90° phase difference between them. All simulations presented in this work were performed at a temperature of 300 K and under a pressure of 1 bar. The temperature and pressure were maintained at the desired values using the Nose-Hoover thermostat [108, 109] at 0.1 ps coupling time and the Berendsen barostat [106] at 1.0 ps coupling time, respectively, during the final production run. The particle-mesh Ewald method [103] was used to model the long-range electrostatic interaction between water molecules and a cut-off radius of 1.2 nm was used for LJ interactions. The Leap-frog integration scheme [100] with a time step of 1 fs was used to solve the equations of motions, with data saved every 1 ps for a total simulation time of 10 ns, unless mentioned otherwise. The prolonged edges of the GNR structure were kept fixed in all directions. To convert between the different file types generated in this work, the OpenBabel-2.4.1 package was used [126, 127]. Lastly, the molecular graphics program VMD 1.9.2 was used for rendering molecular trajectories [128].

INPUT FILES	DESCRIPTION	OUTPUT FILES
gnr.xyz	VNL-ATK produces .xyz structure file which is converted to .pdb using Open Babel package	*gnr.pdb*
gnr.pdb	Input structure file type (.pdb) is converted to GROMACS structure file type (.gro) (*gmx editconf*)	*gnr.gro*
gnr.gro	Topology of the GNR structure is created using forcefield-OPLS-AA (*gmx x2top*)*	*gnr.top*
gnr.gro, spc216.gro, gnr.top	GNR structure is solvated in water- this adds solvent molecules to structure and topology files (*gmx solvate*)	*gnr_solv.gro, gnr.top*
gnr_solv.gro	Index file is created which contains the index numbers of the different groups of atoms (*gmx index*)	*gnr.ndx*
gnr_solv.gro, gnr.top minim.mdp	Energy minimization of solvated GNR structure to emulate equilibrium conditions using the Steepest descent algorithm (*gmx grompp + gmx mdrun*)	*em.xtc, em.trr, em.edr, em.gro*
gnr_solv.gro, gnr.ndx	GNR structure needs to be restrained in position during solvent equilibration (*gmx genrestr*)	*pos_gnr.itp*
em.gro, gnr.top, gnr.ndx, nvt.mdp	Solvent is equilibrated under an NVT ensemble using the Berendsen thermostat at a time-step of 2 fs for 1 ns simulation time (*gmx grompp + gmx mdrun*)	*nvt.xtc, nvt.trr, nvt.edr, nvt.gro*
nvt.gro, gnr.top, gnr.ndx, npt.mdp	Solvent is further equilibrated under an NPT ensemble using the V-rescale at a time-step of 2 fs for 1 ns simulation time (*gmx grompp + gmx mdrun*)	*npt.xtc, npt.trr, npt.edr, npt.gro*
npt.gro, gnr.top, gnr.ndx, md.mdp	Position, velocity and energy values of the solvated GNR structure under a rotating E-field is calculated at a time-step of 1 fs for 10 ns simulation time** (*gmx grompp + gmx mdrun*)	*md.xtc, md.trr, md.edr, md.gro*
	Post-Processing: trajectory (*gmx trjconv*), energy (*gmx energy*), density (*gmx density*), dipole moment (*gmx dipoles*)	

Figure 2.2. Flowchart of the simulation steps that have been carried out in the MD approach adopted in our work. The description of the input and output files at each step is given in **Table 2-3**.
* Topology file formed using *gmx x2top* needs further modification for C-H bonds. This was accomplished using MATLAB.
** The prolonged edges of the GNR structure are kept fixed during the final production run.

Table 2-3 Description of the different file types used in our simulation as shown in **Figure 2.2**.

File Type	Description
gnr.xyz, gnr.pdb, gnr.gro	Different types of structure files containing the GNR structure used in this study
gnr.top	Topology file containing the type of atoms, bonds, pairs, angles, and dihedrals
spc216.gro	Built-in structure file containing the TIP3P water model
gnr_solv.gro	Structure file containing the GNR structure solvated in water
gnr.ndx	Index file containing atoms separated into groups using their index numbers
pos_gnr.itp	Position restraints file for GNR structure
minim.mdp, nvt.mdp, npt.mdp, md.mdp	Files containing the settings for each production run. The *gmx grompp* command produces a .tpr file that contains all information necessary to execute a production run
em.xtc, em.trr, em.edr, em.gro	The output files for each MD run (EM, NVT, NPT, and MD) containing the coordinates (.xtc), velocities (.trr), energy (.edr) at the specified time-step. The .gro file contains the final structure formed after the specified simulation time of production run.

Chapter 3

Results and Discussion

3.1. Principle of Formation

When a static E-field is applied to a dipolar liquid such as water, the polarization of the water molecules causes the formation of dipoles which orient themselves along the applied E-field direction to attain a more energetically stable state. Daub *et al.* showed that a nanoparticle immersed in such a dipolar liquid in the presence of an applied static field will also orient itself along the field direction [20]. However, it is not a consequence of the polarization of the nanoparticle itself. The water dipoles tend to align their surfaces parallel to the applied field direction as well as the surface of the nanoparticle in order to minimize the system energy. This alignment process was rigorously studied by Daub *et al.* [20] for a nanoparticle and for a CNT by Guo *et al.* [120]. Using MD simulation, Guo *et al.* [120], showed that while water molecules orient toward the applied E-field direction due to the formation of dipoles, they also try to orient parallel to the CNT surface in order to maximize hydrogen bonds. In an effort to satisfy these two conditions, the CNT is forced to orient its surface toward the E-field [120]. However, no such study has been conducted for a GNR submerged in water. Thus, at first we used MD simulations to study the effect of a rotating E-field on a freestanding GNR immersed in water. In particular, a 100.3 Å × 51.9 Å GNR aligned with the XZ plane was placed in an 8 nm × 12 nm × 12 nm box containing 37,091 water molecules and an anti-clockwise rotating E-field of 1.0 V/nm magnitude and 10 Gr.p.m. angular speed was applied in the YZ plane for a simulation time of 30 ns. The rotating E-field can be realized using quadruple electrodes [129]. Our results show that the GNR continuously orients itself towards the rotating E-field

performing a spinning motion, which agrees well with the previous reports on E-field induced

hydrated nanoparticles [20, 120]. This validates the choice of our simulation environment.

The sequential snapshots showing the resulting angular displacement of the GNR are given in

Figure 3.1 ($t_1 \rightarrow t_2 \rightarrow \ldots \rightarrow t_{12}$). The full simulation video of 30ns may be found as "**Supporting**

Movie 1" in [130]. Water molecules are not shown in the video for clarity. It is interesting to

(a) t_1= 0 ns (blue)$\rightarrow$$t_2$= 1.5ns(r ed)$\rightarrow$
    t_3=3.9ns (yellow)

(b) t_4= 3.9ns (blue)$\rightarrow$$t_5$=4.65ns (red)
    $\rightarrow$$t_6$=5.4ns (yellow)

(c) t_7= 6.15ns (blue)$\rightarrow$$t_8$=6.9ns (red) $\rightarrow$
    t_9=7.65ns (yellow)

(d) t_{10}= 8.4ns (blue)$\rightarrow$ t_{11}=9.15ns (red)
    $\rightarrow$ t_{12}=9.9ns (yellow)
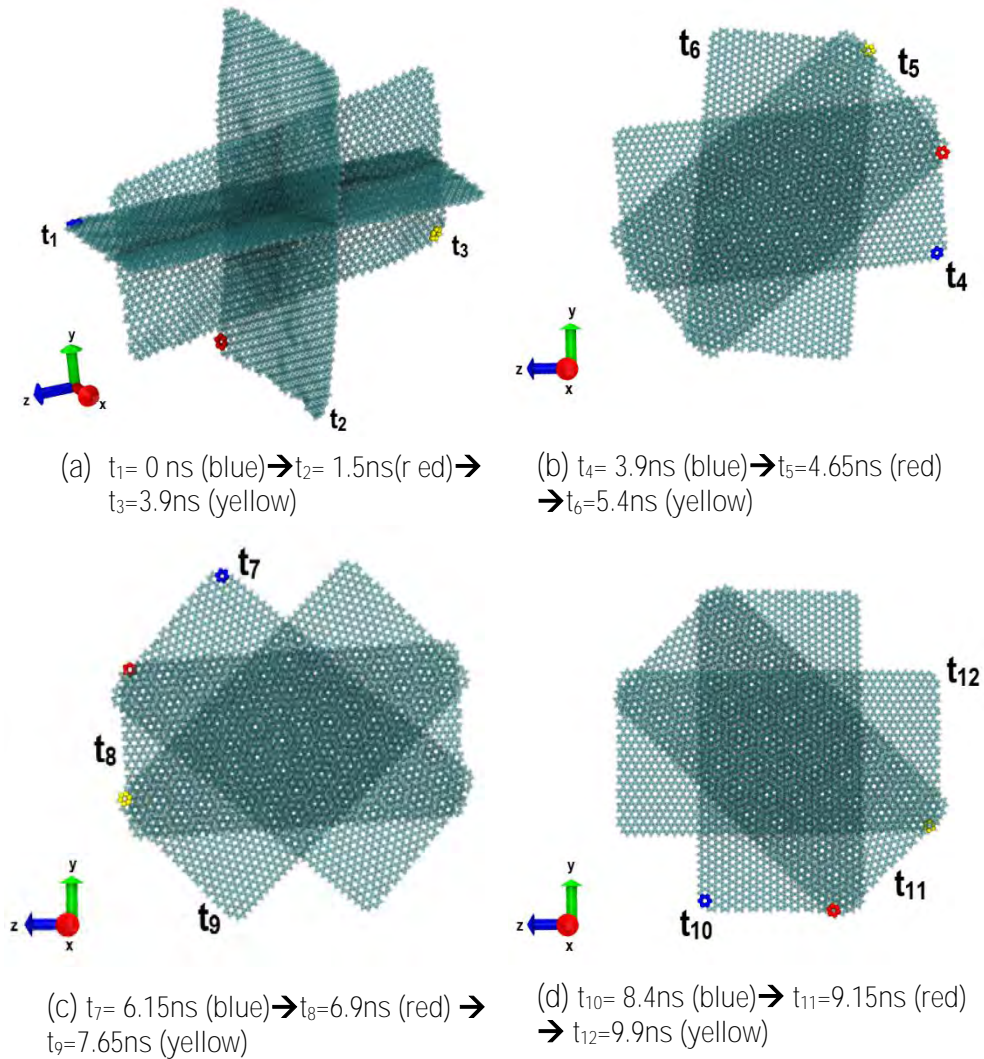
Figure 3.1. (a) GNR (at time t_1) is aligned with XZ plane when an anti-clockwise rotating E-field of strength 1 V/nm and 10 Gr.p.m angular frequency is applied in the YZ plane. GNR (at time t_2) has been rotating to align to the YZ plane. GNR (at time t_3) is almost aligned with YZ plane. (b), (c) and (d) show the sequential snapshots of the GNR 0.75 ns apart (1/8th of the time period) depicting its angular displacement. Water molecules are not shown for clarity.

note that the GNR first aligns with the YZ plane, as shown in **Figure 3.1**(a), where GNR marked blue is the initial state ($t_1=0$ ns) which upon application of an E-field rotates in two planes (GNR marked red shown at time t_2) until it aligns to the YZ plane (GNR marked yellow shown at time t_3). After that, the GNR follows the applied E-field and rotates in an anti-clockwise direction in the YZ plane, as shown in **Figure 3.1**(b), (c), and (d).

3.2. Proposed Setup to Form Nanoscrolls

To utilize the rotating E-field in achieving self-assembly of a GNR, the setup shown in **Figure 3.2**(a) is proposed. Two fixed substrates can be used to support the suspended GNR with prolonged edges on either side, while the whole setup is immersed in a dipolar liquid which is not shown in the schematic for clarity. This means that the prolonged edges are restricted in their motion due to surface adhesion with the substrate while the suspended portion is free to move. In conducting the MD simulations used in our study, the prolonged edges of the GNR have been kept fixed and the whole setup surrounded by water. An atomistic representation of the proposed setup is shown in **Figure 3.2**(b) including the water molecules. In all the studies conducted under this work, the GNR structure was placed aligned to the XZ plane with its prolonged edges fixed in motion while a rotating E-field was applied in the YZ plane unless specified otherwise. The length of the GNR is measured along the Z direction and the width along the X direction. The rotating E-field was achieved by applying two sinusoidal E-fields in the Y and Z directions with a 90° phase difference between them. All trajectories presented in this work have been calculated for a simulation time equal to five time periods of the corresponding E-field (30 ns for 10 Gr.p.m., 15 ns for 20 Gr.p.m.) unless it is less than 10 ns, in which case the simulation time is 10 ns (all other angular frequencies)
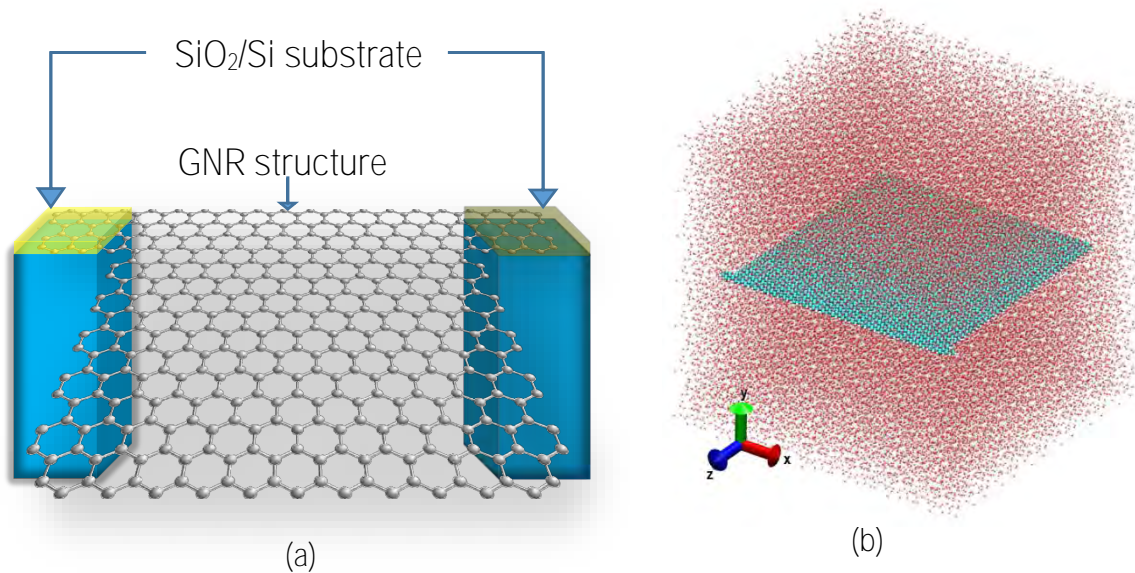
Figure 3.2. Proposed setup to induce the self-assembly of a GNR with prolonged edges using an applied E-field. (a) Device schematics: two substrates are used to suspend a GNR sheet with prolonged edges in a dipolar liquid such as water. (b) Corresponding atom based configuration of the system. To simulate the effect of placing the prolonged edges of the GNR on a substrate, the prolonged edges are kept fixed throughout our simulation.

GNRs have been fabricated through patterning by nanolithography [36], unzipping CNTs by plasma [37] or chemical etching [38], chemical exfoliation of graphene [131], nanocutting graphene and nanotubes via catalytic nanoparticles [34, 35], epitaxial growth of graphene on templated SiC [132], as well as by direct synthesis by self-assembly of polycyclic aromatic hydrocarbons [133]. The electronic and magnetic property of GNR is significantly determined by its width, crystallographic symmetry and edge termination leading to the development of fabrication tools capable of precisely controlling width and edge geometry of GNRs at the atomic scale [133, 134]. Cai *et al.* reported the bottom-up chemical synthesis of atomically precise GNRs with widths less than 10 nm [133]. Benett *et al.* reported a reliable full layer transfer of bottom-up synthesized GNRs [135]. Moreover, various cutting techniques have been developed to create GNRs with specific shapes [34, 136, 137].

Numerous works have reported on the electronic transport through T, L, Y, Z, and cross-shaped GNRs and the resulting nano-devices [138-143]. These methods can be employed to create GNRs with prolonged edges proposed in **Figure 3.2**. Alternatively, GNRs of suitable dimensions and edges can be fused together to create the junctions [144]. After the required GNR structure is prepared, it can be transferred to a suitable substrate and the whole set up suspended in water [135]. Obviously, the substrates have to be separated by at least the width of the GNR on its prolonged side and must have a height greater than the length of the GNR to allow its free suspension. The rotating E-field can be realized using quadruple electrodes [129]. Once a stable GNS is formed, the prolonged portion can be used as electrical contacts for device applications [14]. It is noteworthy to mention that a similar experimental setup of suspended graphene sheet immersed in polar/nonpolar liquid has been reported by Newaz *et al*. [145]. A similar setup for a CNT-based nanomotor in water that operates based on the same principle has also been recently reported [21].

3.3. Formation of Scroll Using the Proposed Setup

A 100.3 Å × 94.5 Å zigzag GNR structure, parallel to the XZ plane was placed in a 12 nm × 12 nm × 12 nm cubic box containing 55169 water molecules as shown in **Figure 3.2**(b), and an anti-clockwise rotating E-field of 90 Gr.p.m. angular frequency and 1 V/nm strength was applied in the YZ plane for a simulation time of 10 ns, with the prolonged edges of the GNR structure kept fixed. **Figure 3.3** shows the evolution in the vdW interaction energy profile of the GNR as a function of simulation time. The inset shows the same energy profile magnified for the first 4200 ps time of this simulation. **Figure 3.4** shows the snapshots of the resulting assembly of the GNR into a scroll structure at different time frames. The simulation video of 10 ns may be found titled "**Supporting Movie 2**" in [130]. It is observed that, in effect, GNR

tries to align itself with the direction of the rotating E-field. The effect of the fixed prolonged edges is that the GNR is fixed along the X axis in one of its width edges and only one of its width dimension is free to rotate. Thus, in following the rotating E-field, the GNR with fixed prolonged edges (**Figure 3.2**) rotates about its fixed edge and produces a folded structure in contrast to a freestanding GNR (**Figure 3.1**) which performs a spinning motion. It is seen that at t=660 ps (C2, **Figure 3.4**(b)), the GNR completes one rotation in the YZ plane about its fixed edge along the X axis with no significant change in its vdW (**Figure 3.3**). However further rotation causes the formation of a single folded, double layered graphene structure (C3, **Figure 3.4**(c)) accompanied by a sharp fall in the vdW interaction energy profile (**Figure 3.3**). Further rotation of this configuration is also followed by added folds (C4, **Figure 3.4**(d) and C5, **Figure 3.4**(e)) and corresponding falls in the vdW interaction energy (**Figure 3.3**). The process is thus driven by a combination of both the applied E-field and the vdW interaction causing self-assembly of the GNR. At t=3720 ps, the folded GNR suddenly forms a round scroll-shaped structure (C6, **Figure 3.4**(f)), which has the lowest vdW interaction energy in **Figure 3.3**. After that, a periodic exchange between two configurations (C7, **Figure 3.4**(g) and C8, **Figure 3.4**(h)) is seen while the rotating E-field "squeezes" the round scroll structure resulting in spike-like changes in the vdW interaction (**Figure 3.3**).
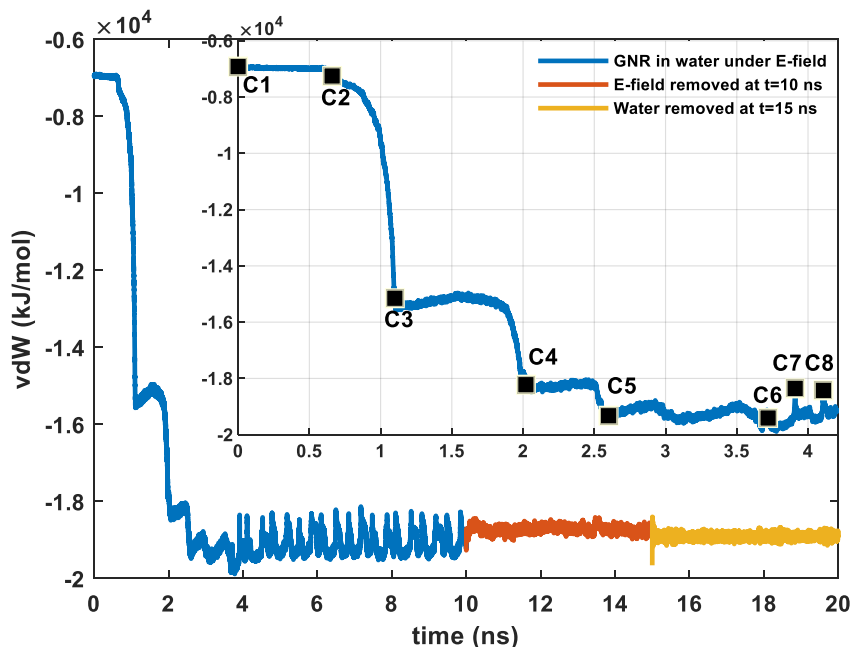
Figure 3.3. Time evolution of the vdW interaction energy profile of the GNR when it is immersed in water and subjected to a rotating E-field (t=0 to 10 ns), on removal of the E-field (t=10 ns to t=15 ns), further removal of the aqueous environment (t=15 ns to t= 20 ns). The inset shows the first 4200 ps of the same energy profile and the times at which significant configurations shown in **Figure 3.4** are formed.

(a) C1 (t=0 ps)   (b) C2 (t=660 ps)   (c) C3 (t=1100 ps)   (d) C4 (t=2020 ps)

(e) C5 (t=2600 ps)   (f) C6 (t=3720 ps)   (g) C7 (t=3910 ps)   (h) C8 (t=4109 ps)
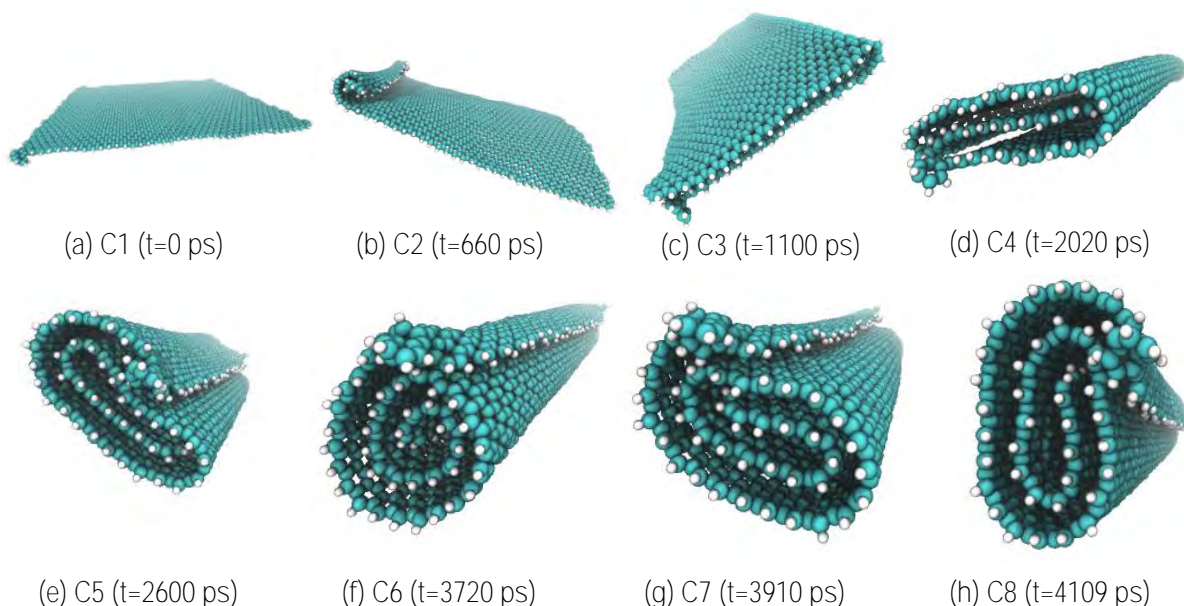
Figure 3.4. Snapshots of different configurations formed during the self-assembly of a 100.3 Å × 94.5 Å zigzag GNR with fixed prolonged edges on application of a rotating E-field.

38

In order to verify which configuration is the final result of this self-assembly process, the applied E-field is removed at t=10 ns and the trajectory calculated for a further 5 ns. The resulting GNS with a hollow inner core and round well-defined scroll structure is shown in **Figure 3.5** (C9). The constant vdW of the final structure as shown in **Figure 3.3** after t=10 ns reflects its stability. Further, the aqueous environment is removed at t=15ns and the structure simulated for another 5 ns. The structure retains the scroll topology shown in **Figure 3.5**. Thus, the proposed mechanism forms a stable GNS that does not unwind into a planar structure on removal of process conditions. For all the different studies conducted in the rest of this work, the final scroll structures shown have been produced after the subsequent removal of the applied E-field, requiring an extended simulation without an E-field for a finite amount of time, which we carried out for 5 ns to ensure the stability of the nanoscroll. As mentioned previously, this corresponds to the flat red portion of the energy profile shown in **Figure 3.3**. For the remaining studies in this work, the time variation of the energy profiles

(a) Lateral and front view of the final
      scroll structure (perspective)

(b) Lateral and front view of the final scroll structure (orthographic)
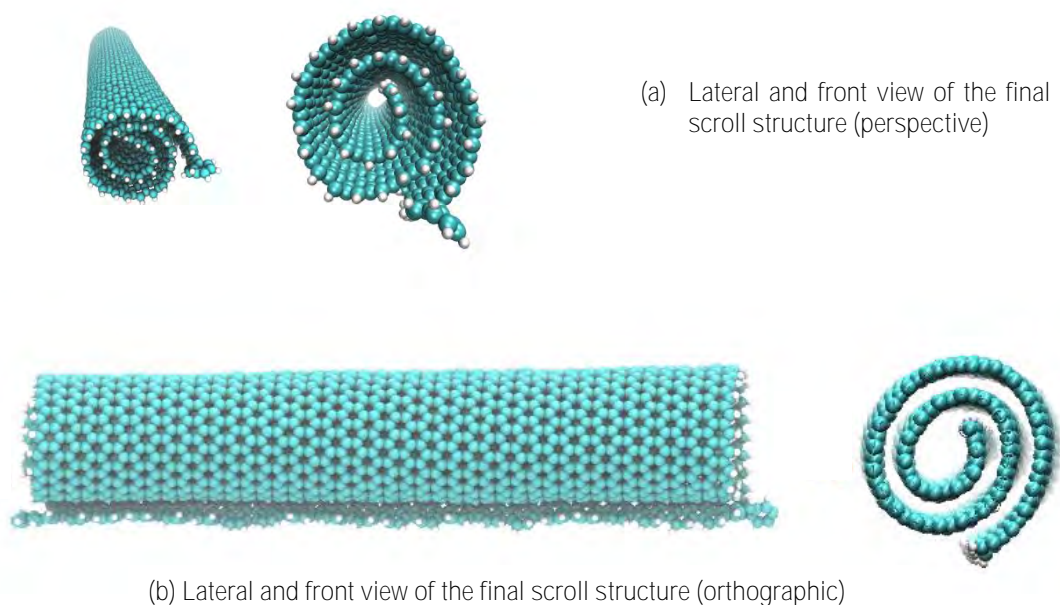
Figure 3.5. Final structure formed on removal of the applied rotating E-field as a result of the self-assembly of a 100.3 Å x 94.5 Å zigzag GNR with fixed prolonged edges.

are shown for the GNR structure under an applied E-field only, for the sake of clarity, and

only the average value of the vdW interaction energy of the final structures formed after the

subsequent removal of the E-field is mentioned since it remains constant over time.
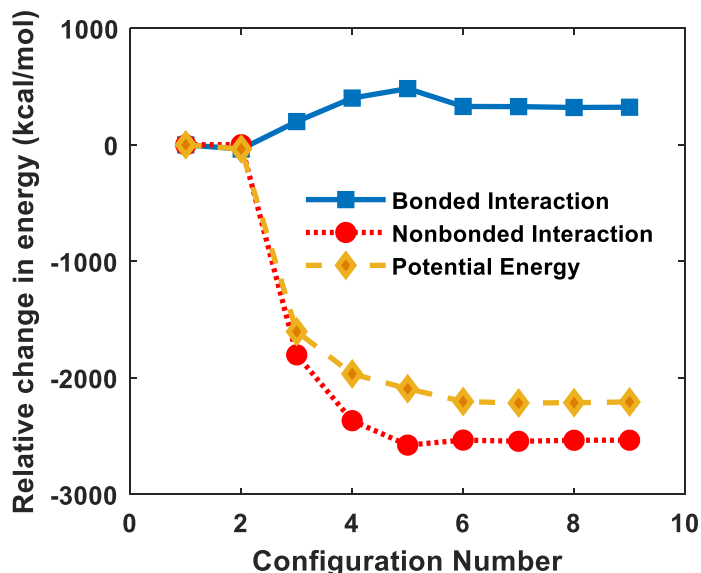
Figure 3.6. Changes in bonded interaction, non-bonded interaction and potential energy terms relative to an undistorted GNR with fixed prolonged edges during its self-assembly induced by a rotating E-field. Configuration number refers to the configurations shown in **Figure 3.4**.

To understand the energy origins of the structural evolution onset by the rotating E-field that

is depicted in **Figure 3.4**, we calculated the contribution of the bonded and non-bonded

interaction energy of the different configurations (C1 to C9) along with the total potential

energy of each. The results shown in **Figure 3.6** are the energy changes relative to the

undistorted GNR with fixed prolonged edges (C1, **Figure 3.4**(a)). Bonded interaction energy

is the sum of bond stretching potential, angle bending potential, dihedral torsion, inversion,

etc. Non-bonded interaction energy is the sum of vdW interaction energy and Coulombic

interaction energy, while the sum of bonded and non-bonded terms is the configuration's

potential energy. As described by Braga *et al.*, scroll formation is dominated by two significant energy contributions- an increase in elastic strain energy caused by the bending of the graphite sheet and the decrease in free energy generated by the vdW interaction of the overlapping graphene layers [8]. Any bending of the graphene sheet before a possible overlapping occurs must, therefore, be energy assisted. In our proposed method, the applied E-field provides the required energy in the initial bending of the GNR. As seen in **Figure 3.6**, there is an increase in the bonded interaction energy with the bending of GNR, indicating decreasing stability. However, when there is significant overlapping of the rotating GNR, there is a sharp fall in the non-bonded interaction energy upon a successful folding of the GNR, so that the overall process yields a more stable configuration than the initial GNR. On removal of the E-field after the formation of C8 (**Figure 3.4** (h)), the scroll structure is retained (C9, **Figure 3.5**).

To characterize the scroll structure formed using our proposed method (C9), we calculated the concentration profiles of the GNS formed along Y and Z directions. The concentration profiles along a specific direction are calculated by slicing the cubic box into evenly spaced slices parallel to the corresponding plane and determining the number of target atoms (whose concentration profile we want to calculate) in each slice. The results are plotted in **Figure 3.7**(a). The blue solid line represents the concentration profile of the GNS along the Y and the red dashed line along the Z direction. The similar concentration profiles along the two directions confirm the uniform morphology of the GNS formed by our proposed method. This is in contrast to previously reported experimental methods of GNS fabrication where the GNS

formed was of poor morphology and ill-defined layers. It is seen that there are five peaks along each curve. If we follow the front view of the GNS shown in **Figure 3.5**(b) along, for example, the Z direction from the positive axis to the negative axis, we encounter five graphene layers. Thus, each peak in the concentration profile along a specific axis represents a layer of the GNS and the distance between the peaks represents the interlayer distances. Here we define the distances d_1, d_2, and d_3 as the distance between adjacent peaks along each of Y and Z direction, moving from their negative to positive axes. The distances d_1, d_2, and d_3 measured along the Y direction are shown in **Figure 3.7**(a). The values of the distances are
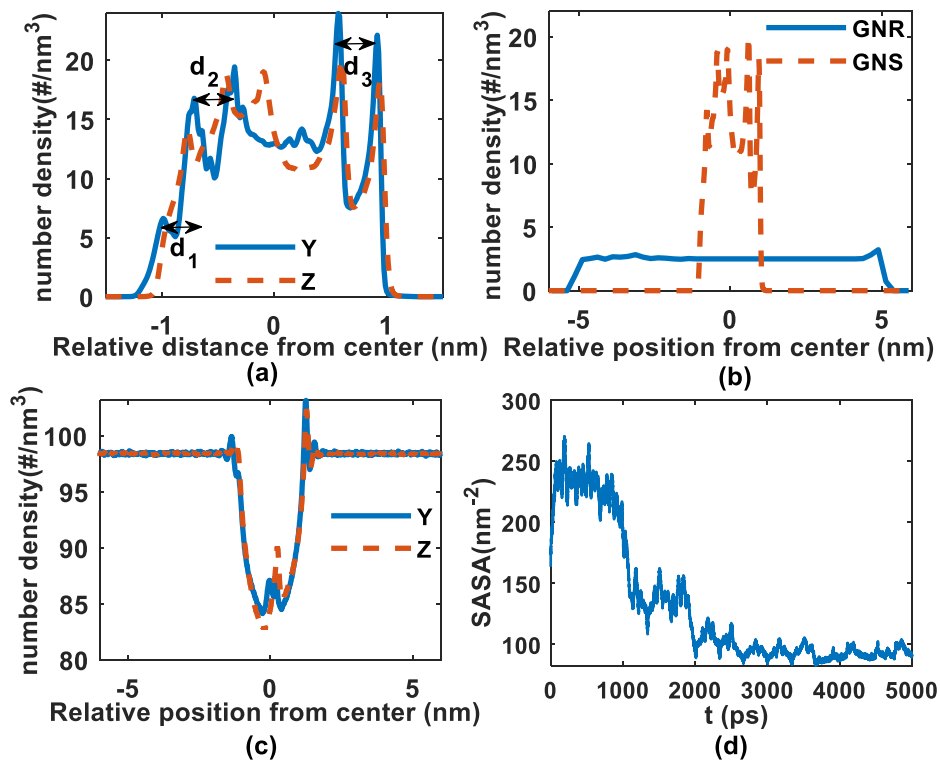
Figure 3.7. (a) Concentration profile of the GNS shown in **Figure 3.5** along the Y and Z direction. The distances d_1, d_2, and d_3 measured along the Y direction are shown in the figure. Distances along Z direction are not shown for clarity.(b) Concentration profile of the initial GNR and final GNS along the Z direction. (c) Concentration profile of the water molecules along the Y and Z direction after formation of the GNS. (d) Time evolution of the solvent accessible surface area (SASA) as the GNR assembles into a GNS.

Table 3-1 Interlayer distances (d_1, d_2, d_3), inner (d_i) and outer (d_o) diameters along with their corresponding averages (d, $d_i{'}$, and $d_o{'}$) of the GNS formed using our proposed method. Column 1 shows a front view of the scroll formed and definitions of the measured distances.

	Axes	Distance (nm)					Average (nm)		
		d_1	d_2	d_3	d_i	d_o	d	$d_i{'}$	$d_o{'}$
	Y	-	0.3592	0.3473	0.9219	1.9038	0.3448	0.8082	1.8080
	Z	0.3472	0.3353	0.3352	0.6945	1.7122			

shown in **Table 3-1**. All the measured distances in both Y and Z directions are larger than 3.4 Å, which is the shortest interlayer distance of the graphitic allotrope and thus have entered the strong-adhesive-binding region of the chemical bond. In addition, the inner (d_i) and outer diameter (d_o) of the GNS, taken as the distance between the innermost peaks and outer most peaks, respectively, are also shown. The small peak in the concentration profile along Y is attributed to the irregular scroll edge formed where the nanoribbon terminates and hence does not truly represent a layer of the scroll. Thus the corresponding distance measured d_1 is ignored in our results shown in **Table 3-1**. The concentration profiles thus further validate the stability of the scroll formed. **Figure 3.7**(b) shows the concentration profiles along Z direction of the initial GNR (blue solid line) along with that of the final GNS (red dashed line) representing the reorientation of the atoms along its length. **Figure 3.7**(c) shows the concentration profile of the water molecules along the Y and Z directions in the simulation box after the formation of the GNS. The dip in the water concentration profile at the center represents the hydrophobicity of the formed GNS. The same is also seen in **Figure 3.7**(d) which shows the solvent accessible surface area in the simulation box during the self-assembly of the GNR into a scroll. Initially, the nanoribbon structure offers a planar, wider area available to the water molecule which decreases as it scrolls into a more closed structure.

3.4. Changing Dimensions and Chirality of Initial GNR

To investigate the versatility of our proposed setup, we varied the dimensions of the initial GNR as well as its chirality and characterized the resulting scroll formed in each case.

3.4.1. Changing Width for Fixed Length of GNR

Specifically, at first, the length of a zigzag GNR (L) was kept fixed at 100.3 Å while its width (W) was varied over 17.8 Å to 94.5 Å. A rotating E-field of 20 Gr.p.m. angular frequency and 1 V/nm strength was applied for a simulation time of 15 ns. The resulting final structures formed after the removal of the E-field are shown in **Figure 3.8**. The full simulation video of the individual simulation trajectories superimposed on each other (W_1= 17.8 Å (blue) , W_2= 26.2 Å (red), W_3= 34.9 Å (yellow), W_4= 43.4 Å (green), W_5= 51.9 Å (cyan), W_6= 60.4 Å (purple), and W_7= 94.5 Å (brown)) may be found as "**Supporting Movie 3**" in [130]. Since the GNR rolls along the direction of its length, the resulting nanoscrolls each have the same number of graphene layers but are of different lengths which is equal to the width of the initial GNR. The change in the vdW interaction energy profile of the GNRs under an applied E-field is shown in **Figure 3.9**(a). Since the vdW interaction energy invariably increases with the increase in the number of atoms in the structure, the profiles shown are calculated for the vdW interaction energy per carbon atom in the structure. A sharp fall in the energy profile is seen in each case which shows the resulting scroll structures are more stable than the initial planar ribbon. As explained previously, a sharp fall indicates the formation of a folded structure while nanoscroll formation occurs at the onset of spike-like changes in the energy profile. The profiles for the wider GNRs depict a more visible stepwise change compared to that for the narrower GNRs. This is because a wider GNR forms more slowly than a narrower GNR, and each folded structure (formed in the course of the self-assembly) follows the E-field for a

comparatively longer period of time, resulting in a stepwise fall in the vdW interaction energy profile. **Figure 3.9**(b) shows the average vdW interaction energy per carbon atom of the final structure formed after the subsequent removal of the E-field against the corresponding width of the initial GNR. It is observed that the scroll morphology formed for a wider GNR is more stable than that for a narrower GNR, while they have the same number of scroll-turns (since the initial length of the GNR is constant).
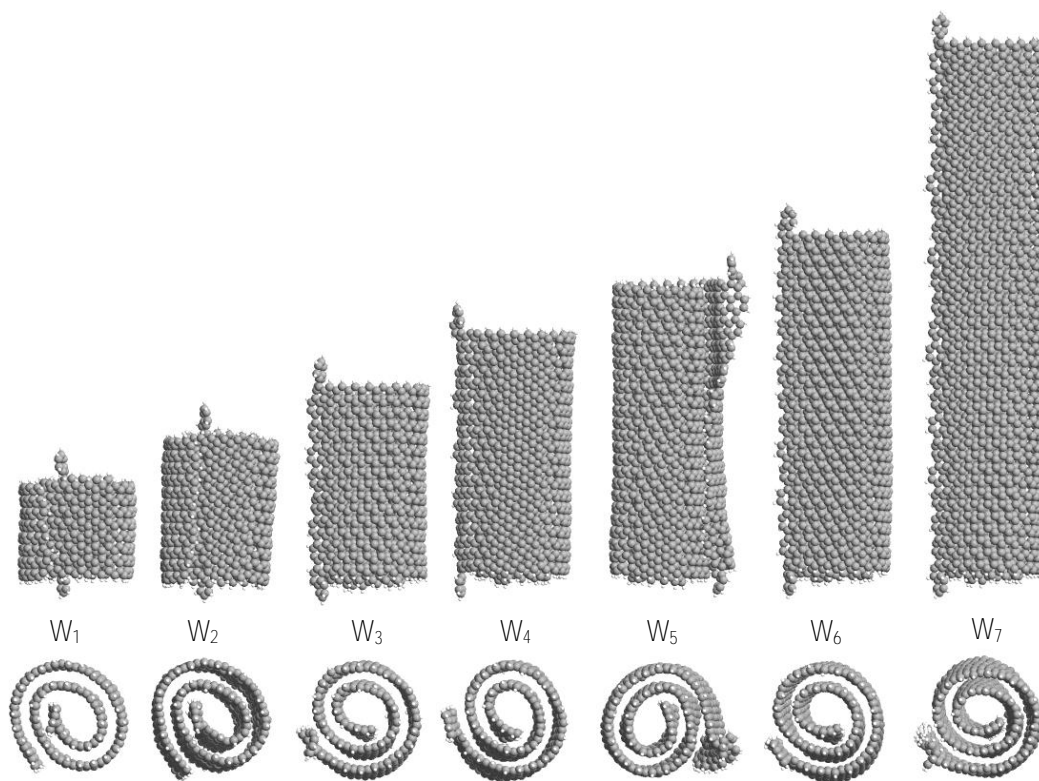
Figure 3.8. Scrolls formed from initial GNRs with the same length (100.3 Å) but varying width. (Left to right) W_1= 17.8 Å, W_2= 26.2 Å, W_3= 34.9 Å, W_4= 43.4 Å, W_5= 51.9 Å, W_6= 60.4 Å, and W_7= 94.5 Å. Both the lateral and front view of the final structures are shown.

To further validate the structure of the scrolls formed due to changing width of the initial GNR, we calculated their concentration profiles along the Y (**Figure 3.10**(a)) and Z (**Figure 3.10**(b)) directions. The measured distances between adjacent peaks (d_1, d_2, d_3) as well as distance between innermost (d_i) and outermost peaks (d_o) are shown in **Table 3-2**. As explained previously, d_1, d_2, d_3 represent the interlayer distances whereas d_i and d_o represent the inner and outer diameter of the scroll structure. The average interlayer distance (d) of each structure is ~3.4 A, thus proves the existence of a strong force between the layers. It appears that the outer diameter of the scrolls slightly changes with the increasing width of the GNR.
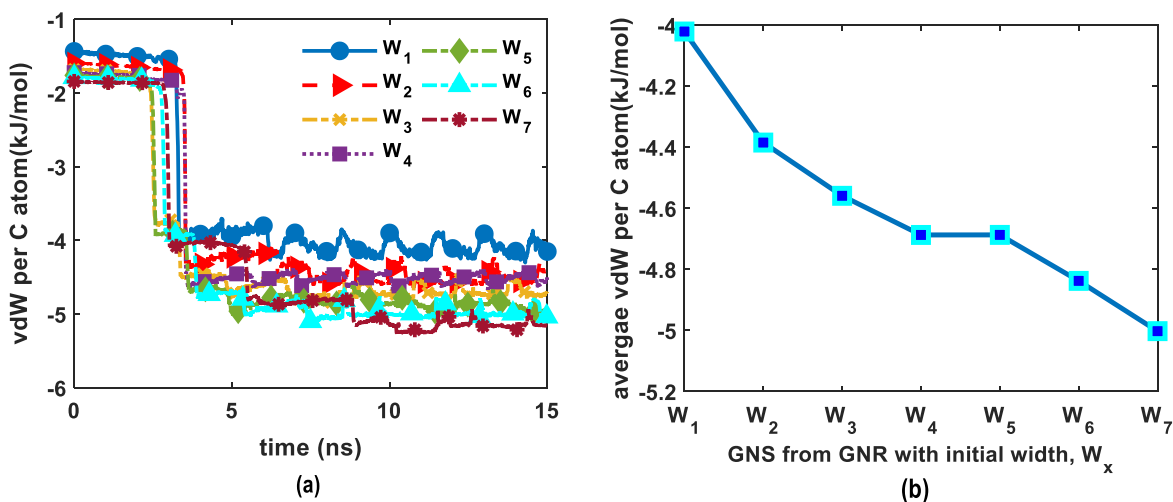
Figure 3.9. (a) Time evolution of the vdW interaction energy per carbon atom of GNRs of equal length (100.3 Å) and different widths (W_1-W_7) under an applied rotating E-field. (b) Average vdW interaction energy per carbon atom of the corresponding final structures formed after removal of E-field.
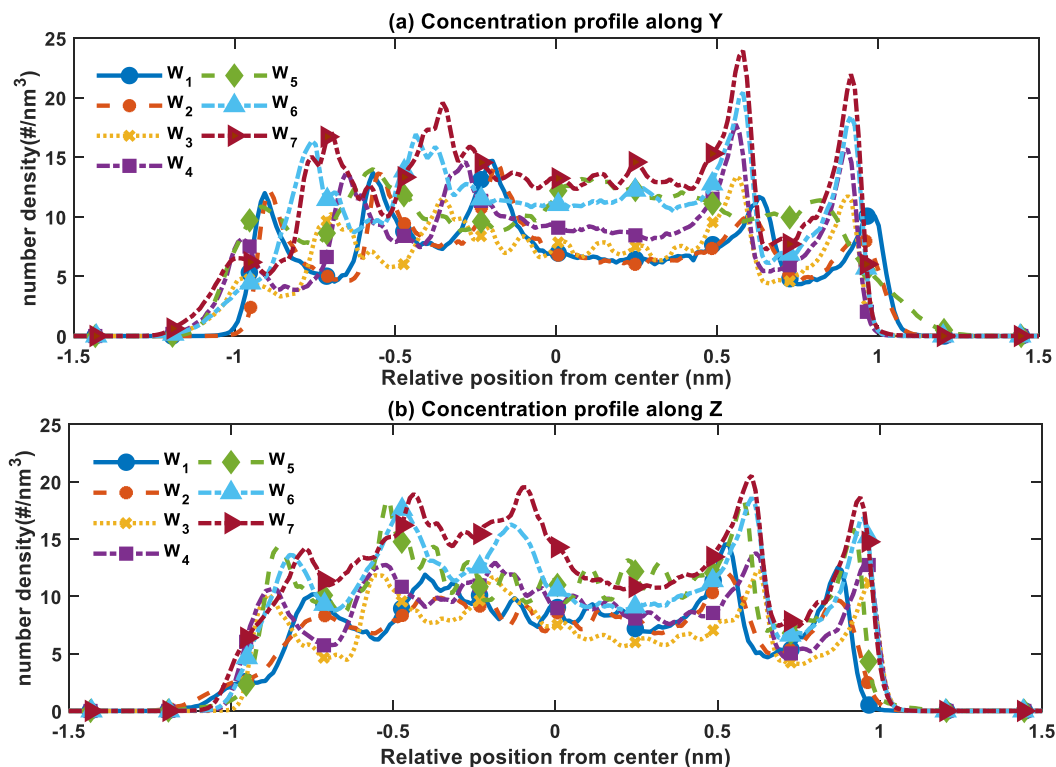
Figure 3.10. Concentration profiles of the scrolls formed from varying width of GNRs while their lengths are kept at 100.3 Å. The values of the width are: W_1= 17.8 Å, W_2= 26.2 Å, W_3= 34.9 Å, W_4= 43.4 Å, W_5= 51.9 Å, W_6= 60.4 Å and W_7= 94.5 Å.

Table 3-2 Interlayer distances (d_1, d_2, d_3), inner (d_i) and outer (d_o) diameters along with their corresponding averages (d, d_i', and d_o') of the different GNSs formed by varying the initial GNR width while its length is kept fixed at 100.3 Å. The dash represents a distance which is ignored because it is measured relative to a small peak formation in the concentration profile that represents an edge where the GNS terminates.

Width	Axes	Distances (nm)					Average (nm)		
		d_1	d_2	d_3	d_i	d_o	d	d_i'	d_o'
W_1	Z	-	0.3480	0.3361	0.9362	1.8244	0.3481	0.8822	1.8544
	Y	0.3361	0.3721	0.3481	0.8281	1.8844			
W_2	Z	-	0.3585	0.3346	0.8843	1.9284	0.3466	0.8365	1.8784
	Y	0.3346	0.3705	0.3346	0.7887	1.8284			
W_3	Z	0.3240	0.3720	0.3360	0.8160	1.8480	0.3456	0.8640	1.8600
	Y	-	0.3480	0.3480	0.9120	1.8720			
W_4	Z	0.3478	0.3358	0.3358	0.8035	1.8229	0.3438	0.8215	1.8529
	Y	-	0.3718	0.3478	0.8395	1.8829			
W_5	Z	-	0.3358	0.3358	1.1032	1.7748	0.3418	1.0552	1.7568
	Y	-	0.3478	0.3478	1.0073	1.7388			
W_6	Z	0.3471	0.3351	0.3471	0.7419	1.7712	0.3375	0.8796	1.8066
	Y	-	0.3231	0.3351	1.0172	1.8419			
W_7	Z	0.3352	0.3472	0.3352	0.6944	1.7120	0.3400	0.8141	1.8078
	Y	-	0.3472	0.3352	0.9339	1.9036			

3.4.2. Changing Length for Fixed Width of GNR
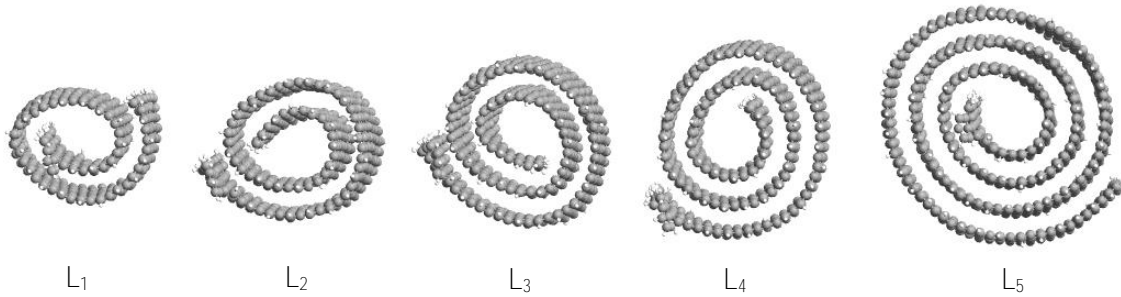
Figure 3.11. Scrolls formed from initial GNRs with the same width (44.4 Å) but varying lengths. (Left to right) L_1= 59.7 Å, L_2= 86.8 Å, L_3= 105.2 Å, L_4= 126.2 Å, and L_5= 207.4 Å. Only the front view of the final structures are shown.

After that, we varied the length of the initial GNR over 59.7 Å to 207.4 Å while its width is kept fixed at 44.4 Å and subjected each to a rotating E-field of 30 Gr.p.m. angular frequency and 1 V/nm strength for 10 ns. The resulting final structures formed after the subsequent removal of the E-field are shown in **Figure 3.11**. The sharp fall in the vdW energy profile shown in **Figure 3.12**(a) for each GNR represents the stability of the final structures for each
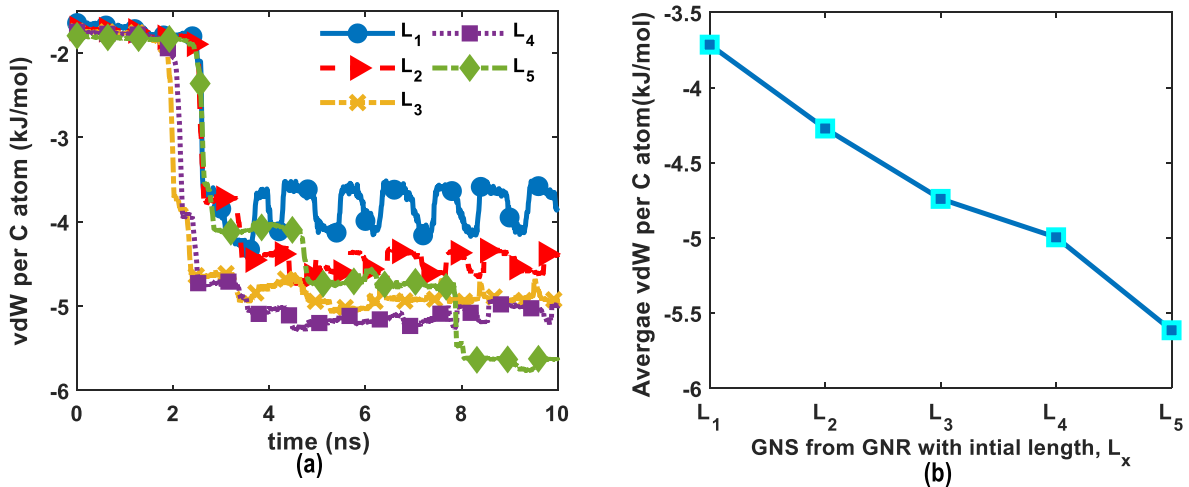
Figure 3.12. (a) Time evolution of the vdW interaction energy per carbon atom of GNRs of equal widths (44.4 Å) and different lengths (L1- L5) under an applied rotating E-field. (b) Average vdW interaction energy per carbon atom of the corresponding final structures after the removal of E-field.

48

length. The stepwise change for the longer GNRs relates to their longer time of formation, as explained previously. Thus, both single-layered and multi-layered GNS can be formed using our proposed method. The average vdW interaction energy per carbon atom of the scrolls formed for GNRs with varying lengths is shown in **Figure 3.12**(b). Since the values are shown for the vdW interaction energy per carbon atom of the structures, the negative slope of the curve in **Figure 3.12**(b) symbolizes the increasing stability of the morphology of the scroll as the number of scroll turns increases. An increasing length, of course, causes a higher number of scrolled layers in the final structure as seen in **Figure 3.11** as well as in the number of peaks in the concentration profiles shown in **Figure 3.13**. For example, there are only three peaks in the concentration profile along the Z direction for the GNS formed from a GNR with length L_1, thus there is only one measured distance, d_1 shown in **Table 3-3**. On the other hand, there are seven peaks in the corresponding profile for the case with initial length, L_5, thus resulting in five measured distances, d_1 to d_5. All the structures yield a stable configuration as seen by the average interlayer distance (d) shown in **Table 3-3**.The outer diameter of the scrolls also increases with the increasing length and vary from 13.7 Å to 27.2 Å for the lengths used in this study.
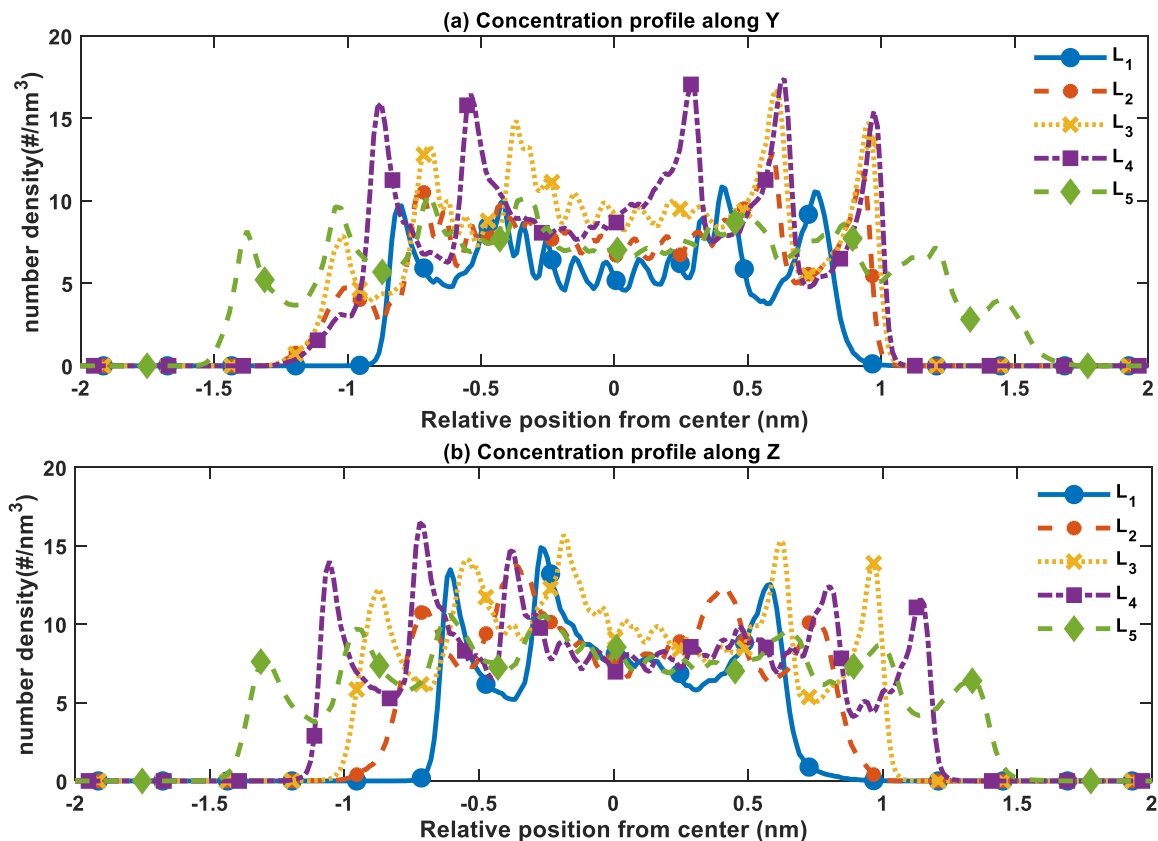
Figure 3.13. Concentration profiles of the scrolls formed from varying lengths of GNRs while their widths are kept at 44.4 Å. The values of the lengths are: L_1= 59.7 Å, L_2= 86.8 Å, L_3= 105.2 Å, L_4= 126.2 Å, and L_5= 207.4 Å.

Table 3-3 Interlayer distances (d_1, d_2, d_3, d_4, d_5), inner (d_i) and outer (d_o) diameters along with their corresponding averages (d, d_i', and d_o') of the different GNSs formed by varying the initial GNR length while its width is kept fixed at 44.4 Å. The dash represents a distance which is not applicable since number of scroll-turns vary with length of the GNR.

| Length	Axes	Distance (nm)							Average (nm)		
		d_1	d_2	d_3	d_4	d_5	d_i	d_o	d	d_i'	d_o'
L_1	Y	0.3841	0.3481	-	-	-	0.8162	1.5484	0.3561	0.8342	1.3683
	Z	0.3360	-	-	-	-	0.8522	1.1882			
L_2	Y	0.3001	0.3359	-	-	-	1.3078	1.9438	0.3320	1.0498	1.6978
	Z	0.3360	0.3240	-	-	-	0.7918	1.4518			
L_3	Y	0.3238	0.3241	0.3481	-	-	0.9723	1.9683	0.3381	0.8883	1.9025
	Z	0.3241	0.3601	0.3481	-	-	0.8043	1.8366			
L_4	Y	0.3355	0.3495	0.3355	-	-	0.8248	1.8453	0.3377	1.0065	2.0197
	Z	0.3351	0.3355	0.3352	-	-	1.1882	2.1940			
L_5	Y	0.3300	0.3523	0.3523	0.3964	0.3301	0.8149	2.8190	0.3478	0.8590	2.7195
	Z	0.3300	0.3524	0.3523	0.3523	0.3300	0.9030	2.6200			

3.4.3. Changing Chirality of Initial GNR

In this section, we used GNRs of approximately the same dimensions but of different chirality and applied a rotating E-field of 30 Gr.p.m. angular frequency and 1 V/nm strength. By varying the chirality of the initial GNR, the chirality of the GNS can be controlled [18]. In **Figure 3.14**, the top row shows part of a zigzag type GNR (chiral angle 0°), an armchair type GNR (chiral angle 30Å) along with some chiral GNRs (chiral angle 5°, 10°, 15°, 20°, and 25°). The bottom row shows the GNSs formed from the corresponding GNR which retains the chirality of the initial planar structure. The variation in the vdW interaction energy profile over time for each chirality of the initial GNR is shown in **Figure 3.15**(a); each final structures is more stable than the initial planar structure. The average vdW interaction energy per carbon atom of the final structures is shown in **Figure 3.15**(b). It is seen that there is little variation in the average vdW interaction energy which reflects that the morphologies of the structures are of comparable stability. The concentration profiles for each structure along the Y and Z
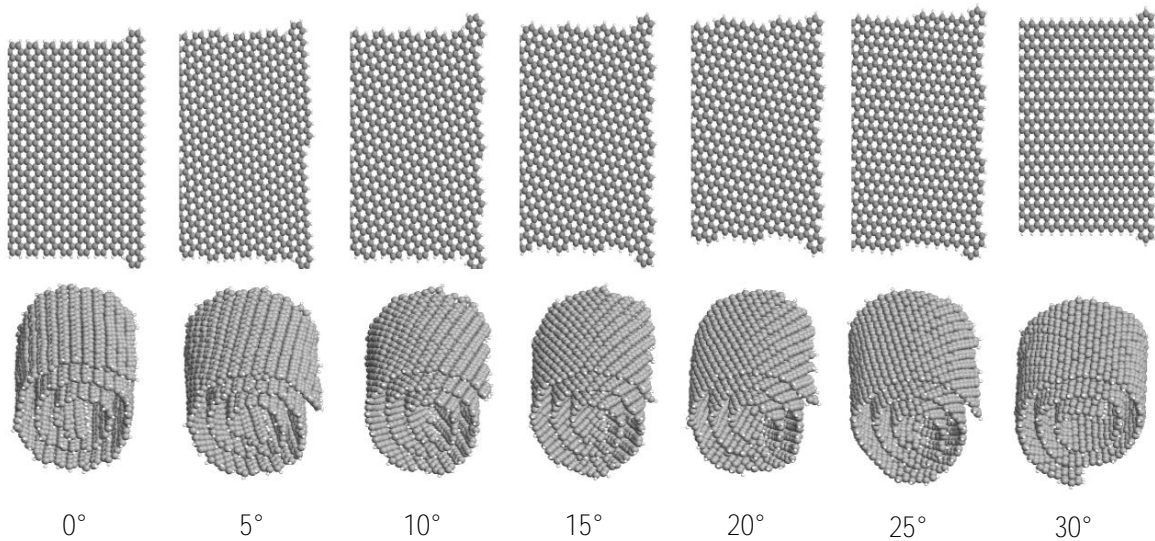
| 0° | 5° | 10° | 15° | 20° | 25° | 30° |

Figure 3.14. Scrolls formed from initial GNRs with approximately the same dimensions but of different chiral angle: (Left to Right) 0°, 5°, 10°, 15°, 20°, 25°, and 30°. The top row shows a portal of the initial GNR structure while the bottom row shows an oblique view of the corresponding scroll structure.

directions are shown in **Figure 3.16**, while **Table 3-4** lists the measured characteristic distances. All types of chiral GNSs formed using our proposed method are stable 1-D configurations since the average interlayer distance (*d*) in each case enters the strong-adhesive-binding regime.
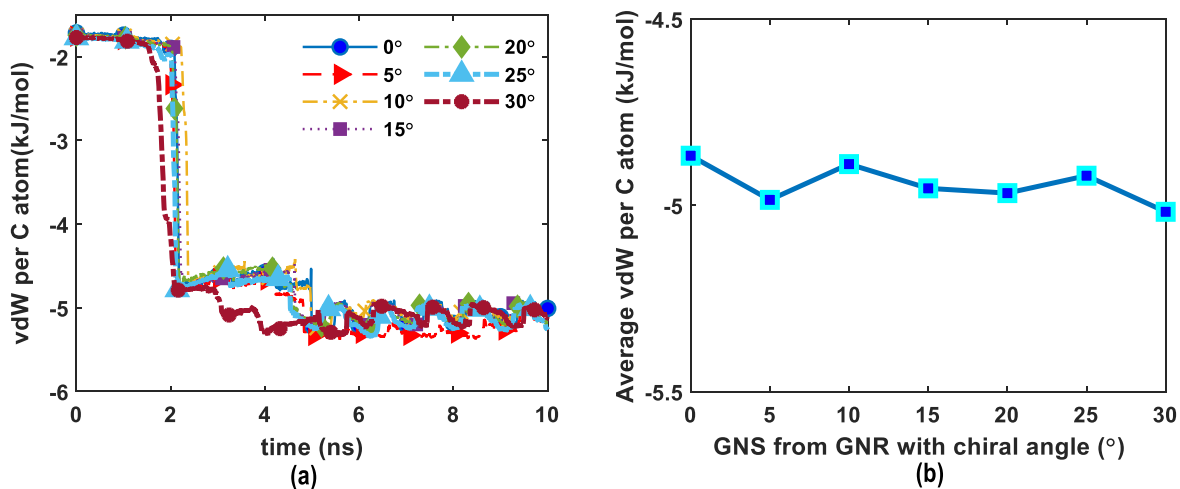
Figure 3.15. (a) Time evolution of the vdW interaction energy per carbon atom of GNRs of approximately equal dimensions but varying chirality under an applied rotating E-field. (b) Average vdW interaction energy per carbon atom of the corresponding final structures.
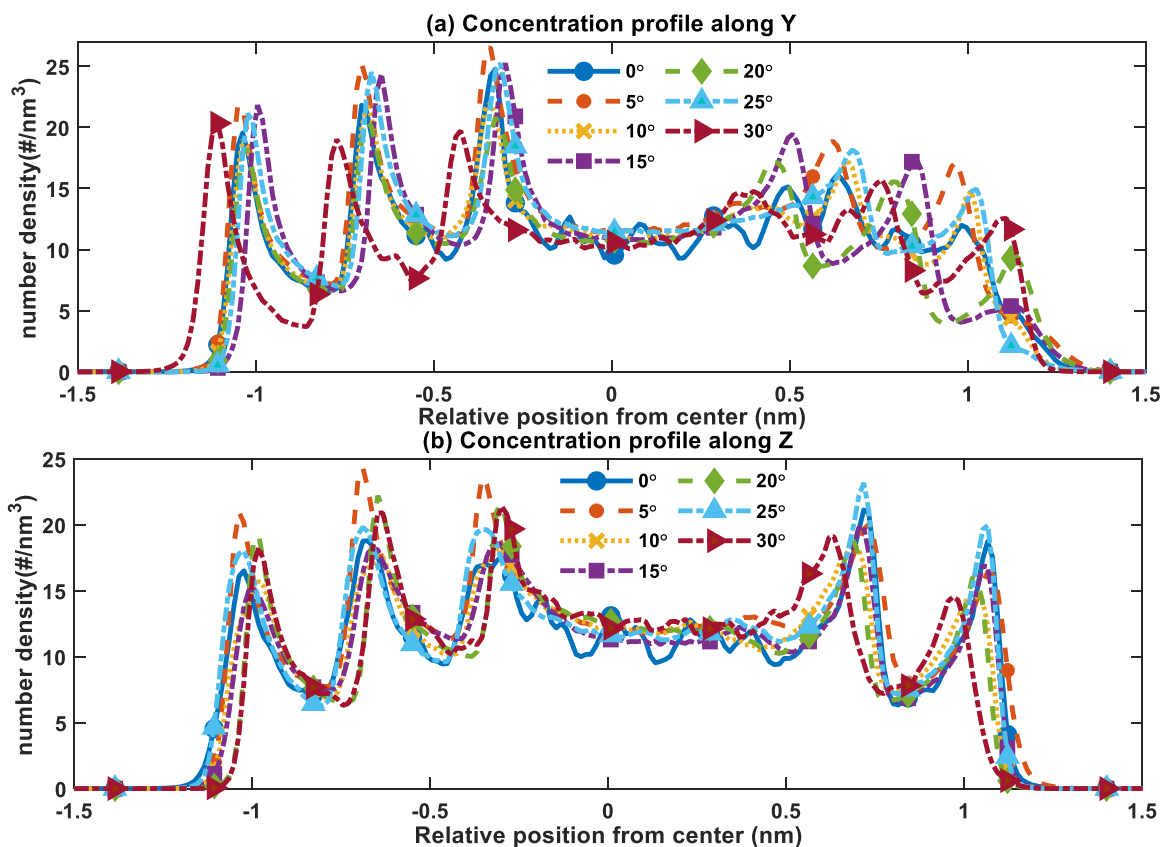
Figure 3.16. Concentration profiles of the scrolls formed from GNRs with various chiral angles while their dimensions are kept approximately same.

Table 3-4 Interlayer distances (d_1, d_2, d_3), inner (d_i) and outer (d_o) diameters along with their corresponding averages (d, d_i', and d_o') of the different GNSs formed by varying the chirality of the initial GNR length while its dimensions (length, L and width, W) are kept approximately fixed.

(n,m)	Angle(°)	L (nm)	W (nm)	Axes	d_1	d_2	d_3	d_i	d_o	d	d_i'	d_o'
(20,0)	0	126.51	48.65	Y	0.3338	0.3760	0.3481	0.9608	2.0187	0.3549	0.9887	2.0534
				Z	0.3477	0.3759	0.3479	1.0165	2.0880			
(20,2)	5	130.63	52.54	Y	0.3347	0.3621	0.3482	0.9609	2.0059	0.3436	1.0236	2.0545
				Z	0.3487	0.3342	0.3339	1.0862	2.1030			
(20,5)	10	123.53	52.27	Y	0.3481	0.3479	0.3479	1.0021	2.0460	0.3433	0.9951	2.0251
				Z	0.3341	0.3479	0.3341	0.9881	2.0042			
(20,8)	15	123.59	50.98	Y	0.3480	0.3480	0.3480	0.8074	2.1303	0.3434	0.9188	2.0883
				Z	0.3341	0.3480	0.3341	1.0301	2.0463			
(20,11)	20	124.10	48.21	Y	0.3339	0.3619	0.3202	0.7936	2.1440	0.3387	0.8910	2.0743
				Z	0.3341	0.3481	0.3339	0.9884	2.0045			
(20,15)	25	125.42	51.94	Y	0.3484	0.3622	0.3484	0.9890	2.0480	0.3437	1.0308	2.0620
				Z	0.3345	0.3343	0.3346	1.0726	2.0760			
(20,20)	30	126.17	47.65	Y	0.3340	0.3482	0.3479	0.8218	2.2140	0.3411	0.8776	2.0820
				Z	0.3482	0.3343	0.3342	0.9333	1.9500			

3.5. Changing Applied E-field Properties

In our proposed method, we have used a rotating E-field to induce the self-assembly of a GNR into a scroll structure. At this point, we would like to elucidate the effect of the applied E-field properties, namely its angular frequency and strength on the scrolling mechanism.

3.5.1. Changing Angular Frequency of Applied E-field

In order to study the effect of angular frequency of the applied E-field upon the scrolling mechanism of a GNR with prolonged fixed edges, we applied rotating E-fields of 1 V/nm strength but different angular frequencies ranging from 10 Gr.p.m. to 100 Gr.p.m. in 10 Gr.p.m. steps and also ultra-fast speeds of 150 Gr.p.m. to 350 Gr.p.m. in 50 Gr.p.m steps to a 100.3 Å × 34.9 Å GNR structure immersed in water for simulation times of 30 ns for 10 Gr.p.m., 15 ns for 20 Gr.p.m. and 10 ns for the rest of the angular frequencies. Our results show that while the trajectory of the GNR during its self-assembly might follow three different regimes depending on the angular frequency of the rotating E-field, the final structure formed is fairly independent of the angular frequency and resembles a scroll structure under all conditions. It is found that during the scrolling motion, the GNR can follow the rotating E-field up to a certain angular frequency after which it starts to lag behind. A similar phenomenon was reported for a CNT immersed in water under a rotating E-field [21]. The maximum frequency up to which the GNR is "locked" with the applied E-field is called the locked frequency and for the GNR under simulation, it is about 30 Gr.p.m. **Figure 3.17** shows the snapshots at quarterly time intervals for one time period of each simulation trajectories under 10 Gr.p.m. (cyan), 60 Gr.p.m. (red) and 300 Gr.p.m. (green). The three different trajectories identified during the self-assembly of the GNR are classified according to whether the angular frequency is below the locked frequency (Regime A), slightly above the locked

frequency (Regime B) or much higher than the locked frequency (Regime C). The frequencies selected for representing the three regimes in **Figure 3.17** have been chosen accordingly. Since 10 Gr.p.m. is below the locked frequency of the GNR under study, it is successfully "locked" with the direction of the applied E-field and thus can also be used to represent the direction of the E-field in each frame. It is noticeable that the GNR marked red (60 Gr.p.m.) and green (300 G r.p.m.) lags behind the GNR marked cyan (10 Gr.p.m.) in each snapshot. The GNR marked cyan successfully completes one complete rotation in one time period of the corresponding angular frequency and is also seen to form a double folded structure in the final frame (Regime A). The GNR marked red also follows a rotational motion about its fixed edge, however, is always a certain angle behind the E-field it is trying to follow (Regime B). On the other hand, the GNR marked green does not leave the first quadrant in one time period. The superimposed trajectories of the GNR under these three frequencies of applied E-field (10 Gr.p.m. (cyan), 60 Gr.p.m.(red) and 300 G r.p.m. (green)) can be found titled "**Supporting Movie 4**" in [130]. The initial frames clearly distinguish between the complete rotational motion of the cyan and red marked GNR from the irregular, jerking motion of the GNR marked green. The simulation video also serves to show that the final structures formed as a result of the trajectories in the three different regimes all resemble a scroll-like formation. While trajectories in regime A and B follow the sequential structural evolution depicted in **Figure 3.4**, the GNR under a very high frequency such as the one marked green suddenly assembles into a scroll structure.

The variable E-field angular frequency study was repeated for GNR structures of different dimensions. The locked frequency for GNR structures of length 100.3 Å and widths 17.8 Å and 94.5 Å are found to be 15 Gr.pm. and 92 Gr.p.m. respectively. Thus, a wider GNR is able

to follow a faster rotating E-field. The range of frequencies over which the different trajectory regimes are identified for different size of the initial GNR are noted in **Table 3-5**.

(a) t= T/4

(b) t= T/2

(c) t= 3T/4

(d) t= T
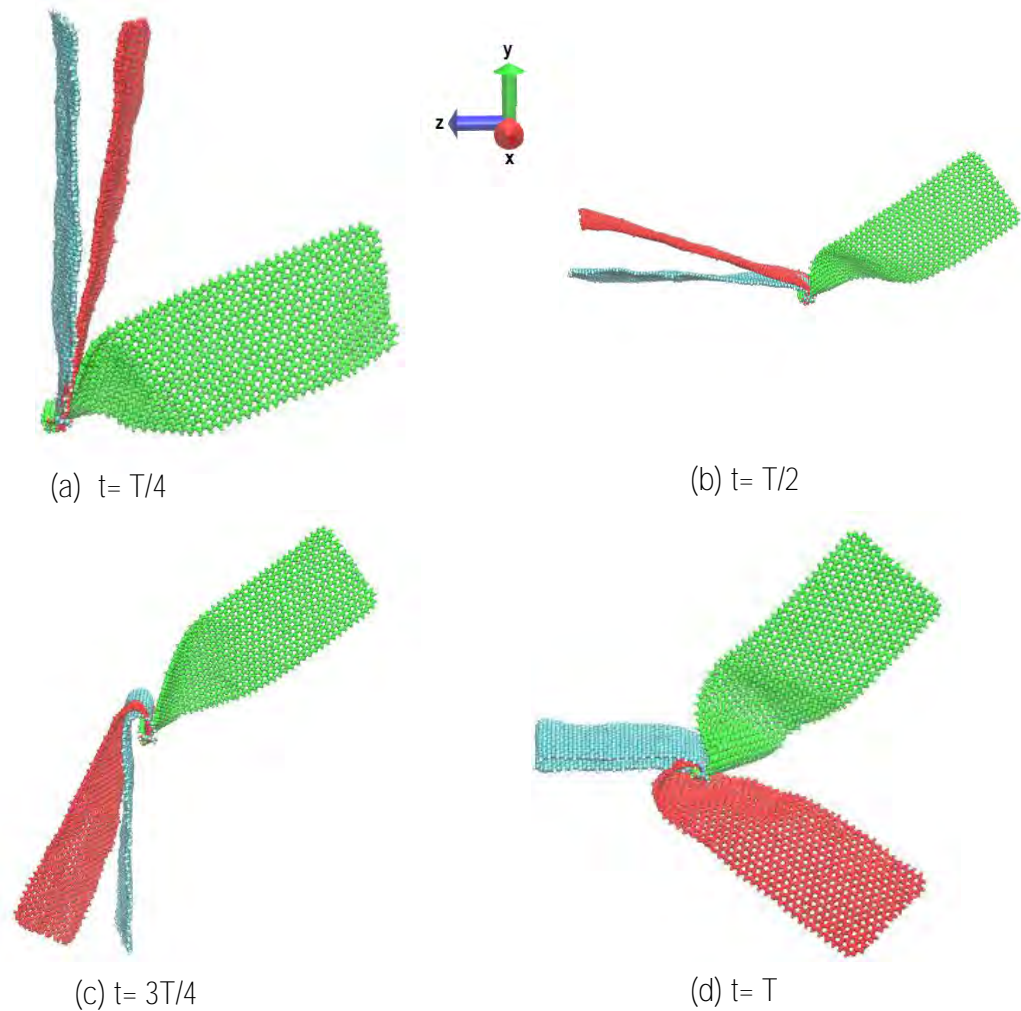
Figure 3.17. Snapshots showing a 100.3 Å × 34.9 Å GNR under rotating E-fields of three different angular frequencies at quarterly intervals of the corresponding time periods (T): GNRs colored cyan, red and green represent the trajectories under 10 Gr.p.m., 60 Gr.p.m., and 300 Gr.p.m. respectively. At 10 Gr.p.m. (cyan), the GNR also represents the predicted position of the E-field since it is below the "locked" frequency; at 60 Gr.p.m. (red), GNR lags the E-field and at 300 Gr.p.m. (green), GNR follows a jerky trajectory.

Table 3-5 Range of frequencies over which the three different trajectory regimes are identified for varying sizes of the initial GNR

Width of 100.3 Å long GNR (Å)	Regime A	Regime B	Regime C
17.8	<10 Gr.pm.	10-60 Gr.p.m.	>60 Gr.p.m.
26.3	< 20 Gr.p.m.	20-60 Gr.p.m.	>60 Gr.p.m.
34.9	< 30 G.r.p.m.	30-70 Gr.p.m.	>70 Gr.p.m.
43.4	< 40 Gr.p.m.	40-100 Gr.p.m.	>100 Gr.p.m.
51.9	< 60 Gr.p.m.	60-150 Gr.p.m.	>150 Gr.p.m.

Figure 3.18 shows the final structures formed under the different angular frequencies applied to a 100.3 Å x 34.9 Å GNR. We were able to identify two types of scroll formed as the final structures depending on whether the fixed edge of the initial GNR forms the inner (Scroll type A, **Figure 3.18** (b)) or outer (Scroll type B, **Figure 3.18**(d)) edge along the length of the final GNS. For slower frequencies below the locked frequency of the GNR structure under study, we found scroll type B to be predominant (**Figure 3.18**(c)- 10 Gr.p.m. (cyan), 20 G r.p.m. (blue)) while for frequencies in regime B, scroll type A (**Figure 3.18**(a)-40 Gr.p.m. (cyan), 50 Gr.p.m. (blue), 60 Gr.p.m. (red)) was found to be predominant. However, the final structure formed under frequencies in regime C were found to be both scroll type A and B. This may be related to their ultrafast, sudden formation after a haphazard, jerky rotation of the initial GNR. The time evolution of the vdW interaction energy profile for two types of scroll structures A (under 40 Gr.p.m.) and B (under 10 Gr.p.m.) is shown in **Figure 3.19**. The average vdW interaction energies of the final structures formed, Scroll Types A and B, are -6552.79 kJ/mol and -6493.59 kJ/mol, in that order.
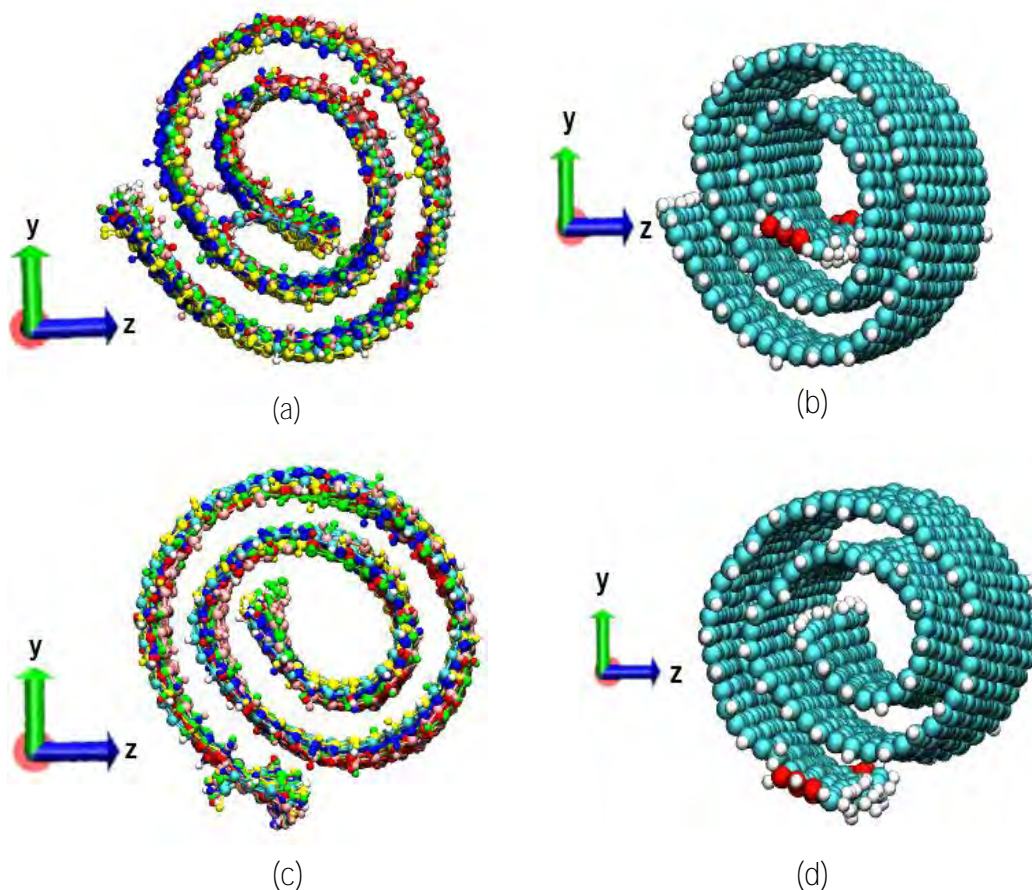
Figure 3.18. (a) GNSs with fixed edge of the initial GNR inside the final structure formed under various angular frequencies of applied rotating E-field of 1 V/nm strength: **40 Gr.p.m**. (cyan), 50 Gr.p.m. (blue), 60 Gr.p.m. (red), 80 Gr.p.m. (yellow), 100 Gr.p.m. (green), 250 Gr.p.m. (pink). Figure shows the front view of the structures. (b) The angular view for the GNS formed under 40 Gr.p.m. is shown with the prolonged edges marked red to indicate the position of the fixed edge inside the scroll (Scroll type A). (c) GNSs with fixed edge of the initial GNR outside the final structure formed under various angular frequencies of applied rotating E-field of 1 V/nm strength: **10 Gr.p.m. (cyan)**, 20 G r.p.m. (blue), 70 G r.p.m. (red), 200 G r.p.m. (yellow), 300 G r.p.m. (green), 350 G r.p.m. (pink). Figure shows the front view of the structures. (d) The angular view for the GNS formed under 10 Gr.p.m. is shown with the prolonged edges marked red to indicate the position of the fixed edge outside the scroll (Scroll type B).
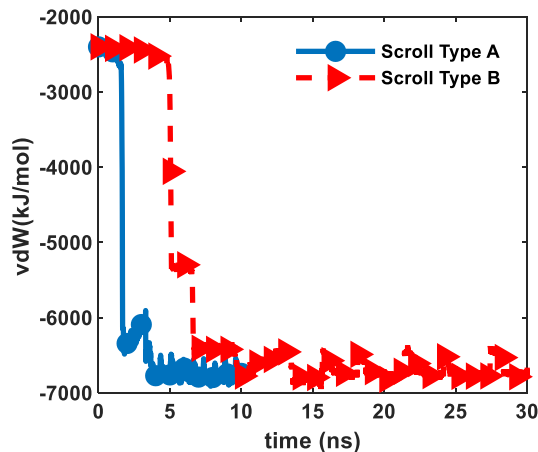
Figure 3.19. Time evolution of the vdW interaction energy of GNRs under applied rotating E-fields of angular frequencies 40 Gr.p.m. and 10 Gr.p.m. as they assemble into Scroll Types A (blue solid line with round markers) and B (red dashed line with triangular marker), respectively. The average vdW interaction energies of the final structures formed, Scroll Types A and B, are -6552.79 kJ/mol and -6493.59 kJ/mol, in that order.

Finally, we calculated the concentration profiles along the Y and Z direction of the final structures formed under each angular frequency. **Figure 3.20** shows the concentration profiles for the scroll formed under 40 Gr.p.m. (Scroll type A) and under 10 Gr.p.m. (Scroll type B), while **Table 3-6** lists the measured distances from the concentration profiles under each
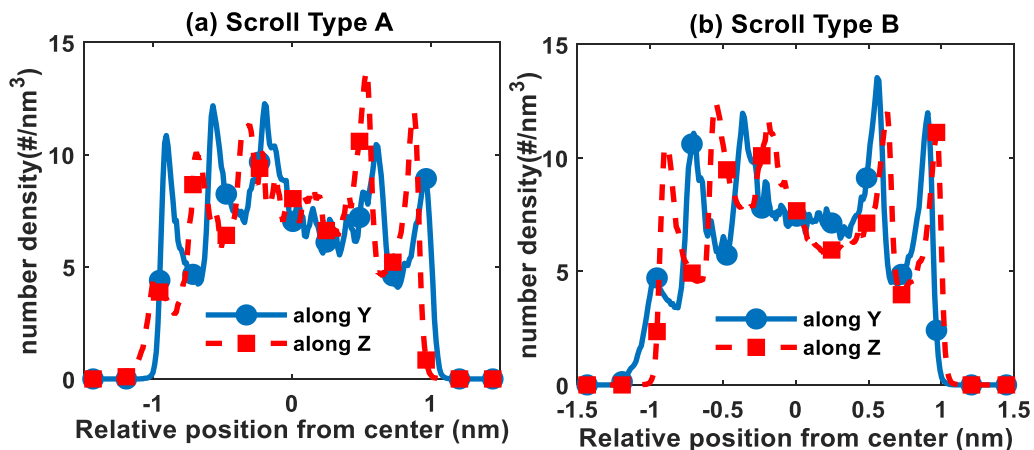
Figure 3.20. Concentration profiles of the scrolls formed under different angular frequencies of applied E-field. (a) Scroll Type A shown for 40 G r.p.m. and (b) Scroll Type B formed under 10 Gr.p.m. angular frequency.

Table 3-6 Interlayer distances (d_1, d_2, d_3), inner (d_i) and outer (d_o) diameters along with their corresponding averages (d, d_i', and d_o') of the different GNSs formed under different angular frequencies of a rotating E-field of 1 V/nm strength. The dash represents a distance which is ignored because it is measured relative to a small peak formation in the concentration profile that represents the edge where the GNS terminates.

Angular Frequency (G r.p.m.)	Axes	Distance (nm) (a) Scroll Type A					Average (nm)		
		d_1	d_2	d_3	d_i	d_o	d	d_i'	d_o'
40	Y	0.3359	0.3719	0.3479	0.8039	1.8596	0.3575	0.8219	1.8657
	Z	-	0.3840	0.3480	0.8398	1.8717			
50	Y	0.3359	0.3719	0.3358	0.8157	1.8593	0.3407	0.8697	1.8533
	Z	-	0.3358	0.3239	0.9237	1.8473			
60	Y	0.3480	0.3599	0.3480	0.8279	1.8838	0.3504	0.8639	1.8778
	Z	-	0.3480	0.3480	0.8998	1.8718			
80	Y	0.3481	0.3842	0.3361	0.8164	1.8848	0.3505	0.8584	1.8728
	Z	-	0.3361	0.3482	0.9004	1.8608			
100	Y	0.3359	0.3599	0.3599	0.8159	1.8716	0.3599	0.8279	1.8656
	Z	-	0.3960	0.3479	0.8398	1.8596			
250	Y	0.3477	0.3597	0.3357	0.8033	1.8464	0.3453	0.8573	1.8404
	Z	-	0.3357	0.3477	0.9112	1.8344			

Angular Frequency (G r.p.m.)	Axes	(b) Scroll Type B					Average (nm)		
		d_1	d_2	d_3	d_i	d_o	d	d_i'	d_o'
10	Y	-	0.3359	0.3479	0.9238	1.8716	0.3407	0.8758	1.8610
	Z	0.3359	0.3479	0.3360	0.8278	1.8503			
20	Y	-	0.3360	0.3361	0.9360	1.8602	0.3409	0.8820	1.8602
	Z	0.3361	0.3600	0.3361	0.8280	1.8602			
70	Y	-	0.3597	0.3478	0.9354	1.8828	0.3454	0.8815	1.8648
	Z	0.3358	0.3477	0.3358	0.8275	1.8468			
200	Y	-	0.3720	0.3360	0.9360	1.8600	0.3456	0.8760	1.8480
	Z	0.3240	0.3480	0.3480	0.8160	1.8360			
300	Y	-	0.3478	0.3478	0.9115	1.8710	0.3502	0.8576	1.8650
	Z	0.3358	0.3838	0.3358	0.8036	1.8590			
350	Y	-	0.3360	0.3480	0.9240	1.8480	0.3432	0.8700	1.8480
	Z	0.3360	0.3600	0.3360	0.8160	1.8480			

frequency. From **Figure 3.18**, it is apparent that the two types of scrolls formed appear to be mirror images of each other, and the representative concentration profiles in **Figure 3.20** confirm that observation. Thus, the concentration profile for scroll type A along Y-axis (**Figure 3.20**(a)-blue solid line) resembles that for scroll type B along Z-axis (**Figure 3.20**(b)-red dashed line). Nevertheless, all the structures formed are stable configurations since the average interlayer distances (*d*) of each structure is more than 3.4 Å, as shown in **Table 3-6**.

3.5.2. Changing Strength of Applied E-field

In order to study the effect of the E-field strength on the self-assembly of the GNR structure immersed in an aqueous environment under a rotating E-field, we studied the trajectories of GNRs of different dimensions using E-fields of constant angular frequency equal to 30 Gr.p.m. but varying strengths from 0.1 V/nm to 1 V/nm in 0.1 V/nm steps for a simulation time of 10 ns. Our results show that there is a minimum strength of the applied E-field required to cause the GNR to continuously align with it and thus form a nanoscroll. For a GNR structure of dimensions 100.3 Å × 51.9 Å, the minimum E-field strength required for the formation of a nanoscroll structure is found to be 0.2 V/nm at an angular frequency of 30 Gr.p.m. In [130], "**Supporting Movie 5**" shows the trajectories of this GNR under 0.1 V/nm (red) and 0.2 V/nm (cyan) strengths of E-field. At a lower E-field strength than 0.2 V/nm, it is seen from the trajectory of the GNR under study that the field is not strong enough to induce a complete rotational motion in the planar GNR. As a result, the free end of the GNR does not come close enough to its fixed edge to induce any non-bonded vdW interaction within the GNR and thus, no self-assembly is observed. Moreover, the same study conducted for GNRs having the same length but varying width reveals that the minimum E-field strength required to induce self-assembly of a GNR varies with its dimensions. Specifically, the required minimum E-field

strength increases with decreasing width of the GNR. For example, for a GNR measuring 100.3 Å × 17.8 Å the required minimum E-field strength at an angular frequency of 30 G r.p.m. is 0.4 V/nm. The corresponding simulation video for this GNR structure under 0.1 V/nm (red) and 0.4 V/nm (cyan) may be found as "**Supporting Movie 6**" in [130]. For weaker E-fields at this frequency, the trajectory of the GNR shows that it is unable to follow the rotating E-field due to an irregular, "jerky" path.
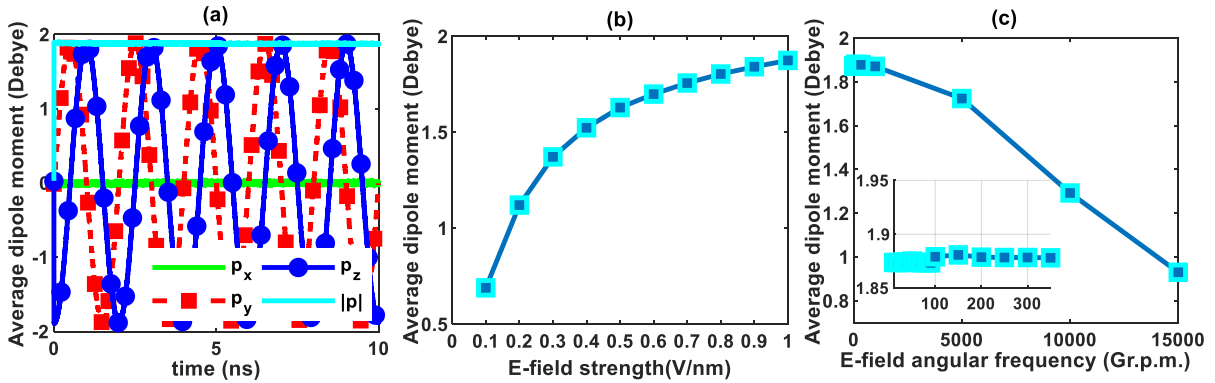
Figure 3.21. Figure showing the variation in the water dipole orientation with the E-field. (a) Variation of the average dipole strength along X, Y, and Z directions for a field strength of 1 V/nm and speed 30 Gr.p.m in the YZ plane. (b) Effect of field strength on the net average water dipole strength at a constant frequency of 30 Gr.p.m. (c) Effect of E-field rotational speed on the net average dipole strength at a constant field strength of 1 V/nm.

To explain the results of our study, we analyzed the orientation of the water dipoles under rotating E-fields of varying angular frequency and strength. **Figure 3.21** (a) shows the variation of the average dipole strength per water molecule in the X, Y and Z directions under a rotating E-field of strength 1 V/nm and 30 Gr.p.m. When a rotating field is applied in the YZ plane, E-field in the Y and Z directions is varied sinusoidally with a 90º phase difference between them. Since, the water dipoles align parallel to the direction of the applied E-field, a similar sinusoidal variation in their orientation along the axes is seen. The norm of the resultant dipole moment vector per water molecule is also shown, which is a measure of the degree of alignment of the water molecules (cyan line). In **Figure 3.21** (b), the variation of

the average dipole moment per water molecule for varying strengths of the E-field at an angular frequency of 30 Gr.p.m. is shown. The experimental value quoted in the literature for the dipole moment of a water monomer is 1.85 D [146, 147], whereas the theoretical value using a TIP3P model is reported to be 2.35 D [148, 149]. It is seen that the average dipole moment per water molecule decreases for weaker E-fields, i.e. the water molecules are less aligned with the direction of the applied E-field. This explains the inability of the GNR structure to follow the rotational motion of the applied E-fields of weaker strengths. The increasing disorientation of the water molecules at weaker strengths of E-field may also explain the need for a higher minimum E-field for a narrower GNR. Since a narrower GNR offers a smaller solvent accessible surface area to the surrounding water molecules it is immersed in, there is less area of contact between the GNR and the water molecules and thus, a higher degree of orientation per water molecule is required to bring about a complete rotation of the GNR. A complete rotation, in turn, is required for the free end of the GNR to come close enough to the fixed end to induce its self-assembly. Since the water dipole moment also varies with the angular frequency, **Figure 3.21** (c) shows the average dipole moment per water molecule at E-fields of different angular frequencies with the same strength (1 V/nm). The water dipoles need a finite amount of time to orient towards the direction of the applied E-field, thus the net average water dipole moment decreases for ultra-fast speeds. For the range of frequencies used in our study, the dipoles can easily follow the rotating field which corresponds to the relatively flat section of **Figure 3.21**(c), which is magnified in its inset. However, at higher frequencies, the water dipoles get less time to respond to the field and therefore, the net average dipole strength decreases.

3.6. Formation of Hybrid-GNS Structure Using the Proposed Setup

GNS formation induced by different nanotemplates such as CNT, nanowires, metal nanoparticles and others triggered the study and use of different hybrid-GNS core/shell structure. Inspired by these studies, we investigated whether our proposed setup can also be utilized to form a core/shell GNS structure. Similar to Xia *et al.* [18], an (8,8) SWCNT of diameter equal to approximately 10 Å and length 99 Å is placed along the fixed edge of a 100.3 Å × 94.5 Å GNR structure. The combined structure is placed in a 12 nm × 12 nm × 14 nm box containing 64296 water molecules and subjected to a rotating E-field of 90 Gr.p.m. angular frequency and 1 V/nm strength. In addition to the prolonged edges of the GNR structure, the carbon atoms at the edge of the SWCNT on either end are also kept fixed in this simulation. The resulting assembly of the GNR around the CNT forms the hybrid core/shell composite shown in **Figure 3.22**(a). It has been shown previously that CNTs larger than 10 Å in diameter are able to induce the self-assembly of a GNR around it [18]. Our studies reveal that when a rotating E-field is applied to such a structure submerged in water, the effect of the E-field prevails the vdW interaction energy between the CNT and the GNR. As a result, the GNR follows the applied E-field and gradually encapsulates the CNT in contrast to an ultra-fast assembly that is seen in the absence of the E-field ("**Supporting Movie 7**" in [130]). In fact, because our proposed set-up utilizes the effect of an applied E-field, we are able to overcome the restriction of a minimum diameter of the CNT that was required in earlier proposed methods. **Figure 3.22**(b) shows the resulting core/shell composite when a (4,4) SWCNT of diameter approximately equal to 5.4 Å and length 99 Å is used instead. The full simulation video of 10 ns is available as "**Supporting Movie M8**" in [130]. Thus, using an applied E-field to induce the self-assembly of a GNR over a SWCNT, we were able to form a

core/shell composite hybrid structure and at the same time, remove the dependence of the formation on the dimension of the nanotemplate. The inner diameter of the composite is determined by the diameter of the SWCNT and thus our proposed method offers more control over the size of the composite structure than the methods proposed previously [18, 81].

(a)

(b)
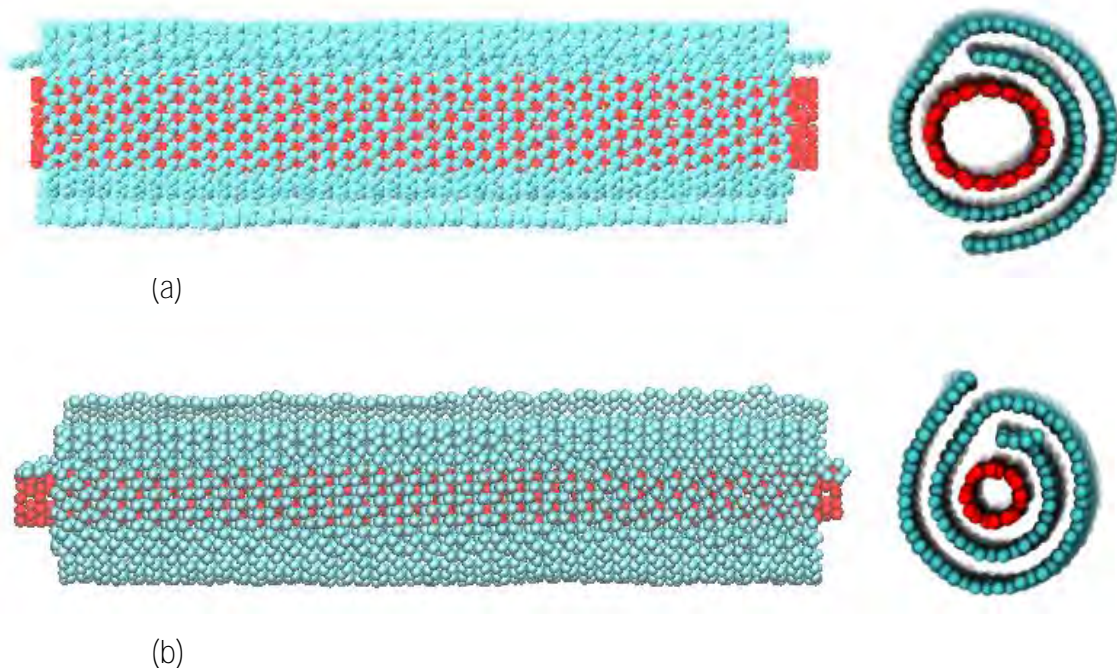
Figure 3.22. Hybrid core/shell composite structures formed using our proposed setup. The GNR used is of zigzag type measuring 100.3 Å x 9.45 Å. The applied E-field has an angular frequency of 90 Gr.p.m. and 1 V/nm strength. Structure formed using (a) (8,8) CNT of diameter approximately 10 Å and (b) (4,4) CNT of diameter approximately 5.4 Å. The CNTs are colored red and the GNR is colored cyan. The figure shows both lateral and front view of the final structure formed after subsequent removal of the applied E-field.
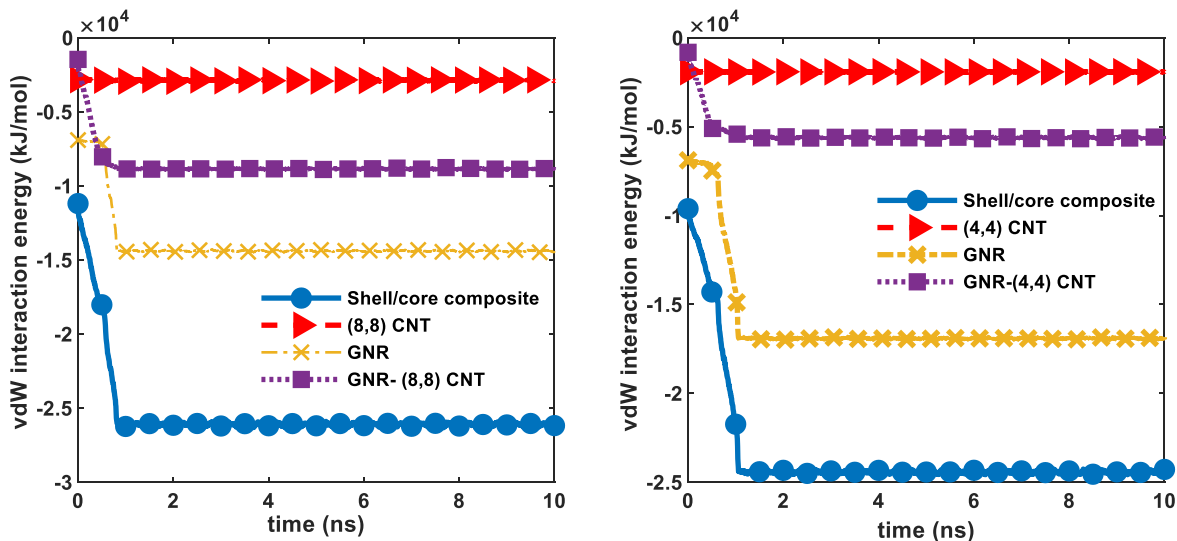
Figure 3.23. Time evolution of the vdW interaction energy of core/shell composite structures formed from (a) (8,8) CNT and (b) (4, 4) CNT using a rotating E-field on a GNR in water. The figure shows the interaction energy profiles of the whole structure (blue solid line with round markers), only the CNT (Red dashed line with triangular markers), only the GNR (orange dash-dotted line with cross markers), and between the GNR and the CNT (violet dotted line with square markers).

The change in the vdW interaction energy of the structure as the GNR encompasses the (8,8) and (4,4) CNTs are shown in **Figure 3.23**(a) and (b) respectively. The red line with triangular markers show the energy interaction profiles for the CNTs which of course remains constant throughout the simulation as the CNT itself does not undergo any structural changes. The orange line with cross markers shows the vdW interaction energy profile for the GNR which shows a sharp fall indicating the self-assembly of the GNR. The blue line with round markers shows the vdW interaction energy profile for the core/shell composite structure and depicts the same sharp fall as in the profile for GNR. On the other hand, we have also calculated the vdW interaction energy between the CNT and the GNR over the course of the simulation (violet line with square markers). As the planar GNR encirculates the fixed CNT, the area of contact increases so that the vdW interaction energy between them increases as well. Finally, in **Figure 3.24**, the average vdW interaction energy per carbon atom of the hybrid composite
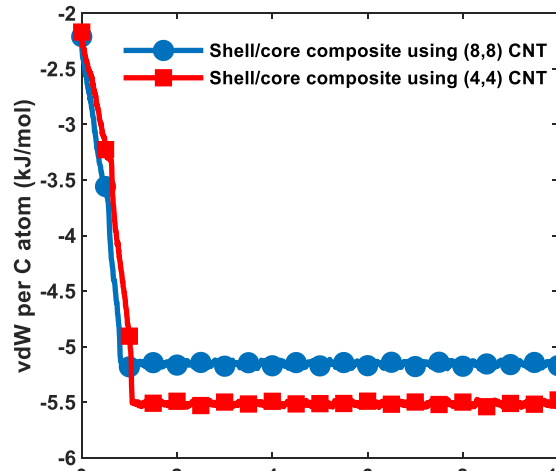
Figure 3.24. Average vdW interaction energy per carbon atom of the core/shell composite structures formed using a (8,8) CNT (Blue line with round markers) and a (4,4) CNT (Red line with square markers).

structures formed from (8,8) and (4,4) CNTs is shown. It is observed that the core/shell composite formed using (4,4) CNT is morphologically more stable than that for (8,8) CNT.

The concentration profiles along the Y and Z direction of the CNTs used to form the composite structures, as well as the GNS encompassing them, are shown in **Figure 3.25**. The distances measured between the adjacent peaks in the concentration profiles, including the peaks in the CNT profiles, in **Figure 3.25**, for the structures shown in **Figure 3.22** are given in **Table 3-7**. Here, d_1 and d_4 are distances measured between adjacents peaks in the concentration profile of the GNS (cyan line with round markers), representing the inter-wall distances between the GNS layers whereas d_2 and d_3 are measured between the inner peaks of the GNS profile and the outer peak of the CNT profile (red dashed line with square markers), thus represents the inter-wall distances between the inner layer of the GNS and the CNT. C_d is the distance between the outermost peaks in the CNT profile and is thus the diameter of the CNT whereas d_o is measured between the outermost peaks of the GNS profile, so is the outer diameter. All

values of d_1-d_4 lie well within that for a strong-adhesive-binding region, so that it is virtually impossible to remove the CNT from the hybrid structure.
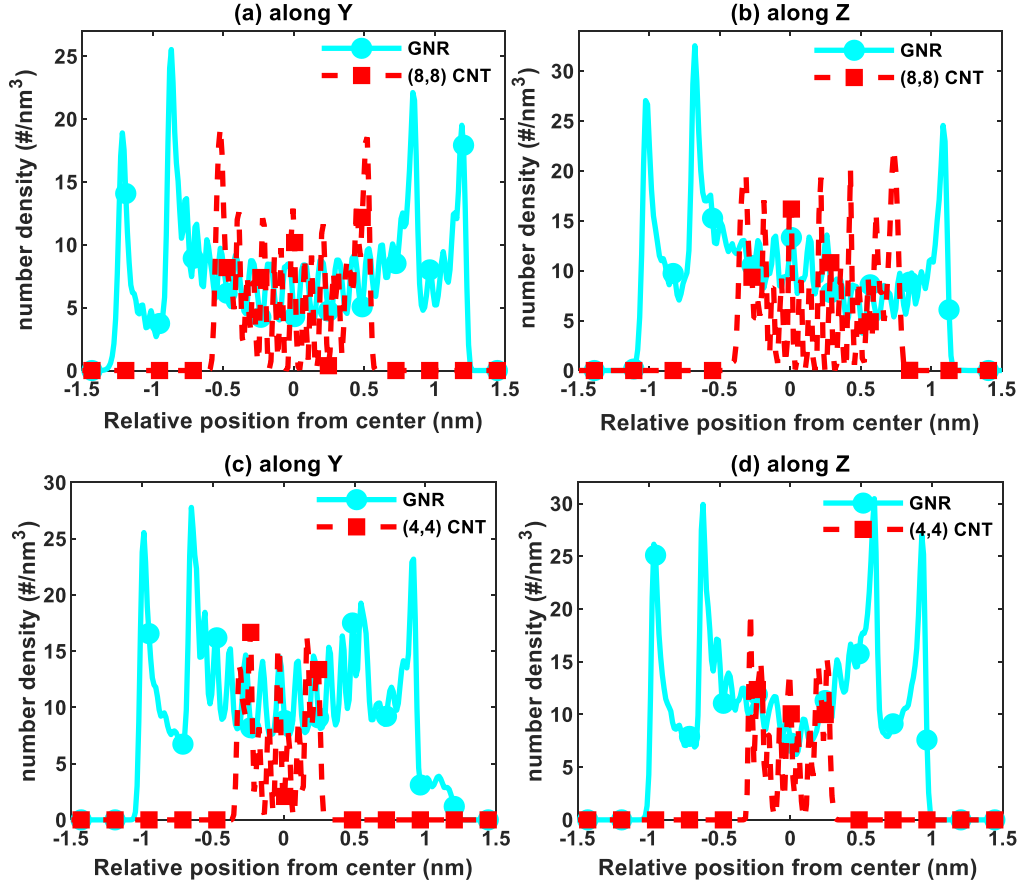
Figure 3.25. Concentration profiles of the core/shell composites formed using (a), (b) (8,8) CNT and (c), (d) (4,4) CNT nano-templates.

Table 3-7 Interlayer distances (d_1, d_2, d_3, d_4), CNT diameter (C_d) and outer (d_o) diameter along with their corresponding averages (d, C_d', and d_o') of the core/shell composites formed using (8,8) and (4,4) SWCNT.

Core/shell formed using	Axes	Distances (nm)						Average (nm)		
		d_1	d_2	d_3	d_4	C_d	d_o	d	C_d'	d_o'
(8,8) CNT	Y	0.3472	0.3476	0.3236	0.3472	1.0424	2.408	0.3469	1.0454	2.2595
	Z	0.3500	0.3635	0.3491	-	1.0484	2.1110			
(4,4) CNT	Y	0.3353	0.3354	0.3114	0.3713	0.5510	1.9044	0.3386	0.5450	1.8984
	Z	0.3474	0.3353	0.3354	0.3357	0.5390	1.8924			

3.7. Formation of Scrolls from Multilayer GNRs

In this section, we will demonstrate the formation of scroll structures from multilayer GNRs using our proposed setup. Double and triple layer zigzag GNRs structures with prolonged edges each measuring 100.3 Å × 94.5 Å were placed parallel to the XZ plane separately in a 12 nm × 12 nm × 12 nm cubic box containing 54058 water molecules. Each structure was subjected to rotating E-fields of 90 Gr.p.m. angular frequency and 1 V/nm strength for 10 ns. After 10 ns, the E-field was turned off and the resulting structures formed are shown in **Figure 3.26**. As seen in the figure, the bilayer and trilayer GNRs form inter-twined structures with well-defined scroll morphology. The full simulation videos for the bilayer and trilayer GNR structure under an E-field can be found as "**Supporting Movie 9**" and "**Supporting Movie 10**" in [130].

(a)   (b)
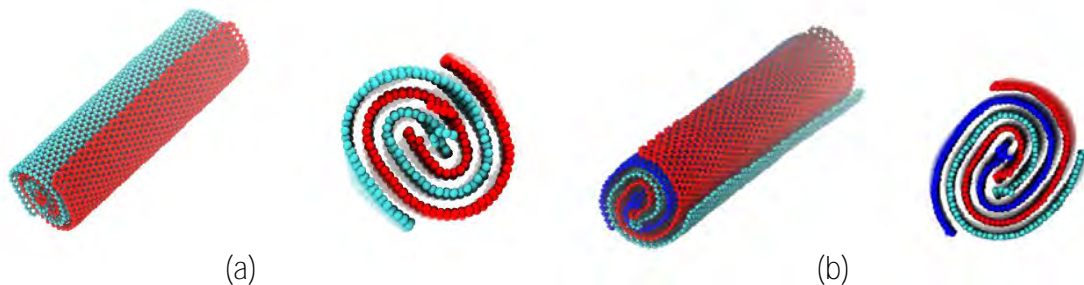
Figure 3.26. Scroll formation from (a) bilayer, and (b) trilayer GNR structures using our proposed setup. (Cyan-GNS_1, Red-GNS_2, Blue-GNS_3)

The change in the vdW interaction energy profiles for the self-assembly of a bilayer and trilayer GNRs under a rotating E-field are shown in **Figure 3.27** and **Figure 3.28**. As the multilayer GNRs inter-twin into a scroll morphology, there is a sharp fall in the vdW interaction energy of the structure. In addition, the vdW interaction energy between the different layers of the GNRs is also shown in the figures. It is observed that there is a sharp fall in the interaction energy between the two layers of the bilayer GNR. (**Figure 3.27**(b)). In case of the trilayer GNR, a sharp fall in the interaction energy between GNR_1 and GNR_3 is observed while the interaction energies between the other sets of layers remain fairly constant. Nevertheless, all interaction energies converge to a comparable value.
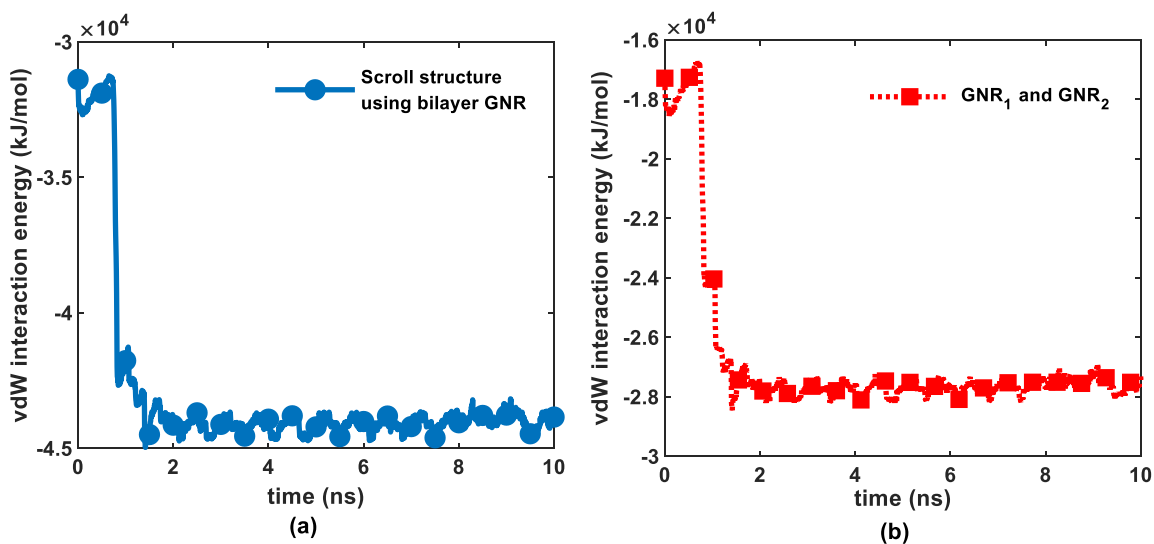
Figure 3.27. Time evolution of the vdW interaction energy (a) of the bilayer GNR as it assembles into a scroll and (b) between GNR_1 and GNR_2.
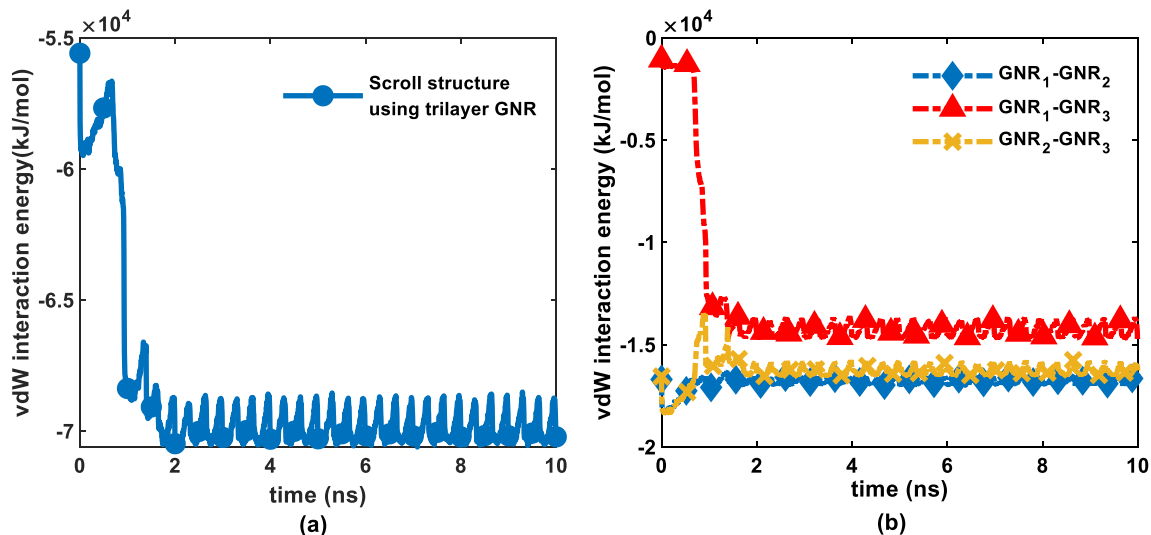
Figure 3.28. Time evolution of the vdW interaction energy (a) of the trilayer GNR as it assembles into a scroll and (b) between GNR_1 and GNR_2 (blue triangular markers), GNR_1 and GNR_3 (red line with triangular markers), and GNR_2 and GNR_3 (orange line with cross markers).

The concentration profiles of each GNR layer in each structure is calculated along the Y and Z direction. (**Figure 3.29**) The measured distances between the adjacent peaks representing the interlayer distances and the outer diameter of the scroll structure are shown in **Table 3-8**. The average interlayer distances (d) of the scroll structures are 3.571 and 3.418 Å respectively in the case of bilayer and trilayer GNR. The sharp fall in the vdW interaction energy profiles paired with the distances measured from the concentration validate the stability of the final scroll structures.
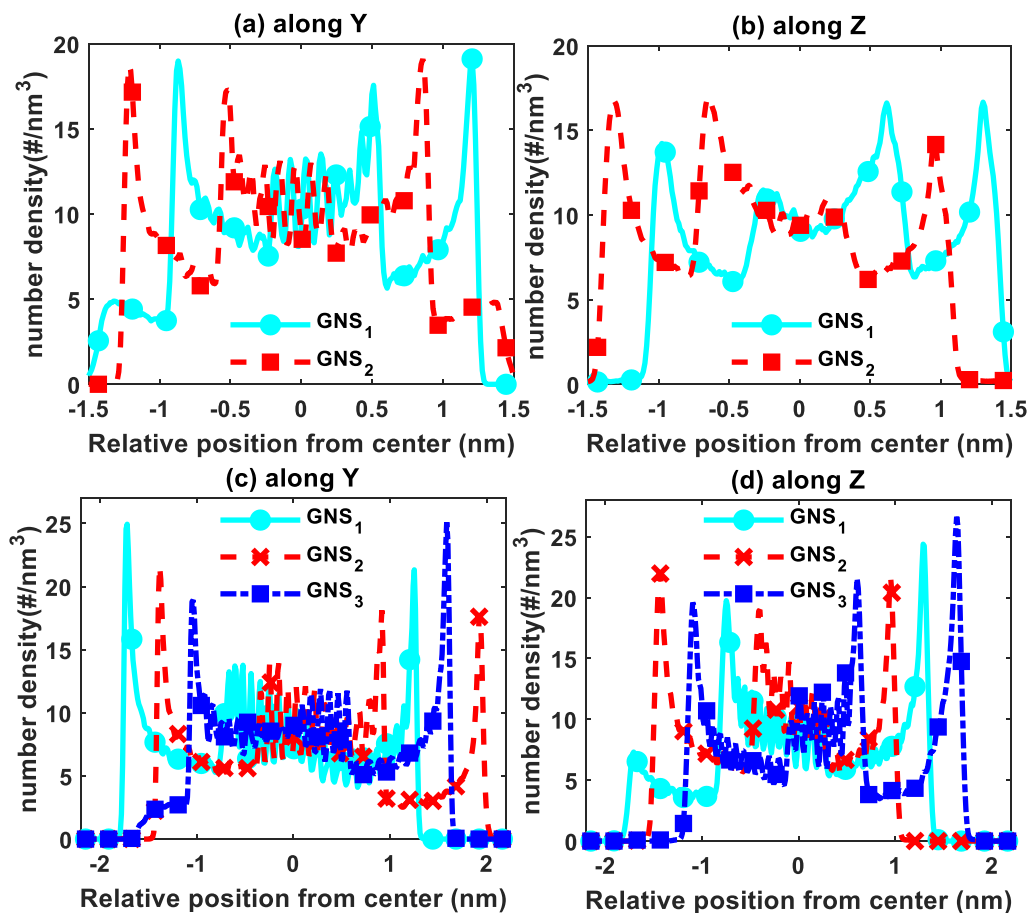
Figure 3.29. Concentration profiles of the scrolls formed from (a), (b) Bilayer and (c), (d) Trilayer GNRs

Table 3-8 Interlayer distances (d_1, d_2, d_3, d_4, d_5, and d_6), and outer (d_o) diameter along with their corresponding averages (d and d_o') of the scrolls formed from bilayer and trilayer GNRs.

Type of GNR	Direction	Distance (nm)							Average (nm)	
		d_1	d_2	d_3	d_4	d_5	d_6	d_o	d	d_o'
Bilayer	Y	-	0.3475	0.3474	0.3475	0.3474	-	2.648	0.3571	2.636
	Z	0.3476	0.3355	0.3833	0.4313	0.3354	0.3476	2.624		
Trilayer	Y	0.3350	0.3470	0.3351	0.3350	0.3480	-	3.652	0.3418	3.496
	Z	0.3350	0.3477	0.3472	0.3472	0.3352	0.3470	3.340		

Conclusion and Future Works

4.1. Conclusion

In conclusion, we have used MD simulation to study the E-field induced orientation of a suspended GNR structure submerged in water to facilitate its assembly into a GNS with hollow core and homogeneous morphology. The stability and uniformity of the final scrolls formed have been illustrated with the aid of vdW interaction energy profiles and concentration profiles along the scrolling directions. The versatility of the method has been established by depicting scroll formation from GNR structures varying in length, width, and chirality, thus relinquishing higher degree of control over the final structure obtained. We have shown the effect of changing E-field properties such as its angular frequency and strength on the trajectory of the GNR and the corresponding GNSs formed, thus establishing the relative independence of the proposed technique on the process conditions. Moreover, it has been shown that the proposed setup overcomes the limitation of a critical dimension of the nanotemplate when utilized to form a core/shell composite structure. Our proposed work thus offers a simple electrical energy activated, purely physical, energy-inexpensive method towards the fabrication of a pure GNS from a nanoribbon at room temperature. Such a method would pave the way for the realization of high quality GNS from graphene nanoribbon utilizing E-field induced orientation of hydrated nanoparticles, facilitating exciting new avenues of fundamental and applied research on nanoscrolls.

4.2. Future works

An obvious task would be to realize the proposed work using an experimental setup to form a nanoscroll structure from a GNR of desired dimensions and chirality. While that may be

outside the current scope of our research group, many interesting theoretical works can be explored as an extension of this thesis work. In addition to graphene-based nanoscroll, the suitability of the proposed work for other 2-D material such as transition metal dichalcogenides as well as popular nanoscroll materials such as graphene oxide can be studied using MD simulations. Furthermore, it would be useful to calculate the electronic and opto-electronic properties of the GNS formed in this work using first principles simulations. In addition to these, MD simulations can be used to conduct some application-oriented studies using the GNS formed using our proposed method, such as its performance in hydrogen storage, water/ion conduction channels or nanoelectromechanical actuators.

References

[1]   Gogotsi, Y. and Presser, V., Eds., *Carbon Nanomaterials*, 2nd ed. Boca Raton: CRC press, 2013.

[2]   Bacon, R., "Growth, Structure, and Properties of Graphite Whiskers," *Journal of Applied Physics,* vol. 31, pp. 283-290, 1960.

[3]   Zhang, Z., Zhao, J., Zhou, J., Zhao, Y., Tang, X., and Zhuo, S., "Interfacial engineering of metal oxide/graphene nanoscrolls with remarkable performance for lithium ion batteries," *Energy Storage Materials,* vol. 8, pp. 35-41, 2017.

[4]   Tarábková, H., Zelinger, Z., and Janda, P., "Electrochemically controlled winding and unwinding of substrate-supported carbon nanoscrolls," *Physical Chemistry Chemical Physics,* vol. 20, pp. 5900-5908, 2018.

[5]   Shi, X., Cheng, Y., Pugno, N. M., and Gao, H., "Tunable Water Channels with Carbon Nanoscrolls," *Small,* vol. 6, pp. 739-744, 2010.

[6]   Berman, D., Deshmukh, S. A., Sankaranarayanan, S. K. R. S., Erdemir, A., and Sumant, A. V., "Macroscale superlubricity enabled by graphene nanoscroll formation," *Science,* vol. 348, pp. 1118-1122, 2015.

[7]   Liu, Z., Wang, J., Ding, H., Chen, S., Yu, X., and Lu, B., "Carbon Nanoscrolls for Aluminum Battery," *ACS Nano,* vol. 12, pp. 8456-8466, 2018.

[8]   Braga, S. F., Coluci, V. R., Legoas, S. B., Giro, R., Galvão, D. S., and Baughman, R. H., "Structure and Dynamics of Carbon Nanoscrolls," *Nano Letters,* vol. 4, pp. 881-884, 2004.

[9]   Chen, Y., Lu, J., and Gao, Z., "Structural and Electronic Study of Nanoscrolls Rolled up by a Single Graphene Sheet," *The Journal of Physical Chemistry C,* vol. 111, pp. 1625-1630, 2007.

[10]   Pan, H., Feng, Y., and Lin, J., "Ab initio study of electronic and optical properties of multiwall carbon nanotube structures made up of a single rolled-up graphite sheet," *Physical Review B,* vol. 72, 085415, 2005.

[11] Chang, C.-H. and Ortix, C., "Theoretical Prediction of a Giant Anisotropic Magnetoresistance in Carbon Nanoscrolls," *Nano Letters,* vol. 17, pp. 3076-3080, 2017.

[12] Bejagam, K. K., Singh, S., and Deshmukh, S. A., "Nanoparticle activated and directed assembly of graphene into a nanoscroll," *Carbon,* vol. 134, pp. 43-52, 2018.

[13] Dhar, P., Gaur, S. S., Kumar, A., and Katiyar, V., "Cellulose Nanocrystal Templated Graphene Nanoscrolls for High Performance Supercapacitors and Hydrogen Storage: An Experimental and Molecular Simulation Study," *Scientific Reports,* vol. 8, 3886, 2018.

[14] Schmidt, M. E., Hammam, A. M. M., Iwasaki, T., Kanzaki, T., Muruganathan, M., Ogawa, S.*, et al.*, "Controlled fabrication of electrically contacted carbon nanoscrolls," *Nanotechnology,* vol. 29, 235605, 2018.

[15] Li, J. L., Peng, Q. S., Bai, G. Z., and Jiang, W., "Carbon scrolls produced by high energy ball milling of graphite," *Carbon,* vol. 43, pp. 2830-2833, 2005.

[16] Shioyama, H. and Akita, T., "A new route to carbon nanotubes," *Carbon,* vol. 41, pp. 179-181, 2003.

[17] Xie, X., Ju, L., Feng, X., Sun, Y., Zhou, R., Liu, K.*, et al.*, "Controlled Fabrication of High-Quality Carbon Nanoscrolls from Monolayer Graphene," *Nano Letters,* vol. 9, pp. 2565-2570, 2009.

[18] Xia, D., Xue, Q., Xie, J., Chen, H., Lv, C., Besenbacher, F.*, et al.*, "Fabrication of Carbon Nanoscrolls from Monolayer Graphene," *Small,* vol. 6, pp. 2010-2019, 2010.

[19] Sharifi, T., Gracia-Espino, E., Reza Barzegar, H., Jia, X., Nitze, F., Hu, G.*, et al.*, "Formation of nitrogen-doped graphene nanoscrolls by adsorption of magnetic γ-Fe2O3 nanoparticles," *Nature Communications,* vol. 4, 2319, 2013.

[20] Daub, C. D., Bratko, D., Ali, T., and Luzar, A., "Microscopic Dynamics of the Orientation of a Hydrated Nanoparticle in an Electric Field," *Physical Review Letters,* vol. 103, 207801, 2009.

[21] Rahman, M. M., Chowdhury, M. M., and Alam, M. K., "Rotating-Electric-Field-Induced Carbon-Nanotube-Based Nanomotor in Water: A Molecular Dynamics Study," *Small,* vol. 13, 1603978, 2017.

[22] Kroto, H. W., Heath, J. R., O'Brien, S. C., Curl, R. F., and Smalley, R. E., "C60: Buckminsterfullerene," *Nature,* vol. 318, pp. 162-163, 1985.

[23] Iijima, S., "Helical microtubules of graphitic carbon," *Nature,* vol. 354, pp. 56-58, 1991.

[24] Anantram, M. P. and Léonard, F., "Physics of carbon nanotube electronic devices," *Reports on Progress in Physics,* vol. 69, pp. 507-561, 2006.

[25] Yao, Z., Kane, C. L., and Dekker, C., "High-Field Electrical Transport in Single-Wall Carbon Nanotubes," *Physical Review Letters,* vol. 84, pp. 2941-2944, 2000.

[26] Kong, J., Yenilmez, E., Tombler, T. W., Kim, W., Dai, H., Laughlin, R. B*., et al.*, "Quantum Interference and Ballistic Transmission in Nanotube Electron Waveguides," *Physical Review Letters,* vol. 87, 106801, 2001.

[27] Kim, P., Shi, L., Majumdar, A., and McEuen, P. L., "Thermal Transport Measurements of Individual Multiwalled Nanotubes," *Physical Review Letters,* vol. 87, 215502, 2001.

[28] Pop, E., Mann, D., Wang, Q., Goodson, K., and Dai, H., "Thermal Conductance of an Individual Single-Wall Carbon Nanotube above Room Temperature," *Nano Letters,* vol. 6, pp. 96-100, 2006.

[29] Jiménez Soto, J. M. and Aranzana, M. S. C., "Conical Carbon Nanoparticles in Analytical Chemistry," in *Encyclopedia of Analytical Chemistry*, Meyers, R. A., Ed., ed: John Wiley & Sons, Ltd., 2012.

[30] Dresselhaus, M. S., Dresselhaus, G., and Saito, R., "Physics of carbon nanotubes," *Carbon,* vol. 33, pp. 883-891, 1995.

[31] Novoselov, K. S., Geim, A. K., Morozov, S. V., Jiang, D., Zhang, Y., Dubonos, S. V*., et al.*, "Electric Field Effect in Atomically Thin Carbon Films," *Science,* vol. 306, pp. 666-669, 2004.

[32] Bolotin, K. I., Sikes, K. J., Jiang, Z., Klima, M., Fudenberg, G., Hone, J*., et al.*, "Ultrahigh electron mobility in suspended graphene," *Solid State Communications,* vol. 146, pp. 351-355, 2008.

[33] Efetov, D. K. and Kim, P., "Controlling Electron-Phonon Interactions in Graphene at Ultrahigh Carrier Densities," *Physical Review Letters,* vol. 105, 256805, 2010.

[34] Ci, L., Song, L., Jariwala, D., ElÃas, A. L., Gao, W., Terrones, M*., et al.*, "Graphene Shape Control by Multistage Cutting and Transfer," *Advanced Materials,* vol. 21, pp. 4487-4491, 2009.

[35] Parashar, U. K., Bhandari, S., Srivastava, R. K., Jariwala, D., and Srivastava, A., "Single step synthesis of graphene nanoribbons by catalyst particle size dependent cutting of multiwalled carbon nanotubes," *Nanoscale,* vol. 3, pp. 3876-3882, 2011.

[36] Han, M. Y., Özyilmaz, B., Zhang, Y., and Kim, P., "Energy Band-Gap Engineering of Graphene Nanoribbons," *Physical Review Letters,* vol. 98, 206805, 2007.

[37] Jiao, L., Zhang, L., Wang, X., Diankov, G., and Dai, H., "Narrow graphene nanoribbons from carbon nanotubes," *Nature,* vol. 458, pp. 877-880, 2009.

[38] Kosynkin, D. V., Higginbotham, A. L., Sinitskii, A., Lomeda, J. R., Dimiev, A., Price, B. K*., et al.*, "Longitudinal unzipping of carbon nanotubes to form graphene nanoribbons," *Nature,* vol. 458, pp. 872-876, 2009.

[39] Abergel, D. S. L., Apalkov, V., Berashevich, J., Ziegler, K., and Chakraborty, T., "Properties of graphene: a theoretical perspective," *Advances in Physics,* vol. 59, pp. 261-482, 2010.

[40] Shi, X., Pugno, N. M., and Gao, H., "Tunable Core Size of Carbon Nanoscrolls," *Journal of Computational and Theoretical Nanoscience,* vol. 7, pp. 517-521, 2010.

[41] Mpourmpakis, G., Tylianakis, E., and Froudakis, G. E., "Carbon Nanoscrolls: A Promising Material for Hydrogen Storage," *Nano Letters,* vol. 7, pp. 1893-1897, 2007.

[42] Coluci, V. R., Braga, S. F., Baughman, R. H., and Galvão, D. S., "Prediction of the hydrogen storage capacity of carbon nanoscrolls," *Physical Review B,* vol. 75, 125404, 2007.

[43]   Zaeri, M. M. and Ziaei-Rad, S., "Elastic properties of carbon nanoscrolls," *RSC Adv.,* vol. 4, pp. 22995-23001, 2014.

[44]   Perim, E., Machado, L. D., and Galvao, D. S., "A Brief Review on Syntheses, Structures, and Applications of Nanoscrolls," *Frontiers in Materials,* vol. 1, 31, 2014.

[45]   Braga, S. F., Coluci, V. R., Baughman, R. H., and Galvão, D. S., "Hydrogen storage in carbon nanoscrolls: An atomistic molecular dynamics study," *Chemical Physics Letters,* vol. 441, pp. 78-82, 2007.

[46]   Hummer, G., Rasaiah, J. C., and Noworyta, J. P., "Water conduction through the hydrophobic channel of a carbon nanotube," *Nature,* vol. 414, pp. 188-190, 2001.

[47]   Zhu, F. and Schulten, K., "Water and Proton Conduction through Carbon Nanotubes as Models for Biological Channels," *Biophysical Journal,* vol. 85, pp. 236-244, 2003.

[48]   Li, J., Gong, X., Lu, H., Li, D., Fang, H., and Zhou, R., "Electrostatic gating of a nanometer water channel," *Proceedings of the National Academy of Sciences,* vol. 104, pp. 3687-3692, 2007.

[49]   Rurali, R., Coluci, V. R., and Galvão, D. S., "Prediction of giant electroactuation for papyruslike carbon nanoscroll structures: First-principles calculations," *Physical Review B,* vol. 74, 085414, 2006.

[50]   Shi, X., Cheng, Y., Pugno, N. M., and Gao, H., "A translational nanoactuator based on carbon nanoscrolls on substrates," *Applied Physics Letters,* vol. 96, 053115, 2010.

[51]   Feng, K., Tang, B., and Wu, P., ""Evaporating" Graphene Oxide Sheets (GOSs) for Rolled up GOSs and Its Applications in Proton Exchange Membrane Fuel Cell," *ACS Applied Materials & Interfaces,* vol. 5, pp. 1481-1488, 2013.

[52]   Li, T. S., Lin, M. F., Huang, Y. C., and Lin, T. C., "Quantum transport in carbon nanoscrolls," *Physics Letters A,* vol. 376, pp. 515-520, 2012.

[53]   Zheng, B., Xu, Z., and Gao, C., "Mass production of graphene nanoscrolls and their application in high rate performance supercapacitors," *Nanoscale,* vol. 8, pp. 1413-1420, 2016.

[54] Yan, M., Wang, F., Han, C., Ma, X., Xu, X., An, Q., *et al.*, "Nanowire Templated Semihollow Bicontinuous Graphene Scrolls: Designed Construction, Mechanism, and Enhanced Energy Storage Performance," *Journal of the American Chemical Society,* vol. 135, pp. 18176-18182, 2013.

[55] Zeng, F., Kuang, Y., Wang, Y., Huang, Z., Fu, C., and Zhou, H., "Facile Preparation of High-Quality Graphene Scrolls from Graphite Oxide by a Microexplosion Method," *Advanced Materials,* vol. 23, pp. 4929-4932, 2011.

[56] Zeng, F., Kuang, Y., Liu, G., Liu, R., Huang, Z., Fu, C., *et al.*, "Supercapacitors based on high-quality graphene scrolls," *Nanoscale,* vol. 4, pp. 3997-4001, 2012.

[57] Fan, T., Zeng, W., Niu, Q., Tong, S., Cai, K., Liu, Y., *et al.*, "Fabrication of high-quality graphene oxide nanoscrolls and application in supercapacitor," *Nanoscale Research Letters,* vol. 10, 192, 2015.

[58] Zhou, W., Liu, J., Chen, T., Tan, K. S., Jia, X., Luo, Z., *et al.*, "Fabrication of Co3O4-reduced graphene oxide scrolls for high-performance supercapacitor electrodes," *Physical Chemistry Chemical Physics,* vol. 13, 14462, 2011.

[59] Zhang, X. F., Zhang, X. B., Van Tendeloo, G., Amelinckx, S., Op de Beeck, M., and Van Landuyt, J., "Carbon nano-tubes; their formation process and observation by electron microscopy," *Journal of Crystal Growth,* vol. 130, pp. 368-382, 1993.

[60] Tojo, T., Fujisawa, K., Muramatsu, H., Hayashi, T., Kim, Y. A., Endo, M., *et al.*, "Controlled interlayer spacing of scrolled reduced graphene nanotubes by thermal annealing," *RSC Advances,* vol. 3, pp. 4161-4166, 2013.

[61] Zhao, J., Yang, B., Zheng, Z., Yang, J., Yang, Z., Zhang, P., *et al.*, "Facile Preparation of One-Dimensional Wrapping Structure: Graphene Nanoscroll-Wrapped of Fe3O4 Nanoparticles and Its Application for Lithium-Ion Battery," *ACS Applied Materials & Interfaces,* vol. 6, pp. 9890-9896, 2014.

[62] Wang, Y. and Zhang, Y., "Superior thermal conductivity of carbon nanoscroll based thermal interface materials," *2015 IEEE 65th Electronic Components and Technology Conference (ECTC)*, San Diego, CA, 2015, pp. 1234-1239.

[63] Krätschmer, W., Lamb, L. D., Fostiropoulos, K., and Huffman, D. R., "Solid C60: a new form of carbon," *Nature,* vol. 347, pp. 354-358, 1990.

[64] Ugarte, D., "Morphology and structure of graphitic soot particles generated in arc-discharge C60 production," *Chemical Physics Letters,* vol. 198, pp. 596-602, 1992.

[65] Saito, Y., Yoshikawa, T., Inagaki, M., Tomita, M., and Hayashi, T., "Growth and structure of graphitic tubules and polyhedral particles in arc-discharge," *Chemical Physics Letters,* vol. 204, pp. 277-282, 1993.

[66] Amelinckx, S., Bernaerts, D., Zhang, X. B., Van Tendeloo, G., and Van Landuyt, J., "A Structure Model and Growth Mechanism for Multishell Carbon Nanotubes," *Science,* vol. 267, pp. 1334-1338, 1995.

[67] Viculis, L. M., Mack, J. J., and Kaner, R. B., "A Chemical Route to Carbon Nanoscrolls," *Science,* vol. 299, pp. 1361-1361, 2003.

[68] Roy, D., Angeles-Tactay, E., Brown, R. J. C., Spencer, S. J., Fry, T., Dunton, T. A*., et al.*, "Synthesis and Raman spectroscopic characterisation of carbon nanoscrolls," *Chemical Physics Letters,* vol. 465, pp. 254-257, 2008.

[69] Savoskin, M. V., Mochalin, V. N., Yaroshenko, A. P., Lazareva, N. I., Konstantinova, T. E., Barsukov, I. V*., et al.*, "Carbon nanoscrolls produced from acceptor-type graphite intercalation compounds," *Carbon,* vol. 45, pp. 2797-2800, 2007.

[70] Yu, D. and Liu, F., "Synthesis of Carbon Nanotubes by Rolling up Patterned Graphene Nanoribbons Using Selective Atomic Adsorption," *Nano Letters,* vol. 7, pp. 3046-3050, 2007.

[71] Sidorov, A., Mudd, D., Sumanasekera, G., Ouseph, P. J., Jayanthi, C. S., and Wu, S.-Y., "Electrostatic deposition of graphene in a gaseous environment: a deterministic route for synthesizing rolled graphenes?," *Nanotechnology,* vol. 20, 055611, 2009.

[72] Zheng, J., Liu, H., Wu, B., Guo, Y., Wu, T., Yu, G*., et al.*, "Production of High-Quality Carbon Nanoscrolls with Microwave Spark Assistance in Liquid Nitrogen," *Advanced Materials,* vol. 23, pp. 2460-2463, 2011.

[73] Gao, Y., Chen, X., Xu, H., Zou, Y., Gu, R., Xu, M*., et al.*, "Highly-efficient fabrication of nanoscrolls from functionalized graphene oxide by Langmuir–Blodgett method," *Carbon,* vol. 48, pp. 4475-4482, 2010.

[74] Zhao, J., Yang, B., Yang, Z., Zhang, P., Zheng, Z., Ren, W*., et al.*, "Facile preparation of large-scale graphene nanoscrolls from graphene oxide sheets by cold quenching in liquid nitrogen," *Carbon,* vol. 79, pp. 470-477, 2014.

[75] Xu, Z., Zheng, B., Chen, J., and Gao, C., "Highly Efficient Synthesis of Neat Graphene Nanoscrolls from Graphene Oxide by Well-Controlled Lyophilization," *Chemistry of Materials,* vol. 26, pp. 6811-6818, 2014.

[76] Chen, X., Li, L., Sun, X., Kia, H. G., and Peng, H., "A novel synthesis of graphene nanoscrolls with tunable dimension at a large scale," *Nanotechnology,* vol. 23, 055603, 2012.

[77] Cheng, G., Calizo, I., Liang, X., Sperling, B. A., Johnston-Peck, A. C., Li, W*., et al.*, "Carbon scrolls from chemical vapor deposition grown graphene," *Carbon,* vol. 76, pp. 257-265, 2014.

[78] Li, H., Papadakis, R., Jafri, S. H. M., Thersleff, T., Michler, J., Ottosson, H*., et al.*, "Superior adhesion of graphene nanoscrolls," *Communications Physics,* vol. 1, 44, 2018.

[79] Patra, N., Wang, B., and Král, P., "Nanodroplet Activated and Guided Folding of Graphene Nanostructures," *Nano Letters,* vol. 9, pp. 3766-3771, 2009.

[80] Zhang, Z. and Li, T., "Carbon nanotube initiated formation of carbon nanoscrolls," *Applied Physics Letters,* vol. 97, 081909, 2010.

[81] Xia, D., Xue, Q., Xie, J., Chen, H., and Lv, C., "Silicon/graphene core/shell nanowires produced by self-scrolling," *Computational Materials Science,* vol. 49, pp. 588-592, 2010.

[82] Patra, N., Song, Y., and Král, P., "Self-Assembly of Graphene Nanostructures on Nanotubes," *ACS Nano,* vol. 5, pp. 1798-1804, 2011.

[83] Chu, L., Xue, Q., Zhang, T., and Ling, C., "Fabrication of Carbon Nanoscrolls from Monolayer Graphene Controlled by P-Doped Silicon Nanowires: A MD Simulation Study," *The Journal of Physical Chemistry C,* vol. 115, pp. 15217-15224, 2011.

[84] Perim, E., Paupitz, R., and Galvão, D. S., "Controlled route to the fabrication of carbon and boron nitride nanoscrolls: A molecular dynamics investigation," *Journal of Applied Physics,* vol. 113, 054306, 2013.

[85] Wang, Y., Zhan, H. F., Yang, C., Xiang, Y., and Zhang, Y. Y., "Formation of carbon nanoscrolls from graphene nanoribbons: A molecular dynamics study," *Computational Materials Science,* vol. 96, pp. 300-305, 2015.

[86] Xu, S., Fu, H., Li, Y., Zhang, C., Gu, Z., and Zhang, D., "Novel scroll peapod produced by spontaneous scrolling of graphene onto fullerene string," *Physical Chemistry Chemical Physics,* vol. 18, pp. 10138-10143, 2016.

[87] Kim, Y.-K. and Min, D.-H., "Preparation of scrolled graphene oxides with multi-walled carbon nanotube templates," *Carbon,* vol. 48, pp. 4283-4288, 2010.

[88] Li, X., Zhang, Y., Li, T., Zhong, Q., Li, H., and Huang, J., "Graphene nanoscrolls encapsulated TiO2 (B) nanowires for lithium storage," *Journal of Power Sources,* vol. 268, pp. 372-378, 2014.

[89] Wang, X., Yang, D.-P., Huang, G., Huang, P., Shen, G., Guo, S.*, et al.*, "Rolling up graphene oxide sheets into micro/nanoscrolls by nanoparticle aggregation," *Journal of Materials Chemistry,* vol. 22, pp. 17441-17444, 2012.

[90] Richard E. Wilde, S. S., *Statistical Mechanics: Fundamentals and Modern Applications*. New York: John Wiley & Sons, Inc, 1997.

[91] LeSar, R., *Introduction to computational materials science: fundamentals to applications*. New York: Cambridge University Press, 2013.

[92] Alder, B. J. and Wainwright, T. E., "Studies in Molecular Dynamics. I. General Method," *The Journal of Chemical Physics,* vol. 31, pp. 459-466, 1959.

[93] Alder, B. J. and Wainwright, T. E., "Phase Transition for a Hard Sphere System," *The Journal of Chemical Physics,* vol. 27, pp. 1208-1209, 1957.

[94]   Rahman, A., "Correlations in the Motion of Atoms in Liquid Argon," *Physical Review,* vol. 136, pp. A405-A411, 1964.

[95]   Stillinger, F. H. and Rahman, A., "Improved simulation of liquid water by molecular dynamics," *The Journal of Chemical Physics,* vol. 60, pp. 1545-1557, 1974.

[96]   Gates, T., Odegard, G., Frankland, S., and Clancy, T., "Computational materials: Multi-scale modeling and simulation of nanostructured materials," *Composites Science and Technology,* vol. 65, pp. 2416-2434, 2005.

[97]   Shi, X., Pugno, N. M., Cheng, Y., and Gao, H., "Gigahertz breathing oscillators based on carbon nanoscrolls," *Applied Physics Letters,* vol. 95, 163113, 2009.

[98]   Jorgensen, W. L., Maxwell, D. S., and Tirado-Rives, J., "Development and Testing of the OPLS All-Atom Force Field on Conformational Energetics and Properties of Organic Liquids," *Journal of the American Chemical Society,* vol. 118, pp. 11225-11236, 1996.

[99]   Jorgensen, W. L. and Tirado-Rives, J., "The OPLS [optimized potentials for liquid simulations] potential functions for proteins, energy minimizations for crystals of cyclic peptides and crambin," *Journal of the American Chemical Society,* vol. 110, pp. 1657-1666, 1988.

[100] Hockney, R. W., Goel, S. P., and Eastwood, J. W., "Quiet High-Resolution Computer Models of a Plasma," *J. Comp. Phys.,* vol. 14, pp. 148–158, 1974.

[101] Abraham, M. J., Murtolad, T., Schulz, R., Páll, S., Smith , J. C., Hessa, B*., et al.*, "GROMACS: High performance molecular simulations through multi-level parallelism from laptops to supercomputers," *SoftwareX,* vol. 1-2, pp. 19-25, 2015.

[102] Ewald, P. P., "Die Berechnung optischer und elektrostatischer Gitterpotentiale," *Annalen der Physik,* vol. 369, pp. 253-287, 1921.

[103] Darden, T., York, D., and Pedersen, L., "Particle mesh Ewald: An N·log(N) method for Ewald sums in large systems," *The Journal of Chemical Physics,* vol. 98, pp. 10089-10092, 1993.

[104] R.W Hockney, J. W. E., *Computer simulation using particles*. New York: McGraw-Hill, 1981.

[105] Özen, A., Haliloğlu, T., and Schiffer, C. A., "Dynamics of Preferential Substrate Recognition in HIV-1 Protease: Redefining the Substrate Envelope," *Journal of Molecular Biology,* vol. 410, pp. 726-744, 2011.

[106] Berendsen, H. J. C., Postma, J. P. M., van Gunsteren, W. F., DiNola, A., and Haak, J. R., "Molecular dynamics with coupling to an external bath," *J. Chem. Phys.,* vol. 81, pp. 3684–3690, 1984.

[107] Andersen, H. C., "Molecular dynamics simulations at constant pressure and/or temperature," *The Journal of Chemical Physics,* vol. 72, pp. 2384-2393, 1980.

[108] Nose´, S., "A molecular dynamics method for simulations in the canonical ensemble," *Mol. Phys. ,* vol. 52, pp. 255–268, 1984.

[109] Hoover, W. G., "Canonical dynamics: equilibrium phase-space distributions," *Phys. Rev. A,* vol. 31, pp. 1695–1697, 1985.

[110] Bussi, G., Donadio, D., and Parrinello, M., "Canonical sampling through velocity rescaling," *The Journal of Chemical Physics,* vol. 126, p. 014101, 2007.

[111] Parrinello, M. and Rahman, A., "Polymorphic transitions in single crystals: A new molecular dynamics method," *Journal of Applied Physics,* vol. 52, pp. 7182-7190, 1981.

[112] Nosé, S. and Klein, M. L., "Constant pressure molecular dynamics for molecular systems," *Molecular Physics,* vol. 50, pp. 1055-1076, 2006.

[113] Martyna, G. J., Tuckerman, M. E., Tobias, D. J., and Klein, M. L., "Explicit reversible integrators for extended systems dynamics," *Molecular Physics,* vol. 87, pp. 1117-1157, 1996.

[114] Virtual Nanolab - Atomistix toolkit (QuantumATK version 2016.4), Available: https://www.synopsys.com/silicon/quantumatk.html, (accessed May 25, 2019)

[115] Walther, J. H., Jaffe, R., Halicioglu, T., and Koumoutsakos, P., "Carbon Nanotubes in Water: Structural Characteristics and Energetics," *J. Phys. Chem. B,* vol. 105, pp. 9980-9987, 2001.

[116] Jorgensen, W. L., Chandrasekhar, J., and Madura, J. D., "Comparison of simple potential functions for simulating liquid water," *J. Chem. Phys.,* vol. 79, 926, 1983.

[117] Zou, J., Ji, B., Feng, X.-Q., and Gao, H., "Self-Assembly of Single-Walled Carbon Nanotubes into Multiwalled Carbon Nanotubes in Water: Molecular Dynamics Simulations," *Nano Letters,* vol. 6, pp. 430-434, 2006.

[118] Hao, X., Qiang, H., and Xiaohu, Y., "Buckling of defective single-walled and double-walled carbon nanotubes under axial compression by molecular dynamics simulation," *Composites Science and Technology,* vol. 68, pp. 1809-1814, 2008.

[119] Abadir, G. B., Walus, K., and Pulfrey, D. L., "Bias-dependent amino-acid-induced conductance changes in short semi-metallic carbon nanotubes," *Nanotechnology,* vol. 21, p. 015202, 2010.

[120] Guo, X., Su, J., and Guo, H., "Electric field induced orientation and self-assembly of carbon nanotubes in water," *Soft Matter,* vol. 8, pp. 1010-1016, 2012.

[121] Tu, Q., Yang, Q., Wang, H., and Li, S., "Rotating carbon nanotube membrane filter for water desalination," *Scientific Reports,* vol. 6, 26183, 2016.

[122] Winarto, W., Takaiwa, D., Yamamoto, E., and Yasuoka, K., "Separation of water–ethanol solutions with carbon nanotubes and electric fields," *Physical Chemistry Chemical Physics,* vol. 18, pp. 33310-33319, 2016.

[123] Settanni, G. and Fersht, A. R., "High Temperature Unfolding Simulations of the TRPZ1 Peptide," *Biophysical Journal,* vol. 94, pp. 4444-4453, 2008.

[124] Kelich, P. and Asadinezhad, A., "Molecular Dynamics Insights into Behavior of Poly(ethylene succinate) Single Chain on Carbon Nanotube Surface," *The Journal of Physical Chemistry C,* vol. 119, pp. 26143-26153, 2015.

[125] Mochizuki, K., Pattenaude, S. R., and Ben-Amotz, D., "Influence of Cononsolvency on the Aggregation of Tertiary Butyl Alcohol in Methanol–Water Mixtures," *Journal of the American Chemical Society,* vol. 138, pp. 9045-9048, 2016.

[126] O'Boyle, N. M., Banck, M., James, C. A., Morley, C., Vandermeersch, T., and Hutchison, G. R., "Open Babel: An open chemical toolbox," *Journal of Cheminformatics,* vol. 3, 33, 2011.

[127] The Open Babel Package, version 2.4.1, Available: http://openbabel.org, (accessed May 25, 2019).

[128] Humphrey, W., Dalke, A., and Schulten, K., "VMD: Visual molecular dynamics," *J. Mol. Graphics,* vol. 14, pp. 33-38, 1996.

[129] Fan, D. L., Zhu, F. Q., Cammarata, R. C., and Chien, C. L., "Controllable High-Speed Rotation of Nanowires," *Physical Review Letters,* vol. 94, 247208, 2005.

[130] Supporting movie files showing simulation videos. Available: http://bit.ly/supportingmovies, (accessed May 25, 2019)

[131] Li, X., Wang, X., Zhang, L., Lee, S., and Dai, H., "Chemically Derived, Ultrasmooth Graphene Nanoribbon Semiconductors," *Science,* vol. 319, pp. 1229-1232, 2008.

[132] Sprinkle, M., Ruan, M., Hu, Y., Hankinson, J., Rubio-Roy, M., Zhang, B.*, et al.*, "Scalable templated growth of graphene nanoribbons on SiC," *Nature Nanotechnology,* vol. 5, pp. 727-731, 2010.

[133] Cai, J., Ruffieux, P., Jaafar, R., Bieri, M., Braun, T., Blankenburg, S.*, et al.*, "Atomically precise bottom-up fabrication of graphene nanoribbons," *Nature,* vol. 466, pp. 470-473, 2010.

[134] Chen, Y.-C., de Oteyza, D. G., Pedramrazi, Z., Chen, C., Fischer, F. R., and Crommie, M. F., "Tuning the Band Gap of Graphene Nanoribbons Synthesized from Molecular Precursors," *ACS Nano,* vol. 7, pp. 6123-6128, 2013.

[135] Bennett, P. B., Pedramrazi, Z., Madani, A., Chen, Y.-C., de Oteyza, D. G., Chen, C.*, et al.*, "Bottom-up graphene nanoribbon field-effect transistors," *Applied Physics Letters,* vol. 103, 253114, 2013.

[136] Ci, L., Xu, Z., Wang, L., Gao, W., Ding, F., Kelly, K. F*., et al.*, "Controlled nanocutting of graphene," *Nano Research,* vol. 1, pp. 116-122, 2008.

[137] Campos, L. C., Manfrinato, V. R., Sanchez-Yamagishi, J. D., Kong, J., and Jarillo-Herrero, P., "Anisotropic Etching and Nanoribbon Formation in Single-Layer Graphene," *Nano Letters,* vol. 9, pp. 2600-2604, 2009.

[138] Chen, Y. P., Xie, Y. E., Sun, L. Z., and Zhong, J., "Asymmetric transport in asymmetric T-shaped graphene nanoribbons," *Applied Physics Letters,* vol. 93, 092104, 2008.

[139] OuYang, F., Xiao, J., Guo, R., Zhang, H., and Xu, H., "Transport properties of T-shaped and crossed junctions based on graphene nanoribbons," *Nanotechnology,* vol. 20, 055202, 2009.

[140] Chen, Y. P., Xie, Y. E., and Yan, X. H., "Electron transport of L-shaped graphene nanoribbons," *Journal of Applied Physics,* vol. 103, 063711, 2008.

[141] Papon, R., Sharma, S., Shinde, S. M., Thangaraja, A., Kalita, G., and Tanemura, M., "Formation of graphene nanoribbons and Y-junctions by hydrogen induced anisotropic etching," *RSC Advances,* vol. 5, pp. 35297-35301, 2015.

[142] Wang, Z. F., Shi, Q. W., Li, Q., Wang, X., Hou, J. G., Zheng, H*., et al.*, "Z-shaped graphene nanoribbon quantum dot device," *Applied Physics Letters,* vol. 91, 053109, 2007.

[143] Wang, Z. F., Li, Q., Shi, Q. W., Wang, X., Hou, J. G., Zheng, H*., et al.*, "Ballistic rectification in a Z-shaped graphene nanoribbon junction," *Applied Physics Letters,* vol. 92, 133119, 2008.

[144] Chen, Y.-C., Cao, T., Chen, C., Pedramrazi, Z., Haberer, D., de Oteyza, D. G*., et al.*, "Molecular bandgap engineering of bottom-up synthesized graphene nanoribbon heterojunctions," *Nature Nanotechnology,* vol. 10, pp. 156-160, 2015.

[145] Newaz, A. K. M., Puzyrev, Y. S., Wang, B., Pantelides, S. T., and Bolotin, K. I., "Probing charge scattering mechanisms in suspended graphene by varying its dielectric environment," *Nature Communications,* vol. 3, 734, 2012.

[146] Verhoeven, J. and Dymanus, A., "Magnetic Properties and Molecular Quadrupole Tensor of the Water Molecule by Beam-Maser Zeeman Spectroscopy," *The Journal of Chemical Physics,* vol. 52, pp. 3222-3233, 1970.

[147] Clough, S. A., Beers, Y., Klein, G. P., and Rothman, L. S., "Dipole moment of water from Stark measurements of H_2O, HDO, and D_2O," *The Journal of Chemical Physics,* vol. 59, pp. 2254-2259, 1973.

[148] Jorgensen, W. L. and Jenson, C., "Temperature dependence of TIP3P, SPC, and TIP4P water from NPT Monte Carlo simulations: Seeking temperatures of maximum density," *Journal of Computational Chemistry,* vol. 19, pp. 1179-1186, 1998.

[149] Mahoney, M. W. and Jorgensen, W. L., "A five-site model for liquid water and the reproduction of the density anomaly by rigid, nonpolarizable potential functions," *The Journal of Chemical Physics,* vol. 112, pp. 8910-8922, 2000.